

## THE LARGE AREA TELESCOPE ON THE *FERMI* GAMMA-RAY SPACE TELESCOPE MISSION

W. B. ATWOOD<sup>1</sup>, A. A. ABDO<sup>2,3</sup>, M. ACKERMANN<sup>4</sup>, B. ANDERSON<sup>1</sup>, M. AXELSSON<sup>5</sup>, L. BALDINI<sup>6</sup>, J. BALLE<sup>7</sup>, D. L. BAND<sup>8,9</sup>, G. BARBIELLINI<sup>10,11</sup>, J. BARTELT<sup>4</sup>, D. BASTIERI<sup>12,13</sup>, B. M. BAUGHMAN<sup>14</sup>, K. BECHTOL<sup>4</sup>, D. BÉDÉREDE<sup>15</sup>, F. BELLARDI<sup>6</sup>, R. BELLAZZINI<sup>6</sup>, B. BERENJI<sup>4</sup>, G. F. BIGNAMI<sup>16</sup>, D. BISELLO<sup>12,13</sup>, E. BISSALDI<sup>17</sup>, R. D. BLANDFORD<sup>4</sup>, E. D. BLOOM<sup>4</sup>, J. R. BOGART<sup>4</sup>, E. BONAMENTE<sup>18,19</sup>, J. BONNELL<sup>9</sup>, A. W. BORGLAND<sup>4</sup>, A. BOUVIER<sup>4</sup>, J. BREGEON<sup>6</sup>, A. BREZ<sup>6</sup>, M. BRIGIDA<sup>20,21</sup>, P. BRUEL<sup>22</sup>, T. H. BURNETT<sup>23</sup>, G. BUSETTO<sup>12,13</sup>, G. A. CALIANDRO<sup>20,21</sup>, R. A. CAMERON<sup>4</sup>, P. A. CARAVEO<sup>24</sup>, S. CARIUS<sup>25</sup>, P. CARLSON<sup>26</sup>, J. M. CASANDJIAN<sup>7</sup>, E. CAVAZZUTI<sup>27</sup>, M. CECCANTI<sup>6</sup>, C. CECCHI<sup>18,19</sup>, E. CHARLES<sup>4</sup>, A. CHEKHTMAN<sup>28,3</sup>, C. C. CHEUNG<sup>9</sup>, J. CHIANG<sup>4</sup>, R. CHIPAUX<sup>29</sup>, A. N. CILLIS<sup>9</sup>, S. CIPRINI<sup>18,19</sup>, R. CLAU<sup>4</sup>, J. COHEN-TANUGI<sup>30</sup>, S. CONDAMOR<sup>4</sup>, J. CONRAD<sup>26,31</sup>, R. CORBET<sup>9</sup>, L. CORUCCI<sup>6</sup>, L. COSTAMANTE<sup>4</sup>, S. CUTINI<sup>27</sup>, D. S. DAVIS<sup>9,32</sup>, D. DECOTIGNY<sup>22</sup>, M. DEKLOTZ<sup>33</sup>, C. D. DERMER<sup>3</sup>, A. DE ANGELIS<sup>34</sup>, S. W. DIGEL<sup>4</sup>, E. DO COUTO E SILVA<sup>4</sup>, P. S. DRELL<sup>4</sup>, R. DUBOIS<sup>4</sup>, D. DUMORA<sup>35,36</sup>, Y. EDMONDS<sup>4</sup>, D. FABIANI<sup>6</sup>, C. FARNIER<sup>30</sup>, C. FAVUZZI<sup>20,21</sup>, D. L. FLATH<sup>4</sup>, P. FLEURY<sup>22</sup>, W. B. FOCKE<sup>4</sup>, S. FUNK<sup>4</sup>, P. FUSCO<sup>20,21</sup>, F. GARGANO<sup>21</sup>, D. GASPARRINI<sup>27</sup>, N. GEHRELS<sup>9,37</sup>, F.-X. GENTIL<sup>38</sup>, S. GERMANI<sup>18,19</sup>, B. GIEBELS<sup>22</sup>, N. GIGLIETTO<sup>20,21</sup>, P. GIOMMI<sup>27</sup>, F. GIORDANO<sup>20,21</sup>, T. GLANZMAN<sup>4</sup>, G. GODFREY<sup>4</sup>, I. A. GRENIER<sup>7</sup>, M.-H. GRONDIN<sup>35,36</sup>, J. E. GROVE<sup>3</sup>, L. GUILLEMOT<sup>35,36</sup>, S. GUIRIEC<sup>30</sup>, G. HALLER<sup>4</sup>, A. K. HARDING<sup>9</sup>, P. A. HART<sup>4</sup>, E. HAYS<sup>9</sup>, S. E. HEALEY<sup>4</sup>, M. HIRAYAMA<sup>9,32</sup>, L. HJALMARSDOTTER<sup>3</sup>, R. HORN<sup>33</sup>, G. JÓHANNESSON<sup>4</sup>, G. JOHANSSON<sup>25</sup>, A. S. JOHNSON<sup>4</sup>, R. P. JOHNSON<sup>1</sup>, T. J. JOHNSON<sup>9,37</sup>, W. N. JOHNSON<sup>3</sup>, T. KAMAE<sup>4</sup>, H. KATAGIRI<sup>39</sup>, J. KATAOKA<sup>40</sup>, A. KAVELAARS<sup>4</sup>, N. KAWAI<sup>41,40</sup>, H. KELLY<sup>4</sup>, M. KERR<sup>23</sup>, W. KLAMRA<sup>26</sup>, J. KNÖDLSER<sup>42</sup>, M. L. KOCIAN<sup>4</sup>, N. KOMIN<sup>7,30</sup>, F. KUEHN<sup>14</sup>, M. KUSS<sup>6</sup>, D. LANDRIU<sup>7</sup>, L. LATRONICO<sup>6</sup>, B. LEE<sup>43</sup>, S.-H. LEE<sup>4</sup>, M. LEMOINE-GOUMARD<sup>35,36</sup>, A. M. LIONETTO<sup>44,45</sup>, F. LONGO<sup>10,11</sup>, F. LOPARCO<sup>20,21</sup>, B. LOTT<sup>35,36</sup>, M. N. LOVELLETTE<sup>3</sup>, P. LUBRANO<sup>18,19</sup>, G. M. MADEJSKI<sup>4</sup>, A. MAKEEV<sup>28,3</sup>, B. MARANGELLI<sup>20,21</sup>, M. M. MASSAI<sup>6</sup>, M. N. MAZZIOTTA<sup>21</sup>, J. E. MCENERY<sup>9</sup>, N. MENON<sup>6,33</sup>, C. MEURER<sup>31</sup>, P. F. MICHELSON<sup>4,46</sup>, M. MINUTI<sup>6</sup>, N. MIRIZZI<sup>20,21</sup>, W. MITTHUMSIRI<sup>4</sup>, T. MIZUNO<sup>39</sup>, A. A. MOISEEV<sup>8</sup>, C. MONTE<sup>20,21</sup>, M. E. MONZANI<sup>4</sup>, E. MORETTI<sup>10,11</sup>, A. MORSELLI<sup>44,45</sup>, I. V. MOSKALENKO<sup>4</sup>, S. MURCIA<sup>4</sup>, T. NAKAMORI<sup>40</sup>, S. NISHINO<sup>39</sup>, P. L. NOLAN<sup>4</sup>, J. P. NORRIS<sup>47</sup>, E. NUSS<sup>30</sup>, M. OHNO<sup>48</sup>, T. OHSUGI<sup>39</sup>, N. OMODEI<sup>6</sup>, E. ORLANDO<sup>17</sup>, J. F. ORMES<sup>47</sup>, A. PACCAGNELLA<sup>12,49</sup>, D. PANEQUE<sup>4</sup>, J. H. PANETTA<sup>4</sup>, D. PARENT<sup>35,36</sup>, M. PEARCE<sup>26</sup>, M. PEPE<sup>18,19</sup>, A. PERAZZO<sup>4</sup>, M. PESCE-ROLLINS<sup>6</sup>, P. PICOZZA<sup>44,45</sup>, L. PIERI<sup>12</sup>, M. PINCHERA<sup>6</sup>, F. PIRON<sup>30</sup>, T. A. PORTER<sup>1</sup>, L. POUPARD<sup>7</sup>, S. RAINO<sup>20,21</sup>, R. RANDO<sup>12,13</sup>, E. RAPPOSELLI<sup>6</sup>, M. RAZZANO<sup>6</sup>, A. REIMER<sup>4</sup>, O. REIMER<sup>4</sup>, T. REPOSEUR<sup>35,36</sup>, L. C. REYES<sup>50</sup>, S. RITZ<sup>9,37</sup>, L. S. ROCHESTER<sup>4</sup>, A. Y. RODRIGUEZ<sup>21</sup>, R. W. ROMANI<sup>4</sup>, M. ROTH<sup>23</sup>, J. J. RUSSELL<sup>4</sup>, F. RYDE<sup>26</sup>, S. SABATINI<sup>44,45</sup>, H. F.-W. SADROZINSKI<sup>1</sup>, D. SANCHEZ<sup>22</sup>, A. SANDER<sup>14</sup>, L. SAPOZHNIKOV<sup>4</sup>, P. M. SAZ PARKINSON<sup>1</sup>, J. D. SCARGLE<sup>52</sup>, T. L. SCHALK<sup>1</sup>, G. SCOLIERI<sup>53</sup>, C. SGRO<sup>6</sup>, G. H. SHARE<sup>3,54</sup>, M. SHAW<sup>4</sup>, T. SHIMOKAWABE<sup>40</sup>, C. SHRADER<sup>8</sup>, A. SIERPOWSKA-BARTOSIK<sup>51</sup>, E. J. SISKIND<sup>55</sup>, D. A. SMITH<sup>35,36</sup>, P. D. SMITH<sup>14</sup>, G. SPANDRE<sup>6</sup>, P. SPINELLI<sup>20,21</sup>, J.-L. STARCK<sup>7</sup>, T. E. STEPHENS<sup>9</sup>, M. S. STRICKMAN<sup>3</sup>, A. W. STRONG<sup>17</sup>, D. J. SUSON<sup>56</sup>, H. TAJIMA<sup>4</sup>, H. TAKAHASHI<sup>39</sup>, T. TAKAHASHI<sup>48</sup>, T. TANAKA<sup>4</sup>, A. TENZE<sup>6</sup>, S. TETHER<sup>4</sup>, J. B. THAYER<sup>4</sup>, J. G. THAYER<sup>4</sup>, D. J. THOMPSON<sup>9</sup>, L. TIBALDO<sup>12,13</sup>, O. TIBOLLA<sup>57</sup>, D. F. TORRES<sup>58,51</sup>, G. TOSTI<sup>18,19</sup>, A. TRAMACERE<sup>59,4</sup>, M. TURRI<sup>4</sup>, T. L. USHER<sup>4</sup>, N. VILCHEZ<sup>42</sup>, V. VITALE<sup>44,45</sup>, P. WANG<sup>4</sup>, K. WATTERS<sup>4</sup>, B. L. WINER<sup>14</sup>, K. S. WOOD<sup>3</sup>, T. YLINEN<sup>25,26</sup>, M. ZIEGLER<sup>1</sup>

1. Santa Cruz Institute for Particle Physics, Department of Physics and Department of Astronomy and Astrophysics, University of California at Santa Cruz, Santa Cruz, CA 95064
2. National Research Council Research Associate
3. Space Science Division, Naval Research Laboratory, Washington, DC 20375
4. W. W. Hansen Experimental Physics Laboratory, Kavli Institute for Particle Astrophysics and Cosmology, Department of Physics and Stanford Linear Accelerator Center, Stanford University, Stanford, CA 94305
5. Stockholm Observatory, Albanova, SE-106 91 Stockholm, Sweden
6. Istituto Nazionale di Fisica Nucleare, Sezione di Pisa, I-56127 Pisa, Italy
7. Laboratoire AIM, CEA-IRFU/CNRS/Université Paris Diderot, Service d'Astrophysique, CEA Saclay, 91191 Gif sur Yvette, France
8. Center for Research and Exploration in Space Science and Technology (CRESTT), NASA Goddard Space Flight Center, Greenbelt, MD 20771
9. NASA Goddard Space Flight Center, Greenbelt, MD 20771
10. Istituto Nazionale di Fisica Nucleare, Sezione di Trieste, I-34127 Trieste, Italy
11. Dipartimento di Fisica, Università di Trieste, I-34127 Trieste, Italy
12. Istituto Nazionale di Fisica Nucleare, Sezione di Padova, I-35131 Padova, Italy
13. Dipartimento di Fisica "G. Galilei", Università di Padova, I-35131 Padova, Italy
14. Department of Physics, Center for Cosmology and Astro-Particle Physics, The Ohio State University, Columbus, OH 43210
15. IRFU/Dir, CEA Saclay, 91191 Gif sur Yvette, France
16. Istituto Universitario di Studi Superiori (IUSS), I-27100 Pavia, Italy
17. Max-Planck-Institut für Extraterrestrische Physik, Giessenbachstraße, 85748 Garching, Germany
18. Istituto Nazionale di Fisica Nucleare, Sezione di Perugia, I-06123 Perugia, Italy
19. Dipartimento di Fisica, Università degli Studi di Perugia, I-06123 Perugia, Italy
20. Dipartimento di Fisica "M. Merlin" dell'Università e del Politecnico di Bari, I-70126 Bari, Italy
21. Istituto Nazionale di Fisica Nucleare, Sezione di Bari, 70126 Bari, Italy
22. Laboratoire Leprince-Ringuet, École polytechnique, CNRS/IN2P3, Palaiseau, France
23. Department of Physics, University of Washington, Seattle, WA 98195-1560
24. INFN-Istituto di Astrofisica Spaziale e Fisica Cosmica, I-20133 Milano, Italy
25. School of Pure and Applied Natural Sciences, University of Kalmar, SE-391 82 Kalmar, Sweden
26. Department of Physics, Royal Institute of Technology (KTH), AlbaNova, SE-106 91 Stockholm, Sweden
27. Agenzia Spaziale Italiana (ASI) Science Data Center, I-00044 Frascati (Roma), Italy
28. George Mason University, Fairfax, VA 22030
29. IRFU/SEDI, CEA Saclay, 91191 Gif sur Yvette, France
30. Laboratoire de Physique Théorique et Astroparticules, Université Montpellier 2, CNRS/IN2P3, Montpellier, France
31. Department of Physics, Stockholm University, AlbaNova, SE-106 91 Stockholm, Sweden
32. Center for Space Sciences and Technology, University of Maryland, Baltimore County, Baltimore, MD 21250, USA
33. Stellar Solutions Inc., 250 Cambridge Avenue, Suite 204, Palo Alto, CA 94306
34. Dipartimento di Fisica, Università di Udine and Istituto Nazionale di Fisica Nucleare, Sezione di Trieste, Gruppo Collegato di Udine, I-33100 Udine, Italy
35. CNRS/IN2P3, Centre d'Études Nucléaires Bordeaux Gradignan, UMR 5797, Gradignan, 33175, France

36. Université de Bordeaux, Centre d'Études Nucléaires Bordeaux Gradignan, UMR 5797, Gradignan, 33175, France  
 37. University of Maryland, College Park, MD 20742  
 38. IRFU/Service de Physique des Particules, CEA Saclay, 91191 Gif sur Yvette, France  
 39. Department of Physical Science and Hiroshima Astrophysical Science Center, Hiroshima University, Higashi-Hiroshima 739-8526, Japan  
 40. Department of Physics, Tokyo Institute of Technology, Meguro City, Tokyo 152-8551, Japan  
 41. Cosmic Radiation Laboratory, Institute of Physical and Chemical Research (RIKEN), Wako, Saitama 351-0198, Japan  
 42. Centre d'Étude Spatiale des Rayonnements, CNRS/UPS, BP 44346, F-30128 Toulouse Cedex 4, France  
 43. Orbital Network Engineering, 10670 North Tantau Avenue, Cupertino, CA 95014  
 44. Istituto Nazionale di Fisica Nucleare, Sezione di Roma "Tor Vergata", I-00133 Roma, Italy  
 45. Dipartimento di Fisica, Università di Roma "Tor Vergata", I-00133 Roma, Italy  
 46. Corresponding author: P. F. Michelson, peterm@stanford.edu.  
 47. Department of Physics and Astronomy, University of Denver, Denver, CO 80208  
 48. Institute of Space and Astronautical Science, JAXA, 3-1-1 Yoshinodai, Sagami-hara, Kanagawa 229-8510, Japan  
 49. Dipartimento di Ingegneria dell'Informazione, Università di Padova, I-35131 Padova, Italy  
 50. Kavli Institute for Cosmological Physics, University of Chicago, Chicago, IL 60637  
 51. Institut de Ciències de l'Espai (IEEC-CSIC), Campus UAB, 08193 Barcelona, Spain  
 52. Space Sciences Division, NASA Ames Research Center, Moffett Field, CA 94035-1000  
 53. Istituto Nazionale di Fisica Nucleare, Sezione di Perugia and Università di Perugia, I-06123 Perugia, Italy  
 54. Praxis Inc., Alexandria, VA 22303  
 55. NYCB Real-Time Computing Inc., 18 Meudon Drive, Lattingtown, NY 11560-1025  
 56. Department of Chemistry and Physics, Purdue University Calumet, Hammond, IN 46323-2094  
 57. Landessternwarte, Universität Heidelberg, Königstuhl, D 69117 Heidelberg, Germany  
 58. Institució Catalana de Recerca i Estudis Avançats (ICREA), Barcelona, Spain and  
 59. Consorzio Interuniversitario per la Fisica Spaziale (CIFS), I-10133 Torino, Italy

Draft version February 6, 2009

## ABSTRACT

The Large Area Telescope (*Fermi*/LAT, hereafter LAT), the primary instrument on the *Fermi Gamma-ray Space Telescope* (*Fermi*) mission, is an imaging, wide field-of-view, high-energy  $\gamma$ -ray telescope, covering the energy range from below 20 MeV to more than 300 GeV. The LAT was built by an international collaboration with contributions from space agencies, high-energy particle physics institutes, and universities in France, Italy, Japan, Sweden, and the United States. This paper describes the LAT, its pre-flight expected performance, and summarizes the key science objectives that will be addressed. On-orbit performance will be presented in detail in a subsequent paper. The LAT is a pair-conversion telescope with a precision tracker and calorimeter, each consisting of a  $4 \times 4$  array of 16 modules, a segmented anticoincidence detector that covers the tracker array, and a programmable trigger and data acquisition system. Each tracker module has a vertical stack of 18  $x, y$  tracking planes, including two layers ( $x$  and  $y$ ) of single-sided silicon strip detectors and high- $Z$  converter material (tungsten) per tray. Every calorimeter module has 96 CsI(Tl) crystals, arranged in an 8 layer hodoscopic configuration with a total depth of 8.6 radiation lengths, giving both longitudinal and transverse information about the energy deposition pattern. The calorimeter's depth and segmentation enable the high-energy reach of the LAT and contribute significantly to background rejection. The aspect ratio of the tracker (height/width) is 0.4, allowing a large field-of-view (2.4 sr) and ensuring that most pair-conversion showers initiated in the tracker will pass into the calorimeter for energy measurement. Data obtained with the LAT are intended to (i) permit rapid notification of high-energy  $\gamma$ -ray bursts (GRBs) and transients and facilitate monitoring of variable sources, (ii) yield an extensive catalog of several thousand high-energy sources obtained from an all-sky survey, (iii) measure spectra from 20 MeV to more than 50 GeV for several hundred sources, (iv) localize point sources to 0.3 – 2 arc minutes, (v) map and obtain spectra of extended sources such as SNRs, molecular clouds, and nearby galaxies, (vi) measure the diffuse isotropic  $\gamma$ -ray background up to TeV energies, and (vii) explore the discovery space for dark matter.

*Subject headings:* gamma rays: pulsars — gamma rays: AGNs — gamma rays: blazars — gamma rays: SNRs — gamma rays: diffuse — gamma rays: dark matter — instruments: telescopes

## 1. INTRODUCTION

A revolution is underway in our understanding of the high-energy sky. The early SAS-2 (Fichtel et al. 1975) and COS-B (Bignami et al. 1975) missions led to the EGRET instrument (Thompson et al. 1993) on the *Compton Gamma-Ray Observatory* (*CGRO*). EGRET performed the first all-sky survey above 50 MeV and made breakthrough observations of high-energy  $\gamma$ -ray blazars, pulsars, delayed emission from  $\gamma$ -ray bursts (GRBs), high-energy solar flares, and diffuse radiation from our Galaxy and beyond that have all changed our view of the high-energy Universe.

Many high-energy sources revealed by EGRET have not yet been identified. The Large Area Telescope (LAT) on the *Fermi Gamma-ray Space Telescope* (*Fermi*), formerly the *Gamma-ray Large Area Space Telescope* (*GLAST*), launched

by NASA on 2008, June 11 on a Delta II Heavy launch vehicle, offers enormous opportunities for determining the nature of these sources and advancing knowledge in astronomy, astrophysics, and particle physics. In this paper a comprehensive overview of the LAT instrument design is provided, the pre-flight expected performance based on detailed simulations and ground calibration measurements is given, and the science goals and expectations are summarized. The *Fermi* observatory had been launched shortly before the submission of this paper so no details of in-flight performance are provided at this time, although the performance to date does not deviate significantly from that estimated before launch. The in-flight calibration of the LAT is being refined during the first year of observations and therefore details of in-flight performance will be the subject of a future paper.

*Fermi* follows the successful launch of *Agile* by the Italian Space Agency in April 2007 (Tavani et al. 2008). The scientific objectives addressed by the LAT include (i) determining the nature of the unidentified sources and the origins of the diffuse emission revealed by EGRET, (ii) understanding the mechanisms of particle acceleration operating in celestial sources, particularly in active galactic nuclei, pulsars, supernovae remnants, and the Sun, (iii) understanding the high-energy behavior of GRBs and transients, (iv) using  $\gamma$ -ray observations as a probe of dark matter, and (v) using high-energy  $\gamma$ -rays to probe the early universe and the cosmic evolution of high-energy sources to  $z \geq 6$ . These objectives are discussed in the context of the LAT's measurement capabilities in §3.

To make significant progress in understanding the high-energy sky, the LAT, shown in Figure 1, has good angular resolution for source localization and multi-wavelength studies, high sensitivity over a broad field-of-view to monitor variability and detect transients, good calorimetry over an extended energy band to study spectral breaks and cut-offs, and good calibration and stability for absolute, long term flux measurement. The LAT measures the tracks of the electron ( $e^-$ ) and positron ( $e^+$ ) that result when an incident  $\gamma$ -ray undergoes pair-conversion, preferentially in a thin, high- $Z$  foil, and measures the energy of the subsequent electromagnetic shower that develops in the telescope's calorimeter. Table 1 summarizes the scientific performance capabilities of the LAT. Figure 2 illustrates the sensitivity and field-of-view (FoV) achieved with the LAT for exposures on various timescales. To take full advantage of the LAT's large FoV, the primary observing mode of *Fermi* is the so-called "scanning" mode in which the normal to the front of the instrument ( $z$  axis) on alternate orbits is pointed to  $+35^\circ$  from the zenith direction and towards the pole of the orbit and to  $-35^\circ$  from the zenith on the subsequent orbit. In this way, after 2 orbits, about 3 hours for *Fermi*'s orbit at  $\sim 565$  km and  $25.5^\circ$  inclination, the sky exposure is almost uniform. For particularly interesting targets of opportunity, the observatory can be inertially pointed. Details of the LAT design and performance are presented in §2.

The LAT was developed by an international collaboration with primary hardware and software responsibilities at Stanford University, Stanford Linear Accelerator Center, Agenzia Spaziale Italiana, Commissariat à l'Energie Atomique, Goddard Space Flight Center, Istituto Nazionale di Fisica Nucleare, Centre National de la Recherche Scientifique / Institut National de Physique Nucléaire et de Physique des Particules, Hiroshima University, Naval Research Laboratory, Ohio State University, Royal Institute of Technology – Stockholm, University of California at Santa Cruz, and University of Washington. Other institutions that have made significant contributions to the instrument development include Institute of Space and Astronautical Science, Stockholm University, University of Tokyo, and Tokyo Institute of Science and Technology. All of these institutions as well as the Istituto Nazionale di Astrofisica in Italy are making significant contributions to LAT data analysis during the science operations phase of the *Fermi* mission.

## 2. LARGE AREA TELESCOPE

### 2.1. Technical development path

The LAT is designed to measure the directions, energies, and arrival times of  $\gamma$ -rays incident over a wide FoV, while rejecting background from cosmic rays. First, the design approach (Atwood et al. 1994) that resulted in the instrument

described in detail in §2.2 made extensive use of detailed simulations of the detector response to signal (celestial  $\gamma$ -rays) and backgrounds (cosmic rays, albedo  $\gamma$ -rays, etc.). Second, detector technologies were chosen that have an extensive history of application in space science and high-energy physics with demonstrated high reliability. Third, relevant test models were built to demonstrate that critical requirements, such as power, efficiency, and detector noise occupancy, could be readily met. Fourth, these detector-system models, including all subsystems, were studied in accelerator test beams to validate both the design and the Monte Carlo programs used in the simulations (Atwood et al. 2000).

The modular design of the LAT allowed the construction, at reasonable incremental cost, of a full-scale, fully functional engineering demonstration telescope module for validation of the design concept. This test engineering model was flown on a high-altitude balloon to demonstrate system level performance in a realistic, harsh background environment (Thompson et al. 2002; Mizuno et al. 2004) and was subjected to an accelerator beam test program (Couto é Silva et al. 2001). Particle beam tests were also done on spare flight tracker and calorimeter modules (see (§2.5.1).

### 2.2. Technical description

High-energy  $\gamma$ -rays cannot be reflected or refracted; they interact by the conversion of the  $\gamma$ -ray into an  $e^+e^-$  pair. The LAT is therefore a pair-conversion telescope with a precision converter-tracker (§2.2.1) and calorimeter (§2.2.2), each consisting of a  $4 \times 4$  array of 16 modules supported by a low-mass aluminum grid structure. A segmented anticoincidence detector (ACD, §2.2.3) covers the tracker array, and a programmable trigger and data acquisition system (DAQ, §2.2.4) utilizes prompt signals available from the tracker, calorimeter, and anticoincidence detector subsystems to form a trigger. The self-triggering capability of the LAT tracker in particular is an important new feature of the LAT design that is possible because of the choice of silicon-strip detectors, which do not require an external trigger, for the active elements. In addition, all of the LAT instrument subsystems utilize technologies that do not use consumables such as gas. Upon triggering, the DAQ initiates the read out of these 3 subsystems and utilizes on-board event processing to reduce the rate of events transmitted to the ground to a rate compatible with the 1 Mbps average downlink available to the LAT. The on-board processing is optimized for rejecting events triggered by cosmic-ray background particles while maximizing the number of events triggered by  $\gamma$ -rays, which are transmitted to the ground. Heat produced by the tracker, calorimeter, and DAQ electronics is transferred to radiators through heat pipes in the grid.

The overall aspect ratio of the LAT tracker (height/width) is 0.4, allowing a large FoV<sup>1</sup> and ensuring that nearly all pair-conversion events initiated in the tracker will pass into the calorimeter for energy measurement.

#### 2.2.1. Precision converter-tracker

The converter-tracker has 16 planes of high- $Z$  material in which  $\gamma$ -rays incident on the LAT can convert to an  $e^+e^-$  pair. The converter planes are interleaved with position-sensitive detectors that record the passage of charged particles, thus

<sup>1</sup> FoV =  $\int A_{\text{eff}}(\theta, \phi) d\Omega / A_{\text{eff}}(0, 0) = 2.4$  sr at 1 GeV, where  $A_{\text{eff}}$  is the effective area of the LAT after all analysis cuts for background rejections have been made.

measuring the tracks of the particles resulting from pair conversion. This information is used to reconstruct the directions of the incident  $\gamma$ -rays. Each tracker module has 18  $x, y$  tracking planes, consisting of 2 layers ( $x$  and  $y$ ) of single-sided silicon strip detectors. The 16 planes at the top of the tracker are interleaved with high- $Z$  converter material (tungsten). Figure 3 shows the completed 16 module tracker array before integration with the ACD. Table 2 is a summary of key parameters of the LAT tracker. See Atwood et al. (2007) for a more complete discussion of the tracker design and performance. We summarize here the features most relevant to the instrument science performance.

The single-sided SSDs are AC-coupled, with 384 56- $\mu\text{m}$  wide aluminum readout strips spaced at 228  $\mu\text{m}$  pitch<sup>2</sup>. They were produced on  $n$ -intrinsic 15-cm wafers by Hamamatsu Photonics, and each has an area of  $8.95 \times 8.95 \text{ cm}^2$ , with an inactive area 1 mm wide around the edges, and a thickness of 400  $\mu\text{m}$ . Sets of 4 SSDs were bonded edge to edge with epoxy and then wire bonded strip to strip to form “ladders,” such that each amplifier channel sees signals from a 35 cm long strip. Each detector layer in a tracker module consists of 4 such ladders spaced apart by 0.2 mm gaps. The delivered SSD quality was very high, with a bad channel rate less than 0.01% and an average total leakage current of 110 nA. The wafer dicing was accurate to better than 20  $\mu\text{m}$ , to allow all of the assembly to be done rapidly with mechanical jigs rather than with optical references.

The support structure for the detectors and converter foil planes is a stack of 19 composite panels, or “trays,” supported by carbon-composite sidewalls that also serve to conduct heat to the base of the tracker array. The tray structure is a low-mass, carbon-composite assembly made of a carbon-carbon closeout, carbon-composite face sheets, and a vented aluminum honeycomb core. Carbon was chosen for its long radiation length, high modulus (stiffness) to density ratio, good thermal conductivity, and thermal stability.

The tray-panel structure is about 3 cm thick and is instrumented with converter foils, detectors, and front-end electronics. All trays are of similar construction, but the top and bottom trays have detectors on only a single face. The bottom trays include the mechanical and thermal interfaces to the grid, while the top trays support the readout-cable terminations, mechanical lifting attachments, and optical survey retro-reflectors. Trays supporting thick converter foils have stronger face sheets and heavier core material than those supporting thin foils or no foils. Figure 4a shows a flight tracker tray and Figure 4b shows a completed tracker module with one sidewall removed.

The strips on the top and bottom of a given tray are parallel, while alternate trays are rotated  $90^\circ$  with respect to each other. An  $x, y$  measurement plane consists of a layer of detectors on the bottom of one tray together with an orthogonal detector layer on the top of the tray just below, with only a 2 mm separation. The tungsten converter foils in the first 16 planes lie immediately above the upper detector layer in each plane. The lowest two  $x, y$  planes have no tungsten converter material. The tracker mechanical design emphasizes minimization of dead area within its aperture. To that end, the readout electronics are mounted on the sides of the trays and interfaced to the detectors around the  $90^\circ$  corner. One fourth of the readout electronics boards in a single tracker module can be seen in Figure 4b. The interface to the data acquisi-

tion and power supplies is made entirely through flat cables constructed as long 4-layer flexible circuits, two of which are visible in Figure 4b. As a result, the dead space between the active area of one tracker module and that of its neighbor is only 18 mm.

Incident photons preferentially convert in one of the tungsten foils, and the resulting  $e^-$  and  $e^+$  particles are tracked by the SSDs through successive planes. The pair conversion signature is also used to help reject the much larger background of charged cosmic rays. The high intrinsic efficiency and reliability of this technology enables straightforward event reconstruction and determination of the direction of the incident photon.

The probability distribution for the reconstructed direction of incident  $\gamma$ -rays from a point source is referred to as the Point Spread Function (PSF). Multiple scattering of the  $e^+$  and  $e^-$  and bremsstrahlung production limit the obtainable resolution. To get optimal results requires that the  $e^-$  and  $e^+$  directions be measured immediately following the conversion. At 100 MeV the penalty for missing one of the first hits<sup>3</sup> is about a factor of two in resolution, resulting in large tails in the PSF. Figure 5 summarizes these and other considerations in the tracker design that impact the PSF. In particular, it is important that the silicon-strip detector layers have high efficiency and are held close to the converter foils, that the inactive regions are localized and minimized, and that the passive material is minimized. To minimize missing hits in the first layer following a conversion, the tungsten foils in each plane cover only the active areas of the silicon-strip detectors.

One of the most complex LAT design trades was the balance between the need for thin converters, to achieve a good PSF at low energy, where the PSF is determined primarily by the  $\sim 1/E$  dependence of multiple scattering, versus the need for converter material to maximize the effective area, important at high energy. The resolution was to divide the tracker into 2 regions, “front” and “back.” The front region (first 12  $x, y$  tracking planes) has thin converters, each 0.03 radiation lengths thick, to optimize the PSF at low energy, while the converters in the back (4  $x, y$  planes after the front tracker section) are  $\sim 6$  times thicker, to maximize the effective area at the expense of less than a factor of two in angular resolution (at 1 GeV) for photons converting in that region. Instrument simulations show that the sensitivity of the LAT to point-sources is approximately balanced between the front and back tracker sections, although this depends on the source spectral characteristics.

The tracker detector performance was achieved with readout electronics designed specifically to meet the LAT requirements and implemented with standard commercial technology (Baldini et al. 2006). The system is based on two Application Specific Integrated Circuits (ASICs). The first ASIC is a 64-channel mixed-mode amplifier-discriminator chip and the second ASIC is a digital readout controller. Each amplifier-discriminator chip is programmed with a single threshold level, and only a 0 or 1 (i.e., a “hit”) is stored for each channel when a trigger is generated. Each channel can buffer up to 4 events, and the system is able to trigger even during readout of the digital data from previous events. Thus the system achieves high throughput and very low deadtime, and the output data stream is compact and contains just the information needed for effective tracking, with  $< 10^{-6}$  noise

<sup>2</sup> pitch = distance between centers of adjacent strips.

<sup>3</sup> The term “hit” refers to the detection of the passage of a charged particle through a silicon strip and the recording of the strip address.

occupancy, and with very little calibration required. The system also measures and records the time-over-threshold (TOT) of each layer's trigger output signal, which provides charge-deposition information that is useful for background rejection. In particular, isolated tracks that start from showers in the calorimeter sometimes range out in the tracker, mimicking a  $\gamma$ -ray conversion. The TOT information is effective for detecting and rejecting such background events because at the termination of such tracks the charge deposition is very large, often resulting in a large TOT in the last SSD traversed.

The tracker provides the principal trigger for the LAT. Each detector layer in each module outputs a logical OR of all of its 1536 channels, and a first-level trigger is derived from coincidence of successive layers (typically 3  $x, y$  planes). There is no detectable coherent noise in the system, such that the coincidence rate from electronics noise is immeasurably small, while the trigger efficiency for charged particles approaches 100% when all layers are considered.

High reliability was a core requirement in the tracker design. The 16 modules operate independently, providing much redundancy. Similarly, the multi-layer design of each module provides redundancy. The readout system is also designed to minimize or eliminate the impact of single-point failures. Each tracker layer has two separate readout and control paths, and the 24 amplifier-discriminator chips in each layer can be partitioned between the two paths by remote command. Therefore, failure of a single chip or readout cable would result in the loss of at most only 64 channels.

### 2.2.2. Calorimeter

The primary purposes of the calorimeter are twofold: (i) to measure the energy deposition due to the electromagnetic particle shower that results from the  $e^+e^-$  pair produced by the incident photon; and (ii) image the shower development profile, thereby providing an important background discriminator and an estimator of the shower energy leakage fluctuations. Each calorimeter module has 96 CsI(Tl) crystals, with each crystal of size 2.7 cm  $\times$  2.0 cm  $\times$  32.6 cm. The crystals are optically isolated from each other and are arranged horizontally in 8 layers of 12 crystals each. The total vertical depth of the calorimeter is 8.6 radiation lengths (for a total instrument depth of 10.1 radiation lengths). Each calorimeter module layer is aligned 90° with respect to its neighbors, forming an  $x, y$  (hodoscopic) array (Carson et al. 1996). Figure 6 shows schematically the configuration of a calorimeter module and Table 3 is a summary of key parameters of the calorimeter.

The size of the CsI crystals is a compromise between electronic channel count and desired segmentation within the calorimeter. The lateral dimensions of the crystals are comparable to the CsI radiation length (1.86 cm) and Molière radius (3.8 cm) for electromagnetic showers. Each CsI crystal provides 3 spatial coordinates for the energy deposited within: two discrete coordinates from the physical location of the crystal in the array and the third, more precise, coordinate determined by measuring the light yield asymmetry at the ends of the crystal along its long dimension. This level of segmentation is sufficient to allow spatial imaging of the shower and accurate reconstruction of its direction. The calorimeter's shower imaging capability and depth enable the high-energy reach of the LAT and contribute significantly to background rejection. In particular, the energy resolution at high energies is achieved through the application of shower leakage corrections.

Each crystal element is read out by PIN photodiodes,

mounted on both ends of the crystal, which measure the scintillation light that is transmitted to each end. The difference in light levels provides a determination of the position of the energy deposition along the CsI crystal. There are two photodiodes at each end of the crystal, a large photodiode with area 147 mm<sup>2</sup> and a small photodiode with area 25 mm<sup>2</sup>, providing two readout channels to cover the large dynamic range of energy deposition in the crystal. The large photodiodes cover the range 2 MeV – 1.6 GeV, while the small photodiodes cover the range 100 MeV – 70 GeV. Each crystal end has its own front-end electronics and pre-amplifier electronics assembly. Both low and high energy signals go through a pre-amplifier and shaper and then a pair of Track and Hold circuits with gains differing nominally by a factor of eight. An energy domain selection circuit routes the best energy measurement through an analog multiplexer to an Analog to Digital Converter. A calibration charge injection signal can be fed directly to the front end of the pre-amplifiers.

The position resolution achieved by the ratio of light seen at each end of a crystal scales with the deposited energy and ranges from a few millimeters for low energy depositions ( $\sim 10$  MeV) to a fraction of a millimeter for large energy depositions ( $>1$  GeV). Simple analytic forms are used to convert the light asymmetry into a position (see Figure 7).

Although the calorimeter is only 8.6 radiation lengths deep, the longitudinal segmentation enables energy measurements up to a TeV. From the longitudinal shower profile, an unbiased estimate of the initial electron energy is derived by fitting the measurements to an analytical description of the energy-dependent mean longitudinal profile. Except at the low end of the energy range, the resulting energy resolution is limited by fluctuations in the shower leakage. The effectiveness of this procedure was evaluated in beam tests with the flight-like calibration unit at CERN. Figure 8 shows the measured energy loss and the leakage-corrected energy loss in the calorimeter for electron beams of various energies. Further details of the calorimeter are in Grove et al. (2008), Johnson et al. (2001), and Ferreira et al. (2004). Details of the energy reconstruction are discussed in §2.4.2.

### 2.2.3. Anticoincidence detector

The purpose of the ACD is to provide charged-particle background rejection; therefore its main requirement is to have high detection efficiency for charged particles. The ACD is required to provide at least 0.9997 efficiency (averaged over the ACD area) for detection of singly charged particles entering the field-of-view of the LAT.

The LAT is designed to measure  $\gamma$ -rays with energies up to at least 300 GeV. The requirement to measure photon energies at this limit leads to the presence of a heavy calorimeter ( $\sim 1800$  kg) to absorb enough of the photon-induced shower energy to make this measurement. The calorimeter mass itself, however, creates a problem we call the backsplash effect: isotropically distributed secondary particles (mostly 100–1000 keV photons) from the electromagnetic shower created by the incident high-energy photon can Compton scatter in the ACD and thereby create false veto signals from the recoil electrons. This effect was present in EGRET, where the instrument detection efficiency above 10 GeV was a factor of at least two or more lower than at 1 GeV due to false vetoes caused by backsplash. A design requirement was established that vetoes created by backsplash (self-veto) would reject not more than 20% of otherwise accepted photons at 300 GeV. To suppress the backsplash effect, the ACD is segmented so that

only the ACD segment nearby the incident candidate photon may be considered, thereby dramatically reducing the area of ACD that can contribute to backscatter (Moiseev et al. 2004). In addition, the onboard use of the ACD veto signals is disengaged when the energy deposition in the calorimeter is larger than an adjustable preset energy (10 to 20 GeV). Such events are subsequently analyzed using more complex software than can be implemented on board.

Numerous trade studies and tests were performed in order to optimize the ACD, resulting in the design shown schematically in Figure 9. Plastic scintillator tiles were chosen as the most reliable, efficient, well-understood, and inexpensive technology, with much previous use in space applications. Scintillation light from each tile is collected by wavelength shifting fibers (WLS) that are embedded in the scintillator and are coupled to two photomultiplier tubes (PMTs) for redundancy. This arrangement provides uniformity of light collection that is typically better than 95% over each detector tile, only dropping to >75% within 1–2 cm of the tile edges. Overall detection efficiency for incident charged particles is maintained by overlapping scintillator tiles in one dimension. In the other dimension, gaps between tiles are covered by flexible scintillating fiber ribbons with >90% detection efficiency.

To minimize the chance of light leaks due to penetrations of the light-tight wrapping by micrometeoroids and space debris, the ACD is completely surrounded by a low-mass micrometeoroid shield ( $0.39 \text{ g cm}^{-2}$ ).

All ACD electronics and PMTs are positioned around the bottom perimeter of the ACD, and light is delivered from the tiles and WLS fibers by a combination of wavelength-shifting and clear fibers. The electronics are divided into 12 groups of 18 channels, with each group on a single circuit board. Each of the 12 circuit boards is independent of the other 11, and has a separate interface to the LAT central electronics. The PMTs associated with a single board are powered by a High Voltage Bias Supply (HVBS), with redundant HVBS for each board. The tile readout has two thresholds: an onboard threshold of about 0.45 MIP for the initial rejection of charged particles, and a ground analysis threshold of about 0.30 MIP for the final analysis.

Further details of the ACD design, fabrication, testing, and performance are given by Moiseev et al. (2007). Table 4 is a summary of key parameters of the LAT ACD.

#### 2.2.4. Data acquisition system (DAQ) and trigger

The Data Acquisition System (DAQ) collects the data from the other subsystems, implements the multi-level event trigger, provides on-board event processing to run filter algorithms to reduce the number of downlinked events, and provides an on-board science analysis platform to rapidly search for transients. The DAQ architecture is hierarchical as shown in Figure 10. At the lowest level shown, each of 16 Tower Electronics Modules (TEMs) provides the interface to the tracker and calorimeter pair in one of the towers. Each TEM generates instrument trigger primitives from combinations of tower subsystem (tracker and calorimeter) triggers, provides event buffering to support event readout, and communicates with the instrument-level Event Builder Module that is part of the Global-trigger/ACD-module/Signal distribution Unit (GASU).

The GASU consists of (i) the Command Response Unit (CRU) that sends and receives commands and distributes the DAQ clock signal, (ii) the Global-Trigger Electronics Module (GEM) that generates LAT-wide readout decision signals

based on trigger primitives from the TEMs and the ACD, (iii) the ACD Electronics Module (AEM) that performs tasks, much like a TEM, for the ACD, and (iv) the Event Builder Module (EBM) that builds complete LAT events out of the information provided by the TEMs and the AEM, and sends them to dynamically selected target Event Processor Units (EPUs).

There are two operating EPUs to support on-board processing of events with filter algorithms designed to reduce the event rate from 2–4 kHz to  $\sim 400$  Hz that is then downlinked for processing on the ground. The on-board filters are optimized to remove charged particle background events and maximize the rate of  $\gamma$ -ray triggered events within the total rate that can be downlinked. Finally, the Spacecraft Interface Unit (SIU) controls the LAT and contains the command interface to the spacecraft. Each EPU and SIU utilizes a RAD750 Compact PCI Processor which, when operating at 115.5 MHz, provides 80 to 90 MIPS. The instrument flight software runs only on the EPUs and the SIU. The TEMs and the GASU hardware have software-controlled trigger configuration and mode registers.

Not shown in Figure 10 is the redundancy of the DAQ system or the LAT's Power Distribution Unit (PDU). There are two primary EPUs and one redundant EPU, one primary SIU and one redundant SIU, and one primary GASU and one redundant GASU. The PDU, which is also redundant, controls spacecraft power to the TEMs, the GASU, and the EPUs. The feeds from the spacecraft to the PDU are fully cross-strapped. In turn, the TEMs control power to the tracker and the calorimeter modules and the GASU controls power to the ACD. Power to the SIUs is directly provided by the spacecraft.

An instrument-level Trigger Accept Message (TAM) signal is issued by the GEM only if the GEM logic is satisfied by the input trigger primitives within the (adjustable) trigger window width. The TAM signal is sent to each TEM and to the AEM with no delays. Upon receipt of the TAM signal, a Trigger Acknowledge (TACK) signal with an adjustable delay is sent by the TEM to the tracker front-ends and a command, also with an adjustable delay, is sent to the calorimeter front-ends. The AEM sends a signal to the ACD front-ends. The TACK causes the entire instrument to be read out (e.g., addresses of hit strips in the tracker and TOT for each layer in each tracker module, and pulse heights for all 3,072 calorimeter channels and 216 ACD channels). Any of the TEMs or the AEM can issue a trigger request to the GEM. The time between a particle interaction in the LAT that causes an event trigger and the latching of the tracker discriminators is 2.3 to 2.4  $\mu\text{s}$ , much of this delay due to the analog rise times in the tracker front-end electronics. Similarly, the latching of the analog sample-and-holds for the calorimeter and the ACD are delayed (programmable delay of  $\sim 2.5 \mu\text{s}$ ) until the shaped analog signals peak.

The minimum instrumental dead time per event readout is 26.50  $\mu\text{s}$  and is the time required to latch the trigger information in the GEM and send it from the GEM to the EBM. The calorimeter readout can contribute to the dead time if the full four-range CAL readout is requested. During readout of any of the instrument, any TEM and the AEM send a “busy” signal to the GEM. From these signals, the GEM then generates the overall dead time and the system records this information and adds it to the data stream transmitted to the ground.

Any of the TEMs can generate a trigger request in several ways: (i) If any tracker channel in the tracker module is over

threshold, a trigger request is sent to the module's TEM which then checks if a trigger condition is satisfied, typically requiring triggers from 3  $x, y$  planes in a row. If this condition is satisfied, the TEM sends a trigger request to the GEM. (ii) If a predetermined low-energy (CAL-LO) or high-energy (CAL-HI) threshold is exceeded for any crystal in the calorimeter module, a trigger request is sent to the GEM.

The prompt ACD signals sent to the GEM are of two types: (i) a discriminated signal (nominal 0.4 MIPs threshold) from each of the 97 scintillators (89 tiles and 8 ribbons) of the ACD, used to (potentially) veto tracker triggers originating in any one of the sixteen towers, and (ii) a high-level discriminated signal (nominal 20 MIPs threshold) generated by highly ionizing heavy nuclei cosmic-rays (carbon-nitrogen-oxygen or CNO). The high-level CNO signal is used as a trigger, mostly for energy calibration purposes. During ground testing the CNO signal is only tested through charge injection. In addition, the GEM can logically group tiles and ribbons to form Regions Of Interest (ROIs) for trigger/veto purposes. An ROI can be defined as any combination of the ACD tiles and ribbons. Up to 16 ROIs can be defined through a series of configuration registers. The ROI signal is simply whether any one of the tiles that define the ROI is asserted.

Finally, non-detector based trigger inputs to the GEM are used for calibration and diagnostic purposes. The GEM can utilize (i) a periodic signal derived from either the instrument system clock (nominally running at 20 MHz) or the 1 pulse-per-second GPS spacecraft clock (accurate to  $\pm 1.5 \mu\text{s}$ ), and (ii) a solicited trigger signal input that allows the instrument to be triggered through operator intervention. The spacecraft clock is also used to strobe the internal time base of the GEM, thus allowing an accurate measurement of the time of an event relative to the spacecraft clock.

### 2.3. Instrument modeling

The development and validation of a detailed Monte Carlo simulation of the LAT's response to signals ( $\gamma$ -rays) and backgrounds (cosmic-rays, albedo  $\gamma$ -rays, etc.) has been central to the design and optimization of the LAT. This approach was particularly important for showing that the LAT design could achieve the necessary rejection of backgrounds expected in the observatory's orbit. The instrument simulation was also incorporated into an end-to-end simulation of data flow, starting with an astrophysical model of the  $\gamma$ -ray sky, used to support the pre-launch development of software tools to support scientific data analysis.

Figure 11 summarizes the various components of the instrument simulation, calibration, and data analysis. The instrument simulation consists of 3 parts: (i) particle generation and tracking uses standard particle physics simulators of particle interactions in matter to model the physical interactions of  $\gamma$ -rays and background particle fluxes incident on the LAT. In particular, the simulation of events in the LAT is based on the Geant4 (G4) Monte Carlo toolkit (Agostinelli et al. 2003; Allison et al. 2006), an object-oriented simulator of the passage of particles through matter. G4 provides a complete set of tools for detector modeling. In the LAT application, the simulation is managed by Gleam, our implementation of the Gaudi software framework (Barrand et al. 2001), and so we use only a subset of the G4 tools. (ii) For a given simulated event the instrument response (digitization) is calculated parametrically based on the energy deposition and location in active detector volumes in the anticoincidence detector, tracker, and calorimeter. (iii) From the digitized instrument

responses, a set of trigger primitives are computed and a facsimile of the Trigger and On-board Flight Software Filter (see §2.2.4) is applied to the simulated data stream. Events that emerge from the instrument simulation (or real data) then undergo event reconstruction and classification (§2.4), followed by background rejection analysis (§2.4.3). As discussed in §2.4.3, the background rejection can be tuned depending on the analysis objectives.

Information about the detector geometry and materials is stored in a set of structured XML files. These files are used by Gleam to build a G4 representation of the detector (and also to provide information about the detector to our event reconstruction packages). The geometry is quite detailed, particularly for the active elements, namely, the tracker silicon strip detectors, CsI crystals and diodes of the calorimeter, and anticoincidence detector scintillator tiles and ribbons. The current implementation has about 54,000 volume elements, of which about 34,000 are active.

G4 contains a full suite of particle interactions with matter, including multiple scattering and delta-ray production for charged particles, pair production and Compton scattering for photons, and bremsstrahlung for  $e^-$  and  $e^+$ , and low-energy interaction with atoms, as well as several models of hadronic interactions. The set of processes implemented is controlled by a "physics list," which allows for considerable flexibility. In fact, a special version of the model of multiple scattering is used to provide better agreement with our measured data.

Detector calibration data (thresholds, gains, non-uniformities, etc.) are used to convert the energy deposited in the active elements to instrument signals. For the tracker, dead channels are removed from the data at this stage, as well as any signals which would have overflowed the electronic buffers. (These same effects are taken into account again during event reconstruction, to aid the pattern recognition.)

### 2.4. Event reconstruction and classification

The event reconstruction processes the raw data from the various subsystems, correlating and unifying them under a unique event hypothesis. The development of the reconstruction relies heavily on the Monte Carlo simulation of the events. In the following subsections, the basic blocks of the reconstruction are described. We start with track reconstruction, as it is key to developing the subsequent analysis of the other systems: the found tracks serve as guides as to what should be expected in both the calorimeter as well as the ACD for various event types. The analogous reconstruction processing for EGRET, a spark-chamber pair conversion telescope, which did not benefit from a detailed Monte Carlo model of the instrument, is described in Thompson et al. (1993).

#### 2.4.1. Track reconstruction

Spatially adjacent hit tracker strips are grouped together, forming clusters, and the coordinates of these clusters are used in the track finding and fitting. Each cluster determines a precise location in  $z$  as well as either  $x$  or  $y$ . Because the planes of silicon detectors are arranged in closely spaced orthogonal pairs, both the  $x$  and  $y$  determinations can be made, albeit the choice of tracker technology (single-sided silicon strip detectors) imposes the ambiguities associated with projective coordinate readout on the initial pairing of the  $x$  and  $y$  coordinates when 2 or more particles pass through a detector plane. This ambiguity is resolved for tracks associated with particles that pass through more than one tracker module. For events with

tracks confined to one module, the coordinate-pairing ambiguity is resolved for  $\sim 90\%$  of these events using calorimeter information. Strictly, resolution of the coordinate-pairing ambiguity is only of secondary importance, having primarily to do with background rejection.

At the heart of track-finding algorithms is a mechanism to generate a track hypothesis. A track hypothesis is a trajectory (location and direction) that can be rejected or accepted based on its consistency with the sensor readouts. The generation algorithm is combinatoric, with a significant constraint imposed on the number of trial trajectories considered because of the available computing power. Two algorithms, described below, are used.

*Calorimeter-Seeded Pattern Recognition (CSPR):* For most of the LAT science analysis, some energy deposition in the calorimeter is required. When present, both the centroid and shower axis of the calorimeter energy deposition can be computed using a moments analysis (see §2.4.2) in most cases. The first and most-often selected algorithm is based on the assumption that the energy centroid lies on the trajectory. The first hit on the hypothesized track, composed of an  $x, y$  pair from the layer in the tracker furthest from the calorimeter, is selected at random from the possible  $x, y$  pairs. If a subsequent hit is found to be close to the line between the first hit and the location of the energy centroid in the calorimeter, a track hypothesis is generated. The candidate track is then populated with hits in the intervening layers using an adaptation of Kalman fitting (e.g., Frühwirth et al. 2000). The process starts from the first hit. A linear projection is made into the next layer. The covariance matrix is also propagated to the layer and provides an estimate of the error ellipse that is searched for a hit to add to the track. The propagation of the covariance matrix includes the complete details of the material crossed, thereby providing an accurate estimate of the error caused by multiple scattering. If a candidate hit exists in the layer, it is incorporated into the trajectory weighted by the covariance matrices. The procedure is then iterated for subsequent layers, allowing for missing hits in un-instrumented regions. Adding more hits to the track is terminated when more than a specified number of gaps (planes without hits associated with the track) have accumulated (nominally 2). The whole process is repeated, starting with each possible  $x, y$  pair in the furthest plane from the calorimeter and then continued using pairs from closer layers. After a track of sufficient quality is found and at least two layers have been looped over, the process is terminated.

A byproduct of this process is the first Kalman fit to the track, providing the  $\chi^2$ , the number of hits, the number of gaps, etc. From these quantities a track quality parameter is derived and used to order the candidate tracks from “best” to “worst”.

At high energies ( $>1$  GeV) the first-hit search is limited to a cone around the direction provided by the calorimeter moments analysis in order to minimize confusion with hits caused by secondary particles generated by backscatter. The cone angle is narrowed as the energy increases, reflecting the improved directional information provided by the calorimeter.

Following the completion of the CSPR, only the “best” track found is retained. The biasing caused by the track quality parameters makes this “the longest, straightest track” and hence, for  $\gamma$  conversions, preferentially the higher-energy track of the  $e^+e^-$  pair. The other tracks are discarded. The hits belonging to the best track are flagged as “used” and a second combinatoric algorithm is then invoked.

*Blind Search Pattern Recognition (BSPR):* In this algorithm, calorimeter information is not used for track finding. Events having essentially no energy deposition in the calorimeter are analyzed using this algorithm as well as for subsequent track finding following the stage detailed above. The same procedure described for the CSPR is used, but here the selection of the second hit used to make the initial trajectory is now done at random from the next closest layer to the calorimeter. The trajectory formed by these two hits is projected into the following layer and if a hit in that layer lies sufficiently close to the projection a trial track is generated. The mechanism of populating the track candidate with hits follows that used in the CSPR, but without any estimation of the energy of the track, the multiple scattering errors are set by assuming a minimum energy (default: 30 MeV). Hits are allowed to be shared between tracks if the hit is the first hit on the best track (two tracks forming a vertex) or if the cluster size (number of strips) is larger than expected for the track already assigned to that hit. The total number of tracks allowed to be found is limited (default: 10).

The final track fits must await an improved energy estimate to be made using the best track to aid in estimating the fraction of energy deposited in the calorimeter (see §2.4.2). Once this is done, the energy is apportioned between the first two tracks according to the amount of multiple scattering observed on each. A subsequent Kalman fit is done but without repopulating the tracks with hits.

The final stage of track reconstruction combines tracks into vertices. The process begins with the best track. The second track is selected by simply looping over the other tracks in the event. The distance of closest approach between the best track and the candidate second track is computed and if within a specified distance (default: 6 mm) a vertex solution is generated by covariantly combining the parameters of the two tracks. The  $z$ -axis location (coordinate along the instrument axis) of the vertex candidate is selected using the detailed topology of the first hits and is assigned either to be in the center of the preceding tungsten foil radiator, in the silicon detector itself, or within the core material of the tracker tray directly above the first hit. A quality parameter is created taking into account the  $\chi^2$  for the combination of tracks, the distance of closest approach, etc. The first track is paired with the second track having the best quality parameter. These tracks are marked as “used” and the next unused track is selected and the process repeated. If a track fails to make a satisfactory vertex it is assigned to a vertex by itself. Thus all tracks are represented by a vertex.

In addition to the “standard” vertexing discussed above, an additional improvement is possible if calorimeter information is included. In events where either during the conversion process or immediately thereafter much of the energy is in  $\gamma$ -rays (due to Bremsstrahlung or radiative corrections), the charged tracks can point well away from the incident  $\gamma$ -ray direction. However the location of the conversion point is usually well determined and, when combined with the energy centroid location in the calorimeter, can give a fair estimate of the direction. The “best” track as well as the first vertex are combined covariantly with this direction using weights to apportion the total energy between these directions. These “neutral energy” solutions result in significantly reducing the non-gaussian tails of the PSF.

Energy reconstruction begins by first applying the appropriate pedestals and gains to the raw digitized signals. Then, for each calorimeter crystal, the signals from the two ends are combined to provide the total energy in the crystal (independent of location) and the position along the crystal where the energy was deposited. The result is an array of energies and locations.

The three-dimensional calorimeter energy centroid is computed along with energy moments (similar to the moment of inertia, but with energy in place of mass). The shower direction is given by the eigenvector with the smallest eigenvalue. Initially, the overall energy is taken to be the sum of the crystal energies (“CALEnergyRaw” in Figure 8). Further improvements must await the completion of the fitted tracks.

The trajectory provided by the best track (or best track vertex when available) is used as input to estimate the energy correction necessary to account for leakage out the sides and back of the calorimeter and through the internal gaps between calorimeter modules. Three different algorithms are applied to each event: a parametric correction (PC) based on the barycenter of the shower, a fit to the shower profile (SP) taking into account the longitudinal and transverse development of the shower, and a maximum likelihood (LK) fit based on the correlations of the overall total energy deposited with the number of hits in the tracker and with the energy seen in the last layer. Because the SP method starts to work beyond 1 GeV and the LK method works below 300 GeV, only the PC method covers the entire phase space of the LAT. Figure 8 shows the results of the LK method applied to data obtained with electron beams at CERN entering the LAT calibration unit at an angle of  $45^\circ$  to the detector vertical axis. The energy resolutions obtained vary between 4% at 5 GeV and 2% at 196 GeV.

At low energy ( $\sim 100$  MeV), a significant fraction ( $\sim 50\%$ ) of the energy in a  $\gamma$  conversion event can be deposited in the tracker and hence the determination of this contribution to the total energy becomes important. For this purpose the tracker is considered to be a sampling calorimeter where the number of hit silicon strips in a tracker layer provides the estimate of the energy deposition at that depth. The total number of hits in the thin radiator section, the thick radiator section and the non-radiator last layers is computed within a cone with an opening angle which decreases as  $E^{-1/2}$ , where  $E$  is the apparent energy in the calorimeter. The “tracker” energy is added to the corrected calorimeter energy.

Because the PC method gives an energy estimate for all events, it is used to iterate the Kalman track fits as mentioned in §2.4.1.

### 2.4.3. Background rejection

The vast majority of instrument triggers and subsequently downlinked data are background events caused by charged particles as well as earth albedo  $\gamma$ -rays. The task of the hardware trigger is to minimize their effects on the instrumental deadtime associated with reading out the LAT. Subsequently the task of the onboard filter is to eliminate a sufficient number of background events without sacrificing celestial  $\gamma$ -ray events such that the resulting data can be transmitted to the ground within the available bandwidth. The final task is for the analysis on the ground to distinguish between background events and  $\gamma$ -ray events and minimize the impact of backgrounds on  $\gamma$ -ray science. The combination of these 3 elements reduces the background by a factor of almost  $10^6$  while preserving efficiency for  $\gamma$ -rays exceeding 75%. For refer-

ence, the average cosmic  $\gamma$ -ray event rate in the LAT is  $\sim 2$  Hz.

#### 2.4.3.1 Background model

In order to facilitate the development of the on-board triggering and filtering and subsequent event reconstruction and classification algorithms, a model of the background the LAT encounters in space has been developed.

As shown in Table 5, the background model includes cosmic rays and earth albedo  $\gamma$ -rays within the energy range 10 MeV to  $10^6$  MeV. Any particles that might either make non-astrophysical  $\gamma$ -rays and/or need to be rejected as background are included. The model does not include X-rays or soft  $\gamma$ -rays that might cause individual detectors within the LAT to be activated. The model is meant to be valid outside the radiation belts and the South Atlantic Anomaly (SAA); no particle fluxes from inside the radiation belts are included. The boundaries of the belts are defined to be where the flux of trapped particles is 1 proton  $\text{cm}^{-2} \text{s}^{-1}$  ( $E > 10$  MeV). LAT does not take data inside the SAA. The fraction of time spent in the SAA is 14.6%.

The AMS (Aguilar et al. 2002) and BESS (Haino et al. 2004) experiments provided important and accurate new measurements of the spectra of the protons and alpha particles, the most abundant of the various galactic cosmic-ray (GCR) components. AMS made detailed latitude-dependent measurements of the splash and reentrant albedo particles ( $e^+$ ,  $e^-$  and protons) in the energy range from  $\sim 150$ – $200$  MeV up to the cutoff energies where the earth albedo components become lost in the much greater GCR fluxes. These fluxes will be updated with results from the Pamela satellite (Picozza et al. 2007).

For albedo fluxes of particles with energies below  $\sim 150$  MeV, inaccessible to the AMS and other large instruments, measurements made by NINA and NINA-2 and a series of Russian satellite experiments with an instrument known as Mariya are used. The albedo  $\gamma$ -ray fluxes are taken from a reanalysis of the data collected by EGRET when the CGRO satellite was pointed at the Earth.

The model is based on empirical fits to the referenced data. No time variability is included. The GCR fluxes are taken to be the same as those observed near solar minimum (maximum GCR intensities). The albedo fluxes may vary with time and be correlated with the GCR fluxes. The fluxes as observed by the NINA and Mariya experiments are used without correcting them for solar cycle variations. While an East-West cutoff variation was included that affects galactic cosmic ray components, all fluxes except albedo protons are assumed to be isotropic. The measurements are not complete enough for us to be able to account for variation in parameters such as the zenith angle of the particles or their pitch angles with respect to the local field. We have attempted to model some the zenith angle dependence for albedo protons, based not on measurements, but on modeling of the albedo (Zucon et al. 2003). Further verification and improvement to the model are being done on orbit.

The orbit averaged background fluxes in the model are shown in Figure 12. For charged particles, these fluxes are integrated over solid angle. It is straightforward to obtain fluxes per unit solid angle. For galactic cosmic ray components, divide by 8.7 sr, the solid angle of the visible sky that is not blocked by the Earth at *Fermi*'s orbital altitude. For the albedo components we have taken the reentrant and albedo fluxes to be the same.

### 2.4.3.2 Event classification and background rejection

After track reconstruction, vertexing, and energy reconstruction, the events are analyzed to determine the accuracy of the energy determinations, the directional accuracy, and whether they are  $\gamma$ -rays.

All of the estimates are based on classification tree (CT) generated probabilities. This statistical tool was found to give the highest efficiency with the greatest purity, exceeding that which we obtained with either a more traditional cut-based analysis or with neural nets. Our usage of classification trees involves training a modest number of trees (a few to  $\sim 10$ ) and averaging over the results. The trees are “grown” by minimizing “entropy” as defined in statistics (Breiman et al. 1984).

The final energy estimate for each event is made by first dividing the sample up into subsets according to which energy methods were reporting results (PC+LF+SP, PC+LF, PC+SP, and PC). When more than one energy method is available, the method selected is determined using a CT. The probability that the selected energy is better than the  $1\sigma$  resolution limit is estimated using a second CT. The subsets are then merged, now with a single “best” energy and a probability “knob” that can be used to lessen the presence of tails (both high and low) in the distribution of reconstructed energies at the expense of effective area.

The analysis sorts the events according to where they occurred in the LAT tracker. (Events in the thick radiator portion have about a factor of 2 worse angular resolution due to increased multiple scattering.) When there is sufficient energy in the calorimeter (default:  $>10$  MeV), the neutral energy solutions are used. If a 2-track vertex is present, a CT determines whether the vertex derived direction or the best track direction is used. As such there are four basic subsets: thin and thick radiator events and vertexed and 1-track events. For each of these subsets the probability that the reconstructed direction is more accurate than the theoretical 68% containment PSF is determined using a CT. The events are re-merged now with a “best” direction solution and associated CT-based probability. This image “knob” can be used to limit the long tails often associated with the PSFs of  $\gamma$ -ray instruments.

The background rejection is by far the most challenging of all the reconstruction analysis tasks. This is due to the large phase space covered by the LAT and the very low signal-to-noise ratio in the incoming data ( $\sim 1:300$  for down-linked data). The first task is to eliminate the vast majority of the charged particle flux that enters within the FoV using the ACD in conjunction with the found tracks. One cannot simply demand that there are no triggers from the ACD because high-energy  $\gamma$ -rays generate a considerable amount of back splash, from the shower that develops in the calorimeter, in the form of hard X-rays that can trigger several ACD tiles. Consequently only the tiles pointed at by the reconstructed tracks are used to establish a veto by the presence of a signal in excess of  $\sim 1/4$  of a minimum ionization event. Because the accuracy of the pointing is energy dependent due to multiple scattering, at low energy, only tiles within the vicinity of the track intersection with the ACD are used, while at high energy the region is restricted to essentially the one tile being pointed to. In addition there are several areas in the ACD where it is not possible to completely cover the acceptance region (e.g. the four vertical edge corners, the screw holes used to mount the tiles, etc.). Since these are known locations, tracks pointing at them must also be eliminated. However, these holes are small and account for a few percent of the surface area and

reduce the events sample by  $<2\%$ .

The considerations for rejecting backgrounds involve the detailed topology of the events within the tracker and the overall match of the shower profile in 3D in both the tracker and the calorimeter. The tracker provides a clear picture of the initial event topology. For example the identification of a 2-track vertex immediately reduces the background contamination by about an order of magnitude. However a majority of events above 1 GeV don’t contain such a recognizable vertex due to the small opening angle of the  $e^+e^-$  pair along the incoming  $\gamma$ -ray direction. The observation of a significant number of extra hits in close proximity to the track(s) indicates they are electrons and hence from the conversion of a  $\gamma$ -ray while the presence of unassociated hits or tracks are a strong indicator of background. These as well as other considerations are used for training background rejection CTs.

The final discriminator of background is the identification of an electromagnetic shower. Considerations such as how well the tracker solution points to the calorimeter centroid, how well the directional information from the calorimeter matches that of the track found in the tracker, as well as the width and longitudinal shower profile in the various layers of the calorimeter, are important in discrimination of backgrounds. Again the information from the reconstruction is used to train CTs and the resulting probability is used to eliminate backgrounds.

The broad range of LAT observations and analysis, from GRBs to extended diffuse radiation, leads to different optimizations of the event selections and different rates of residual backgrounds. For example, in analysis of a GRB, the relatively small region of the sky as well as the very short time window allow the background rejection cuts to be relaxed relative to an analysis of a diffuse source covering a large portion of the sky. Furthermore a key science attribute for GRB observations is the time evolution and the sensitivity of a measurement to rapid time variation scales as the square root of the number of detected burst photons. The background rejection analysis has been constructed to allow analysis classes to be optimized for specific science topics.

Table 6 lists 3 analysis classes that have been defined based on the backgrounds expected in orbit, current knowledge of the  $\gamma$ -ray sky, and the performance of the LAT. Our estimates of LAT performance are given in terms of these analysis classes. Common to all of these analysis classes is the rejection of the charged-particle backgrounds entering within the field of view. The classes are differentiated by an increasingly tighter requirement that the candidate photon events in both the tracker and the calorimeter behave as expected for  $\gamma$ -ray induced electromagnetic showers. The loosest cuts apply to the Transient class, for which the background rejection was set to allow a background rate of  $<2$  Hz, estimated using the background model described in §2.4.3, which would result in no more than one background event every 5 sec inside a  $10^\circ$  radius about a source. The Source class was designed so that the residual background contamination was similar to that expected from the extragalactic  $\gamma$ -ray background flux over the entire field of view. Finally, the Diffuse class has the best background rejection and was designed such that harsher cuts would not significantly improve the signal to noise. The various analysis cuts and event selections will be optimized for the conditions found on-orbit during the 1st year all-sky survey phase. Note that these 3 analysis classes are hierarchical; that is all events in the Diffuse class are contained in the Source class and all events in the Source class are in the

Transient class.

The residuals of background events for the 3 analysis classes are shown in Figure 13. For the Diffuse class, the resulting rejection factor is  $\sim 1:10^6$  at some energies (e.g.,  $\sim 10$  GeV) while retaining  $>80\%$  efficiency for retaining  $\gamma$ -ray events. The residual background is worse at low energy particularly for events originating in the thick radiator portion of the tracker. It is here that “splash” backgrounds, entering the backside of the calorimeter can undergo interactions that result in low energy particles which range out in the thick radiator, thus mimicking an event originating in the thick tracker section. In a sense the thick section shields the thin section from this flux and hence the thin section is somewhat cleaner.

The leaked background events generally fall into two categories: irreducible events and reducible events. The irreducible events are events in which a background particle interacts in the passive material outside the ACD or within the first  $\sim 1$  mm of the ACD scintillator and the resulting secondaries contain  $\gamma$ -rays which enter inside the FoV. This can happen in the case of entering  $e^+$  which annihilate to two photons, entering  $e^-$  or  $e^+$  which bremsstrahlung essentially all their energy to a single photon, and proton interactions that make a  $\pi^0$  which decays to 2 photons with the rest of the secondaries either neutral or aimed away from the LAT. In these cases the ACD has no signals and a  $\gamma$ -ray is seen in the LAT. There is no way in principle to distinguish and eliminate these events from the celestial  $\gamma$ -ray signal and this component is the result of the reality of contemporary instrumentation and the precautionary measures that must be taken to survive in low earth orbit. This irreducible component constitutes  $\sim 60\%$  of the residual background events with measured energies above 100 MeV.

The reducible background component comprises events that in principle should be identifiable. These events leak through the various filters because they are in the far tails of their parent distributions, overlapping the  $\gamma$ -ray (signal) distribution. The filter parameters are chosen to optimize efficiency for  $\gamma$ -rays versus background rejection. Additional contributions to the reducible background component come from the fact that any real detector will have inefficiencies caused by real world design choices such as gaps in the silicon detector planes of the tracker and in the ACD. This reducible component however is easily monitored by comparing the apparent fluxes of events with and without vertices. The difference is essentially the reducible component because the vertexed event sample has 10 times fewer such reducible background events.

### 2.5. Performance of the LAT

The performance of the LAT is basically determined by the design of the LAT hardware, the event reconstruction algorithms (i.e., the accuracy and efficiency with which the low-level event information is used to determine energy and direction), and event selection algorithms (i.e., the efficiency for identifying well reconstructed  $\gamma$ -ray events).

Figures 14 – 18 summarize the performance of the LAT. The performance parameters are subject to change as event selection algorithms are further optimized, particularly during the early part of on-orbit operations of *Fermi*. For the most up-to-date performance parameters go to [http://www-glast.slac.stanford.edu/software/IS/glast\\_lat\\_performance.htm](http://www-glast.slac.stanford.edu/software/IS/glast_lat_performance.htm).

Figure 14 shows the on-axis effective area versus energy for each of the analysis classes defined in Table 6. Contributions from conversions in both the thin and thick sections of the

tracker are included, with each contributing about 50% of the effective area. Note that the peak effective area, near 3 GeV, is nearly the same for all 3 analysis classes, while at energies below 300 MeV the effective area for the transient class is a factor of  $\sim 1.5$  larger than the for the diffuse class. Figure 15 shows the effective area for the source class on-axis and at  $60^\circ$  off-axis. Figure 16 shows the telescope’s acceptance, the average effective area times the field-of-view. Again, the differences between the analysis classes are largest at low energies.

Figure 17 shows the energy dependence of the 68% containment radius (space angle) for  $\gamma$ -ray conversions in the thin section of the tracker that are incident either on-axis or at  $60^\circ$  off-axis for the source class. The PSF for  $\gamma$ -rays converting in the thick section of the tracker is about twice as wide.

Figure 18 shows the energy resolution of the LAT versus energy for the source class.

With a diffuse  $\gamma$ -ray background model based on EGRET observations and the instrument performance summarized above, the source sensitivity of the LAT can be estimated. The source sensitivity of course depends not only on the flux of the source but it also depends on the spectrum of the source. Figure 19 shows the integral source flux above energy  $E$  versus energy corresponding to a  $5\sigma$  detection after one year of scanning mode observations. Figure 20 shows the differential source flux (in  $1/4$  decade bins) corresponding to a  $5\sigma$  detection.

#### 2.5.1. LAT performance tests

The design of the LAT was optimized using Monte Carlo simulations. Verification of the design and simulations was done with a series of beam tests at the SLAC, CERN and GSI heavy ion accelerator laboratories. In addition hardware prototypes as well as the flight instrument have been tested using cosmic rays. The early prototype tests at SLAC have already been mentioned. The most extensive beam test was at CERN in 2006. The CERN beams were selected because they cover almost the entire energy range of the LAT for on-orbit operations as well as provide large fluxes of hadrons to verify the modeling of background interactions within the LAT. Because schedule prevented doing beam tests with the entire LAT, a Calibration Unit (CU) consisting of two complete tracker and 3 calorimeter modules was assembled. The CU readout electronics is a copy of the flight instrument data acquisition system. The CU is also instrumented with several ACD scintillator tiles to measure the backsplash response from the calorimeter at high energies. The overall agreement between the Monte Carlo simulations of the CU and the beam test data are excellent, including the overall tracker performance and the PSF, the backsplash into the ACD, and the modeling of hadronic interactions. The largest discrepancies involve the energy calibration in the calorimeter which was found to be low by  $\sim 7\%$ . A much more complete discussion of the preliminary beam test results, comparing the CU to the Monte Carlo simulations can be found in Baldini et al. (2007).

In addition to the accelerator beam tests, several times during the assembly of the LAT, cosmic ray triggers were recorded to verify the proper functioning of the LAT modules as they were added to the instrument array. Collection of cosmic-ray data, recorded at a trigger rate of  $\sim 400$  Hz, continued through the environmental testing and pre-launch preparations of the *Fermi* telescope. While terrestrial cosmic rays are quite messy (e.g., multiple particle types, range of arrival directions) compared to a particle beam from an accelerator,

the LAT has sufficient power as a particle detector to provide clean samples of sea-level muons, resulting in relatively large samples of muon events that allow precision testing. With these events, calibrations, efficiencies, and alignment issues were successfully addressed.

The first 60 days after launch were a commissioning period for the *Fermi* spacecraft and the LAT. During part of this period the LAT was subjected to a relatively high rate albedo photon data by pointing at the earth's limb, and directly observed the "splash" albedo background component with nadir pointed runs, as well as run with modified triggers to allow high-energy cosmic rays to be efficiently collected to verify alignment and efficiencies that may have been affected during the launch. The early operations tests included checks of internal timing and absolute timing, subsystem calibrations, characterization of the perimeter of the South Atlantic Anomaly, tuning the onboard event filters, and commissioning the on-board detection of GRBs.

## 2.6. Instrument operations

### 2.6.1. Onboard science processing

A primary objective of onboard science processing is to provide rapid detection and localization of GRBs. The output of this processing can trigger an autonomous re-pointing of the *Fermi* to keep the GRB within the LAT FoV for observation of high-energy afterglows and is made available to support follow-up observations of afterglows by other observatories. The *Fermi* Gamma-ray Burst Monitor also produces onboard detections and localizations, however for burst that trigger the LAT, the LAT's better point spread function results in significantly improved localization. The onboard estimates of the celestial coordinates of the GRB and the error region are distributed via the Gamma-ray burst Coordinate Network (GCN).

The onboard science processing consists of algorithms to (1) select  $\gamma$ -ray candidate events, (2) reconstruct directions of  $\gamma$ -ray candidate events and (3) search for and localize high energy transients.

The information available to the onboard GRB search algorithm differs substantially from that eventually available on the ground. The event selection is based on parameters previously calculated for the onboard filter (described in §2.2.4). The onboard software uses fairly simple, computationally efficient algorithms to calculate the directions of candidate  $\gamma$ -ray events. The efficiency for successfully reconstructing an event direction is within 25% of what can be achieved with subsequent ground processing however, the reconstructed directions are about a factor of 2 to 5 worse.

The onboard GRB detection algorithm utilizes both the temporal and spatial characteristics of GRBs. It works by associating a probability for a cluster of tracks to be located on a small part of the sky during a short interval of time.  $\gamma$ -ray candidate events with reconstructed directions are fed to the algorithm in time order. The algorithm searches a list of the  $n$  most recent events for the cluster of events that has the smallest probability of occurring in time and space. If the probabilities pass a pre-selected threshold, the time and location of the cluster is passed to a second stage of processing which considers events over a longer time interval. A GRB is declared when cluster probabilities in the second stage exceed a pre-defined threshold. The algorithm will then calculate refined localizations on a configurable sequence of time intervals. The initial burst location and each updated lo-

cation is sent promptly to the ground via the Tracking and Data Relay Satellite System (TDRSS) and then to the GCN (<http://gcn.nasa.gov/>). The GCN provides locations of GRBs (the Notices) detected onboard by the LAT or the GBM and reports on follow-up observations (the Circulars and the Reports) made by ground-based and space-based optical, radio, x-ray, TeV, and other observers.

Triggering on bursts depends on settable parameter choices. We used a phenomenological burst simulator and background model to guide the initial choice of filter parameter values. These parameters will be optimized once a large enough sample of bursts has been identified via ground reconstruction.

### 2.6.2. Pipeline and data products

LAT science data arrive at the LAT Instrument Science Operations Center (ISOC) from the *Fermi* Mission Operations Center at about 3 hour (2 orbits) intervals, 24 hours per day, in approximately 1.5 GB downlinked data sets. Automated processing of the data implements several analysis functions. The primary function is to interpret the event data, via pattern recognition and reconstruction, to indicate the nature of the event as either celestial  $\gamma$ -ray photons or background, and determine the direction, arrival time, and energy and provide estimates of the associated errors. During the process of correlating data from all the subsystems, detailed information is available on the operation of the LAT and is collected and trended for monitoring purposes. Once the photons have been isolated, the level-1 data are immediately used to carry out several higher level science analysis tasks that include searching for and refining GRB properties; searching for flaring sources; and tracking the light curves of a pre-selected list of sources.

The processing pipeline is designed to allow parallel processing of events, with dependencies enabled so that processes can wait for the parallel processing to finish before aggregating the results. It can process an arbitrary graph of tasks. The pipeline is run in a java application server and interacts with farms of batch processors. About 300 Hz of downlinked on-orbit data can be processed by 100 computing cores within 1-2 hours, allowing processing to finish before the next downlink arrives. Reconstruction inflates the raw science data volume by approximately a factor of 20. Keeping all events processed requires about 150 TB of disk per year. The total LAT pipeline processing compute facility is sized to accommodate prompt processing, reprocessing and simulations. 300 computing cores for reprocessing of data, allow one year of data to be reprocessed in about one month. This is an upper limit on the reprocessing time, since use will be made of the much larger user batch processor pool in the SLAC compute farm.

The reconstructed  $\gamma$ -ray photon events are then made available, along with instrument response functions and high-level analysis tools, etc., to the *Fermi* Science Support Center (FSSC) for distribution to the community at the conclusion of the first year on-orbit verification and sky-survey phase and during subsequent mission phases. After completion of the verification and sky survey phase (year 1) of the mission, these data should arrive at the FSSC within about 3-4 hours after arrival of unprocessed data at the ISOC. Automated science processing operates on 3 time scales: per downlink, per week and per month. During year 1 as well as beyond, the ISOC will deliver high-level science data products, resulting from Automated Science Processing (ASP), to the FSSC. These include light curves and GCN notices and circulars for

GRBs and AGN flares as well as fluxes, source locations and associated errors for transient or flaring sources.

### 2.6.3. Automated science processing

Time critical analysis tasks related to detection and characterization of transient sources, referred to as Automated Science Processing (ASP), are performed on the reconstructed and classified events from the level-1 pipeline to facilitate timely follow-up observations by other observatories.

The ASP tasks relevant to GRBs (and other impulsive phenomena, such as solar flares) are the refinement of information for GRBs that were detected with onboard processing, the search for untriggered GRBs, and the rapid search for and characterization of  $\gamma$ -ray afterglow emission. In this context, untriggered means not triggered by the LAT; however, information about GRBs detected by the GBM and GCN notices from other observatories will be used in conjunction with this search. The baseline for ASP processing uses an unbinned likelihood analysis to determine the position and uncertainty of a GRB and evaluates the spectral index and fluence by fitting a power-law spectrum to the LAT events, also via an unbinned likelihood analysis. The refinement task uses a Bayesian Blocks temporal analysis (Scargle 1998; Jackson et al. 2005) to characterize the prompt burst light curve, and from that analysis, it determines the burst start time and duration. The search for untriggered GRBs uses an algorithm similar to the one developed for onboard detection; but since ASP analysis uses ground processed events, it benefits from a substantially lower residual background rate as well as from more accurate energy and directional reconstructions. Any independently-available information, such as directions and times of GRBs seen by other instruments, is used to increase the sensitivity of the search. The afterglow search uses an unbinned likelihood analysis to fit for a point source at the best-fit GRB position using a likelihood analysis on all data available for  $\sim 5$  hours after the time of the GRB. The principal products of ASP processing for GRBs are Notices and Circulars released via GCN; for GRB refinements the latency for release of these products will eventually be no more than 15 minutes from the availability of the necessary level-1 data. For GRB and afterglow searches the latency will be less than 1 hour. Overall catalogs of LAT GRBs will be produced by the LAT collaboration.

The ASP tasks relevant to blazars and other long-term transient sources relate to monitoring for episodes of flaring. For optimum sensitivity this involves both routinely evaluating the fluxes for a set of sources as well as searching for new transients not already on the list of monitored sources. The flux monitoring task uses an unbinned likelihood analysis to evaluate the fluxes and upper limits of a specified list of sources on daily and weekly bases. The ASP-monitored source list is not static – bright transients will be added as they are found, for example. The general search for flaring sources, to find transients that are not on the list of sources being monitored, is run on daily and downlink ( $\sim 3$ – $4$  hr) time scales. The baseline algorithm for this search monitors for changes in exposure-corrected maps of counts. Newly-detected transients meeting the detection criteria are released via GCN notices or Astronomers Telegrams (ATELs). The latency for updating daily light curves of monitored sources will eventually be less than 6 hours after the availability of the needed level-1 data. The general search for flaring sources is expected to take less than 1 hour per downlink.

The algorithms and event classification cuts used for the

ASP analyses are continuing to be refined during flight. The ASP processing tasks are built as part of the general pipeline system in the LAT ISOC, and are extensible as needed. A parallel set of tasks uses the LAT science data for the bright pulsars to validate the instrument response functions and to monitor the high-level performance of the LAT.

## 3. KEY SCIENCE OBJECTIVES

The LAT is designed to address a number of scientific objectives that include (i) resolving the  $\gamma$ -ray sky and determining the origins of diffuse emission and the nature of unidentified sources (§3.1), (ii) understanding the mechanisms of particle acceleration in celestial sources (§3.2), (iii) studying the high-energy behavior of GRBs and transients (§3.3), (iv) probing the nature of dark matter (§3.4), and (v) using high-energy  $\gamma$ -rays to probe the early universe (§3.5). The key objectives are largely motivated by the discoveries of EGRET ( $\sim 30$  MeV – 10 GeV) and of ground-based atmospheric Cherenkov telescopes (ACT) above  $\sim 100$  GeV. Progress in several areas requires coordinated multi-wavelength observations with both ground and space-based telescopes. The following sections describe how the LAT enables these scientific studies.

### 3.1. Resolve the $\gamma$ -ray sky: the origins of diffuse emission and the nature of unidentified sources

High-energy  $\gamma$ -ray sources are seen against a diffuse background of Galactic and extragalactic radiation. Particularly at low Galactic latitudes, the diffuse radiation is bright and highly structured. About 80% of the high-energy luminosity of the Milky Way comes from processes in the interstellar medium (ISM). Because these background emissions are themselves not completely understood, analysis is an iterative process. As sources are discovered and distinguished from the background, the diffuse background model can be improved, thus allowing better analysis of the sources (e.g., Hunter et al. 1997; Sreekumar et al. 1998; Hartman et al. 1999; Strong et al. 2004a).

#### 3.1.1. Unidentified EGRET sources

Although time signatures allowed identification of many EGRET sources as pulsars or blazars, in the third EGRET catalog (Hartman et al. 1999) 170 of the 271 sources had no firm identifications. Progress towards identifications has been limited primarily by the relatively large EGRET error boxes that often contain many potential counterparts.

A wide variety of astrophysical objects have been suggested as possible counterparts for some of these sources. Some examples are: newly-found radio or X-ray pulsars (e.g., Kramer et al. 2003; Halpern et al. 2001), isolated neutron stars (e.g., RX J1836.2+5925 Mirabal & Halpern 2001; Reimer et al. 2001; Halpern et al. 2002), star forming regions or association of hot and massive stars (e.g., Kaaret & Cottam 1996; Romero et al. 1999), supernova remnants (e.g., Sturmer & Dermer 1995; Esposito et al. 1996), pulsar wind nebulae (e.g., Roberts et al. 2001), and microquasars, such as LSI 61 $^{\circ}$ 303 (Tavani et al. 1998; Paredes et al. 2000). Figure-of-Merit approaches have increased the number of  $\gamma$ -ray sources at high Galactic latitudes identified, with moderate confidence, with blazars (Mattox et al. 2001; Sowards-Emmerd et al. 2003, 2004, 2005).

Population studies of the unidentified EGRET sources have also provided clues about their natures. For example, spatial-

statistical considerations and variability studies provide evidence for a population of Galactic and variable GeV  $\gamma$ -ray emitters among the unidentified EGRET sources (Nolan et al. 2003). Many sources may be related to star-forming sites in the solar neighborhood or a few kiloparsecs away along the Galactic plane (Gehrels et al. 2000). These sites harbor compact stellar remnants, SNRs and massive stars, i.e., many likely candidate  $\gamma$ -ray emitters. Evidence exists for a correlation with SNRs (Sturmer & Dermer 1995) as well as OB associations (Romero et al. 1999), reviving the SNOB concept of Montmerle (1979) or making the pulsar option attractive. Pulsar populations may also explain a large fraction of unidentified sources close to the Galactic plane (Yadigaroglu & Romani 1997) and possibly in the nearby starburst Gould Belt (Grenier 2000). Other candidate objects among the unidentified sources include radio-quiet neutron star binary systems (Caraveo et al. 1996) and systems with advection-dominated accretion flows onto a black hole such as Cygnus X-1, recently detected as a flaring source by MAGIC (Albert et al. 2007).

With regard to extragalactic sources, understanding the nature of the unidentified sources is important because new  $\gamma$ -ray emitting source classes (e.g., normal galaxies, clusters, etc.) are likely to be found in addition to the well-established blazars. A census of these sources is important for establishing their contribution to the extragalactic  $\gamma$ -ray background (EGRB; see §3.1.3). High-confidence detections and identifications of the first representatives of other extragalactic  $\gamma$ -ray sources, such as galaxy clusters (Dar & Shaviv 1995; Colafrancesco & Blasi 1998; Totani & Kitayama 2000; Loeb & Waxman 2000; Gabici & Blasi 2003), will enable comparisons and normalization of theoretical predictions of their contributions to the EGRB.

The LAT addresses these challenges with good source localization, energy spectral measurement over a broader range, and nearly continuous monitoring of sources for temporal variability. These capabilities greatly facilitate the source identification process in the following ways:

(1) *Provide good source localization for the majority of  $\gamma$ -ray sources, including all of the EGRET detected sources.* For  $5\sigma$  one-year LAT survey sources and for EGRET sources (Figure 21), the typical error box sizes (68% confidence radius) are  $2.5'$  and  $<0.4'$  respectively, for an  $E^{-2}$  source and  $12'$  and  $2'$  respectively, for a source with a spectral cut-off at  $\sim 3$  GeV, as anticipated for pulsars.

More precise source locations and smaller positional uncertainties are a prerequisite for more efficient and conclusive source identifications, with the exception of  $\gamma$ -ray variability that is tightly correlated with variability in another band. Small error boxes significantly reduce the number of potential counterparts at other wavebands. Better source localization will also improve spatial-statistical correlation studies by reducing the number of chance coincidences. Finally, a number of unidentified EGRET sources that are likely unresolved composite sources (e.g., Sowards-Emmerd et al. 2003), will be resolved into individual sources.

(2) *Measure source spectra over a broad energy range.* Determining  $\gamma$ -ray spectra with the LAT's resolution will allow investigation of features intrinsic to the sources such as absorption signatures, spectral breaks, transitions, and cut-offs (e.g., attenuation of blazar spectra at high-energy due to  $\gamma + \gamma \rightarrow e^+ + e^-$  in the extragalactic background light). The LAT's wide energy coverage will connect the GeV sky to ground-based very high energy  $\gamma$ -ray observations. For ex-

ample, LAT spans the energy range where the pulsed emission component in pulsars appears to fade out (a few GeV), to be dominated at higher energies by energetic synchrotron nebulae powered by the pulsar.

(3) *Measure  $\gamma$ -ray light curves over a broad range of timescales.* The large effective area, wide field of view, stability, and low readout deadtime of the LAT enable measurement of source flux variability over a wide range of timescales. Figure 22 illustrates this capability. Coupled with the scanning mode of operation, this capability enables continual monitoring of source fluxes that will greatly increase the chances of detecting correlated flux variability with other wavelengths. It allows periodicity and modulation searches, for example, for orbital modulation in close binaries. LAT sources can be investigated for potential periodicities on time scales of milliseconds to years, encompassing millisecond pulsars, pulsars and binary systems hosting a neutron star. Extrapolating from EGRET analyses of Geminga (e.g., Mattox et al. 1996; Chandler et al. 2001), the LAT sensitivity allows searches in sources as faint as  $\sim 5 \times 10^{-8}$  photons  $\text{cm}^{-2} \text{s}^{-1}$  ( $E > 100$  MeV) without prior knowledge of the period and period derivative from radio, optical, or X-ray observations (Atwood et al. 2006; Ziegler et al. 2008). Such a capability is crucial for revealing radio-quiet, Geminga-like sources (Bignami & Caraveo 1996) which are expected to contribute significantly to the galactic unidentified source population (Gonthier et al. 2007; Harding et al. 2007).

In general, variability can be a discriminator for different source populations, i.e., expected steadiness in the  $\gamma$ -ray emission in the case of molecular-cloud-related CR interactions,  $\gamma$ -rays from SNRs, starburst galaxies, or in galaxy clusters versus modulated or stochastic variable emission from Active Galactic Nuclei, Galactic relativistic jet sources, black hole or neutron stars in binary systems with massive stars, and pulsar wind nebulae.

Population studies for a prospective source class help to select the most promising individual candidate sources for carrying out deep multi-frequency identification campaigns based on their broadband non-thermal properties and also help with investigating common characteristics of the candidate population. For example, galaxy clusters, as a candidate population, can be characterized by mass as deduced from optical richness, by temperature and mass functions, by applying virial mass-over-distance constraints, and by observational characteristics such as the presence or absence of merger activity, the presence or absence of diffuse radio halos or indications of nonthermal spectral components in the hard-X-rays.

LAT observations should allow at least several members among each new candidate source populations to be individually discovered and characterized. In view of the large number of expected detections, most probably representing different source classes, confirmation of a given population as  $\gamma$ -ray emitters will require a common criteria for statistical assessment (e.g., Torres & Reimer 2005), as well as dedicated multiwavelength observing campaigns (e.g., Caraveo & Reimer 2007).

Given the advance for point-source detection provided by the LAT, anticipating new observational features presently unknown in GeV astrophysics is also important. Although speculative at present, GeV  $\gamma$ -ray phenomena might be found that initially, or ultimately, have no detectable correspondence in other wavebands (e.g., GeV forming galaxy clusters: Totani & Kitayama 2000; dark matter clumps: Lake 1990; Calcáneo-

Roldán & Moore 2000).

### 3.1.2. *Interstellar emission from the Milky Way, nearby galaxies, and galaxy clusters*

The diffuse emission of the Milky Way is an intense celestial signal that dominates the  $\gamma$ -ray sky. The diffuse emission traces energetic particle interactions in the ISM, primarily protons and electrons, thus providing information about cosmic-ray spectra and intensities in distant locations (e.g., Hunter et al. 1997). This information is important for studies of cosmic-ray acceleration and propagation in the Galaxy (Moskalenko & Strong 2005).  $\gamma$ -rays can be used to trace the interstellar gas independently of other astronomical methods, e.g., the relation of molecular  $H_2$  gas to CO molecule (Strong et al. 2004c) and hydrogen overlooked by other methods (Grenier et al. 2000). The diffuse emission may also contain signatures of new physics, such as dark matter, or may be used to put restrictions on the parameter space of supersymmetrical particle models and on cosmological models (see §3.4). The Galactic diffuse emission must also be modeled in detail in order to determine the Galactic and extragalactic  $\gamma$ -ray backgrounds and hence to build a reliable source catalog.

Accounting for the diffuse emission requires first a calculation of the cosmic-ray (CR) spectra throughout the Galaxy (Strong et al. 2000). A realistic calculation that solves the transport equations for CR species must include gas and source distributions, interstellar radiation field (ISRF), nuclear and particle cross sections and nuclear reaction network,  $\gamma$ -ray production processes, and energy losses. Finally, the spectrum and spatial distribution of the diffuse  $\gamma$ -rays are the products of CR particle interactions with matter and the ISRF.

One of the critical issues for diffuse emission remaining from the EGRET era is the so-called “GeV excess”. This puzzling excess emission above 1 GeV relative to that expected (Hunter et al. 1997; Strong et al. 2000) has shown up in all models that are tuned to be consistent with directly measured cosmic-ray nucleon and electron spectra (Strong et al. 2004a). The excess has shown up in all directions, not only in the Galactic plane. The origin of the excess is intensively debated in the literature since its discovery by Hunter et al. (1997).

The excess can be the result of an error in the determination of the EGRET effective area or energy response or could be the result of yet unknown physics (for a discussion of various hypotheses see Moskalenko & Strong 2005). Recent studies of the EGRET data have concluded that the EGRET sensitivity above 1 GeV has been overestimated (Stecker et al. 2008) or underestimated (Baughman et al. 2007) or imply different cosmic-ray energy spectra in other parts of the Galaxy compared to the local values (Strong et al. 2004a; Porter et al. 2008). If these possibilities are eliminated with high confidence then it may be possible to attribute it to exotic processes, e.g., dark matter annihilation products (de Boer et al. 2005). See, however, a discussion on limitations in the determination of the diffuse Galactic  $\gamma$ -ray emission using EGRET data and a word of caution in Moskalenko et al. (2007).

With its combination of good spatial and energy resolution over a broad energy range, the LAT can test different hypotheses. LAT measurements of the Galactic  $\gamma$ -radiation offer good uniformity and high sensitivity as well. As noted above, understanding the Galactic diffuse emission is critical to analysis of LAT sources and important for cosmic ray and dark matter studies. Optimizing this model over the entire sky will have a high priority in the early phases of the mission.

The same basic considerations needed for the development

of the model of Galactic diffuse  $\gamma$ -ray emission also apply to other galaxies that are candidates for study with the LAT. For example, the LAT will resolve the Large Magellanic Cloud in detail and, in particular, map the massive star-forming region of 30 Doradus. By detecting further members among the normal galaxies in our Local Group, and galaxies with enhanced star formation rates (e.g., Ultra Luminous Infrared Galaxies and starburst galaxies), LAT observations can establish independent measures of cosmic ray production and propagation. Both M31 and the Small Magellanic Cloud are predicted to be detectable with LAT (Pavlidou & Fields 2001), and the nearest starburst galaxies as well (Torres et al. 2004).

Galaxy clusters emitting high-energy  $\gamma$ -rays are, although well hypothesized, observationally not yet established emitters in the GeV sky (Reimer et al. 2003). Predictions for galaxy clusters as a candidate source class for detectable high-energy emission relate to observations of diffuse radio signatures (Giovannini et al. 1999; Feretti et al. 2004, and references therein), revealing the existence of relativistic electrons in a number of galaxy clusters. Further hints of the presence of nonthermal particles in galaxy clusters arise from observations of hard emission components in case of a few nearby but X-ray bright clusters (Rephaeli et al. 2008, and references therein). Similarly, large scale cosmological structure formation scenarios predict high-energy  $\gamma$ -ray emission from galaxy clusters at a level detectable for *Fermi*/LAT (Keshet et al. 2003).

Both particle acceleration in merger processes as well as injection of relativistic particles through feedback from AGN as cluster members can provide the mechanism to produce non-thermal particles energized well into the energetic regime of LAT and perhaps beyond. Since galaxy clusters can store cosmic rays (Berezinsky et al. 1997) injected either by AGNs or accelerated by primordial shocks,  $\gamma$ -rays can be produced in  $pp$  interactions via production and decay of neutral pions and from annihilating DM or supersymmetrical particles. However, weak constraints from measurements of the intercluster magnetic field ranging from 0.1  $\mu$ G to 1  $\mu$ G leave assessments of the total energy content, as well as the relative fraction in relativistic electrons and protons still open to speculation. The first clear detection of high-energy  $\gamma$ -ray emission from a galaxy cluster will undoubtedly constrain the baryonic particle content as well as the uncertainty in the estimates of the magnetic field, and consequently enable vastly improved modeling of galaxy clusters over the entire electromagnetic spectrum.

### 3.1.3. *Extragalactic diffuse emission*

An isotropic, apparently extragalactic component of the high-energy  $\gamma$ -ray sky was studied by EGRET (Sreekumar et al. 1998). This extragalactic  $\gamma$ -ray background (EGRB) is a superposition of all unresolved sources of high-energy  $\gamma$ -rays in the universe plus any truly diffuse component. A list of the contributors to the EGRB includes “guaranteed” sources such as blazars and normal galaxies (Bignami et al. 1979; Pavlidou & Fields 2002), and potential sources such as galaxy clusters (Ensslin et al. 1997), shock waves associated with large scale cosmological structure formation (Loeb & Waxman 2000; Miniati 2002), distant  $\gamma$ -ray burst events (Casanova et al. 2007), pair cascades from TeV  $\gamma$ -ray sources and UHE cosmic rays at high redshifts (so-called Greisen-Zatsepin-Kuzmin cut-off). A consensus exists that a population of unresolved AGN certainly contribute to the EGRB inferred from EGRET observations; however predictions range

from 25% up to 100% of the EGRB (Stecker & Salamon 1996; Mukherjee & Chiang 1999; Chiang & Mukherjee 1998; Mücke & Pohl 2000). A number of exotic sources that may contribute to the EGRB have also been proposed: baryon-antibaryon annihilation phase after the Big Bang (Stecker et al. 1971; Gao et al. 1990; Dolgov & Silk 1993), evaporation of primordial black holes (Hawking 1974; Page & Hawking 1976; Maki et al. 1996), annihilation of so-called weakly interacting massive particles (WIMPs) (Silk & Srednicki 1984; Rudaz & Stecker 1991; Jungman et al. 1996; Bergström et al. 2001; Ullio et al. 2002; Elsässer & Mannheim 2005), and strings (Berezinsky et al. 2001).

The EGRB is difficult to disentangle from the intense Galactic diffuse foreground (see previous section) because it is relatively weak and has a continuum spectrum with no strongly distinguishing features. Indeed, determination of the EGRB spectrum depends on the adopted model for the Galactic diffuse emission spectrum, which itself is not yet firmly established. Even at the Galactic poles, the EGRB does not dominate over the Galactic component, with its flux comparable to the Galactic contribution from inverse Compton scattering of the interstellar radiation from stars and dust near the Galactic plane and the cosmic microwave background (Strong et al. 2000; Moskalenko & Strong 2000). The determination of the EGRB is thus model dependent and influenced by the adopted size of the Galactic halo, the electron spectrum there, and the spectrum of low-energy background photons which must be determined independently. Recent studies suggest that there are two more diffuse emission components originating nearby in the solar system:  $\gamma$ -ray emission due to inverse Compton scattering of solar photons on cosmic-ray electrons (Moskalenko et al. 2006; Orlando & Strong 2007, 2008) and a  $\gamma$ -ray glow around the ecliptic due to the albedo of small solar system bodies (produced by cosmic-ray interactions) in the Main Asteroid Belt between the orbits of Mars and Jupiter and Kuiper Belt beyond Neptune's orbit (Moskalenko et al. 2008), for more details see §3.2.3.

Extensive work has been done (Sreekumar et al. 1998) to derive the spectrum of the EGRB from EGRET data. Sreekumar et al. (1998) used the relation of modeled Galactic diffuse emission to total measured diffuse emission to determine the EGRB, as the extrapolation to zero Galactic contribution of the total diffuse emission. The derived spectral index  $-2.10 \pm 0.03$  appears to be close to that of  $\gamma$ -ray blazars. Using a different approach, Dixon et al. (1998) concluded that the derived EGRB is affected by a significant contribution from a Galactic halo component. A new detailed model of the Galactic diffuse emission (Strong et al. 2004a) includes an anisotropic Inverse Compton cross section, which brightens the high-latitude IC intensity. This re-analysis (Strong et al. 2004b) gives a new estimate of the EGRB that is lower in flux and steeper than found by Sreekumar et al. (1998) and is not consistent with a power-law.

The sensitivity and resolution of the LAT allow it to resolve many more individual sources, such as AGNs, not resolved by EGRET and that contribute to current estimates of the EGRB. Other components of the remaining EGRB will therefore become more important. Accurate calculations of the "guaranteed background" from conventional sources will make the limits and constraints imposed on exotic processes more reliable.

Estimating point-source contributions to the EGRB requires statistical information about the particular population under consideration, e.g., luminosity function, evolutionary proper-

ties, etc. This analysis has been done for the  $\gamma$ -ray blazar population using a luminosity function derived from EGRET observations to estimate the contribution of unresolved point sources to the EGRB (e.g., Chiang & Mukherjee 1998) as  $>25\%$ . The improved sensitivity of the LAT will reduce the uncertainty of the LAT blazar luminosity function significantly, and at the same time probe the blazar evolution to the redshifts of their expected birth.

This approach will enable LAT observations to place interesting constraints on the cosmological blazar formation rate. So far GeV-photon absorption in the cosmic background radiation field has not been taken into account in any diffuse source background model. With LAT's sensitivity in a much broader energy range as compared to previous pair conversion telescopes, the expected absorption imprints on the diffuse spectrum may provide information on both the source population as well as the background radiation field. With the large number of extragalactic sources resolved by the LAT, the extragalactic component of the diffuse flux will be reduced accordingly; predictions of the reduction due to radio-loud AGN are in the range  $\sim 15\% - 40\%$ .

Fluctuation analysis, where signatures of excess variance are searched for in the surface brightness of the EGRB, is a very general approach to estimating the contribution of any isotropically distributed source population to the diffuse flux. Application of this method to the EGRET data set revealed a point source contribution to the EGRB of 5%–100% (Willis 1996) from analysis on an angular scale of  $3.5^\circ \times 3.5^\circ$ , the scale of the Hunter et al. (1997) Galactic diffuse emission model. With LAT's sensitivity, point spread function and more uniform exposure, smaller spatial scales can be probed, thereby improving the detectability of a signal from contributing point sources to the EGRB.

### 3.2. Understand the mechanisms of particle acceleration in celestial sources

$\gamma$ -ray observations are a direct probe of particle acceleration mechanisms operating in astrophysical systems. Advances with LAT observations in our understanding of these non-thermal processes can be anticipated by reference to discoveries made with EGRET in several important source categories: blazars, pulsars, supernovae remnants, and the Sun.

#### 3.2.1. Blazar AGN jets

With high-confidence detections of more than 60 AGN, almost all of them identified with BL Lacs or Flat Spectrum Radio Quasars (FSRQs) (Hartman et al. 1999), EGRET established blazars as a class of powerful but highly variable  $\gamma$ -ray emitters, in accord with the unified model of AGN as super-massive black holes with accretion disks and jets. Although blazars comprise only several per cent of the overall AGN population, they largely dominate the high-energy extragalactic sky. This is because most of the non-thermal power, which arises from relativistic jets that are narrowly beamed and boosted in the forward direction, is emitted in the  $\gamma$ -ray band (Figure 23), whereas the presumably nearly-isotropic emission from the accretion disk is most luminous at optical, UV, and X-ray energies. Most extragalactic sources detected by the LAT are therefore expected to be blazar AGNs, in contrast with the situation at X-ray frequencies, where most of the detected extragalactic sources are radio-quiet AGN.

The estimated number of blazars that *Fermi*/LAT will detect ranges from a thousand (Dermer 2007) to several thousand (Stecker & Salamon 1996; Chiang & Mukherjee 1998;

Mücke & Pohl 2000: see Figure 24). Such a large and homogeneous sample will greatly improve our understanding of blazars and will be used to perform detailed population studies and to carry out spectral and temporal analyses on a large number of bright objects. In particular, the very good statistics will allow us to a) extend the  $\log N - \log S$  curve to fluxes about 25 times fainter than EGRET, b) estimate the luminosity function and its cosmological evolution, and c) calculate the contribution of blazars and radio galaxies to the extragalactic  $\gamma$ -ray background (see previous section). These observations will chart the evolution and growth of supermassive black holes from high-redshifts to the present epoch, probe a possibly evolutionary connection between BL Lacs and FS-RQs, verify the unified model for radio galaxies and blazars (Urry & Padovani 1995), and test the “blazar sequence” (Fosati et al. 1998). The redshift dependence of spectral parameters of blazars in the LAT energy band, together with the measurements or limits from ground-based TeV instruments, will be used to measure the evolution of the Extragalactic Background Light (see §3.5). Finally, LAT blazar detections will be essential in determining if a truly diffuse component of extragalactic  $\gamma$ -ray emission is required, or if such background can be accounted for by a superposition of various classes of discrete objects.

The LAT’s wide field of view will allow AGN variability to be monitored on a wide range of time scales. Rapid flares as bright as those observed by EGRET from 3C 279 (Kniffen et al. 1993) and by *Swift* and *Agile* from 3C454.3 (Giommi et al. 2006; Vercellone et al. 2008) will be measurable with *Fermi* at  $\gamma$ -ray energies on time scales of hours (e.g., see Figure 22). In addition, the duty cycle of flaring of a large number of blazars will be determined with good accuracy. Measurements of the short variability time scale for luminous  $\gamma$ -ray emission will place lower limits on the Doppler factor of the jet plasma. The values of the Doppler factor can be correlated with  $\gamma$ -ray intensity states for a specific blazar and correlated with membership in different subclasses for many blazars. The Doppler factors can also be compared with values obtained from superluminal motion radio observations in order to infer the location of the  $\gamma$ -ray emission site, with the goal to study the evolution of jet Lorentz factor with distance from the black hole.

Most viable current models of formation and structure of relativistic jets involve conversion of the gravitational energy of matter flowing onto a central supermassive black hole.  $\gamma$ -ray flares are most likely related to the dissipation of magnetic accretion energy or extraction of energy from rotating black holes (e.g., Blandford & Znajek 1977). However, the conversion process itself is not well understood, and many questions remain about the jets, such as: How are they collimated and confined? What is the composition of the jet, both in the initial and in the radiative phase? Where does the conversion between the kinetic power of the jet into radiation take place, and how? What role is played by relativistic hadrons. There are also questions about the role of the magnetic field, such as whether the total kinetic energy of the jet is, at least initially, dominated by Poynting flux.

The first step in answering these questions is to determine the emission mechanisms in order to infer the content of the luminous portions of jets. This understanding should, in turn, shed light on the jet formation process and its connection to the accreting black hole. Determining the emission mechanisms, whether dominated by synchrotron self-Compton, external Compton, or hadronic processes, requires sensitive,

simultaneous multiwavelength observations. Such observations can uncover the causal relationships between the variable emissions in different spectral bands and provide detailed modeling of the time-resolved, broadband spectra. The sensitivity and wide bandpass of the LAT, coupled with well-coordinated multiwavelength campaigns, are essential. Figure 24 shows representative spectral energy distributions of  $\gamma$ -ray blazars and the detection pass-band and sensitivity of the LAT.

Broadband campaigns have been organized to measure the total jet power as compared with accretion power, and the spectra from these observations should reveal whether a single zone structure is sufficient or whether multiple zones are required. Furthermore, the content of the inner part of the jet will be tightly constrained by broadband X-ray spectra and by temporal correlations between the X-ray and  $\gamma$ -ray variability; this is because the radiative energy density in the vicinity of black holes in AGN can be reliably estimated from contemporaneous broadband data, and this circumnuclear radiation must Compton-scatter with all “cold” charged particles contained in the jet (e.g., Sikora & Madejski 2000; Moderski et al. 2004). Finally, the detection of anomalous  $\gamma$ -ray spectral features will indicate the importance of hadronic processes, with significant implications for the origin of ultra-high-energy cosmic rays.

### 3.2.2. Pulsars, pulsar wind nebulae and supernova remnants

Pulsars, with their unique temporal signature, were the only definitively identified EGRET population of Galactic point sources. There were five young radio pulsars detected with high significance, along with the radio-quiet pulsar Geminga and one likely millisecond pulsar (for a summary, see Thompson 2001). A number of other pulsars had lower significance pulse detections and many of the bright, unidentified  $\gamma$ -ray sources are coincident with known radio pulsars. Surrounding young pulsars are bright non-thermal pulsar wind nebulae (PWNe). In the case of the Crab pulsar, EGRET detected a clear signature of PWN emission on off-pulse phases; several other EGRET sources near young pulsars/PWNe show strong variability, possibly connected with variations in the wind shock termination. Even more encouraging has been the success in detecting PWN Compton emission in the TeV band (Aharonian et al. 2005b) from a number of PWNe. Finally, it has long been noticed (Montmerle 1979; Kaaret & Cottam 1996; Yadigaroglu & Romani 1997) that  $\gamma$ -ray sources are spatially correlated with massive star sites, including supernova remnants (SNRs). While EGRET was not able to make definitive associations with SNRs, the LAT has the spatial and spectral resolution to do so.

#### 3.2.2.1 Pulsar magnetospheric emission

Rotation-induced electric fields in charge-depleted regions of pulsar magnetospheres (“gaps”) accelerate charges to ten’s of TeV and produce non-thermal emission across the electromagnetic spectrum. The coherent radio emission, through which most pulsars are discovered, is however a side-show, representing a tiny fraction of the spin-down power. In contrast  $\sim$ GeV peak in the pulsed power can represent as much as 20-30% of the total spin-down. This emission, with its complex pulse profile and phase-varying spectrum, thus gives the key to understanding these important astrophysical accelerators. And, despite 40 years of pulsar studies, many central questions remain unanswered. A basic issue is whether

the high energy emission arises near the surface, close to the classical radio emission (“the polar cap” model, Daugherty & Harding 1996) or at a significant fraction of the light cylinder distance (“outer gap” models, Cheng et al. 1986; Romani 1996). In addition to geometrical (beam-shape) differences, the two scenarios predict that different physics dominates the pair production. Near the surface  $\gamma + B \rightarrow e^+ + e^-$  is important, while in the outer magnetosphere  $\gamma + \gamma \rightarrow e^+ + e^-$  dominates; these result in substantially different predictions for the high energy pulsar spectrum (see Figure 25).

There are a number of pulsar models estimating detailed pulse profiles and spectral variation with pulse phase (for a recent summary, see Harding et al. 2007; Takata et al. 2006). Some also predict emission between the polar cap and outer magnetosphere extremes (Muslimov & Harding 2003; Dyks & Rudak 2003). The improved statistics, energy resolution and high energy sensitivity provided by the LAT enable serious tests of these models for individual bright pulsars. Also, with predicted numbers ranging from dozens to hundreds, the LAT survey of the Galactic pulsar population will provide additional key tests of massive star populations and pulsar evolution.

An extensive campaign of pulsar timing using radio telescopes at Parkes, Jodrell Bank, Nancay, Green Bank, and Arecibo, plus X-ray timing with the Rossi X-ray Timing Explorer has been started in order to provide contemporaneous ephemerides with the  $\gamma$ -ray observations (Smith et al. 2008). As discussed in §3.1.1, LAT’s high sensitivity also allows searches for pulsations in many sources independent of external timing information. Finding a larger population of radio-quiet pulsars is another test of pulsar models (e.g., Gonthier et al. 2007) as well as a new window on the neutron star population of the Galaxy. Indeed, shortly after in-orbit activation, *Fermi*/LAT detected a radio-quiet pulsar in the supernova remnant CTA 1 (Abdo et al. 2008).

### 3.2.2.2 Plerions and unidentified sources

For the Crab pulsar, EGRET detected unpulsed, possibly variable, emission below  $\sim 150$  MeV (likely synchrotron) and Compton-scattered PWN emission at higher energies (de Jager et al. 2006). In this and other pulsars the connection with the IC flux observed in the TeV band is particularly valuable in constraining the PWN B field and the injected particle spectrum. Recent successes with detecting PWN at TeV energies show that the Galactic plane contains an abundance of such sources.

To illustrate the capability of the LAT for advancing PSR/PWN physics, we have simulated one particularly interesting source, the “Kookaburra/Rabbit” complex (Ng et al. 2005). EGRET data suggested that the source was composite and now X-ray (Ng et al. 2005) and TeV (Aharonian et al. 2006a) studies show that the source contains two PWNe. One contains the young energetic radio pulsar PSR J1420-6048, for the other radio pulsations are not known and the source may be Geminga-like. We have simulated, see Figure 26, a plausible PWN spectrum for the two sources (following the HESS morphology) along with a Vela-like pulsed emission for PSR J1420-6048, in the K3 region, and Geminga-like emission for a pulsar in the Rabbit. At high energies the simulation indicates that the two PWNe can be resolved.

### 3.2.2.3 Host supernova remnants

Cosmic rays with energy  $\leq 10^{15}$  eV have long been thought to be shock-accelerated in supernova remnants. For some time, non-thermal X-ray emission has implied a significant population of electrons accelerated to TeV energies (Allen et al. 1997). Moreover, recently the HESS experiment has had great success in detecting TeV emission from Galactic SNR (Aharonian et al. 2005b). However the origin of this emission – inverse Compton scattering from a leptonic component or  $\pi^0$  decay from a hadronic component – is still uncertain. The *Fermi*/LAT has the spatial and spectral sensitivity to resolve this question and thus constrain the origin of cosmic rays. Particularly interesting sources are G0.9+0.1 (Aharonian et al. 2005a) and RX J1713.7-3946 (Aharonian et al. 2006b). In the case of G0.9+0.1, LAT observations will probe the inverse Compton emission mechanism and the interstellar radiation field at the Galactic center (Porter et al. 2006). In case of RX J1713.7-3946, extended TeV emission matches well spatially the lower energy X-ray emission. This match might implicate inverse Compton emission from  $e^+e^-$  populations (Porter et al. 2006) or can be easily accommodated by a  $\pi^0$  model. In the GeV band, well covered by the LAT, the spectra differ (see Figure 27), and can be distinguished. In the particular case of RX J1713.7-3946 and for perhaps a dozen additional objects, careful analysis of LAT observations should be able to resolve the emission at  $E > 10$  GeV – such spatial-spectral studies can further constrain the particle acceleration physics and may isolate shell SNR emission from core PWN emission in composite sources.

### 3.2.3 $\gamma$ -ray emission from the Sun and solar system bodies

The 2005 January 20 solar flare produced one of the most intense, fastest rising, and hardest solar energetic particle events ever observed in space or on the ground.  $\gamma$ -ray measurements of the flare (Share et al. 2006; Grechnev et al. 2008) revealed what appear to be two separate components of particle acceleration at the Sun: i) an impulsive release lasting  $\sim 10$  min with a power-law index of  $\sim 3$  observed in a compact region on the Sun and, ii) an associated release of much higher energy particles having an spectral index  $\leq 2.3$  interacting at the Sun for about two hours. Pion-decay  $\gamma$ -rays appear to dominate the latter component. Such long-duration high-energy events have been observed before, most notably on 1991 June 11 when the EGRET instrument on CGRO observed  $> 50$  MeV emission for over 8 hours (Kanbach et al. 1993). It is possible that these high-energy components are directly related to the particle events observed in space and at Earth.

Solar activity is expected to rise in 2008 with a peak occurring as early as 2011. During normal operations *Fermi* will be able to observe the Sun about 20% of the time with the possibility of increasing that to about 60% during heightened solar activity. With LAT’s large effective area and field-of-view, and its low deadtime it is expected to observe tens of these high-energy events from the Sun. For intense events LAT may be able to localize the source to about  $30''$ , sufficient to determine if it originates from the flare’s X-ray footpoints or from a different location that might be expected if the high-energy particles were accelerated in a shock associated with a coronal mass ejection.

The quiet Sun is also a source of  $\gamma$ -rays which will be detectable by LAT. Estimates of the cosmic-ray proton interactions with the solar atmosphere (solar albedo) were made by Seckel et al. (1991), it is expected that LAT will observe a flux of  $\sim 10^{-7}$  cm $^{-2}$  s $^{-1}$  above 100 MeV from pion decays that

is at the limit of EGRET sensitivity (Thompson et al. 1997b). In addition, a diffuse emission component with maximum in the direction of the Sun due to the inverse Compton scattering of solar photons on cosmic-ray electrons was predicted to be detected by LAT (Moskalenko et al. 2006; Orlando & Strong 2007, 2008). A detailed analysis of the EGRET data (Orlando & Strong 2008) yielded the flux of these two solar components at  $4\sigma$ , consistent with the predicted level. Observations of the inverse Compton scattering of solar photons will allow for continuous monitoring of the cosmic-ray electron spectrum from the close proximity of the solar surface to Saturn’s orbit at 10 AU, important for heliospheric cosmic-ray modulation studies. The fluxes of these components will vary over the solar cycle as solar modulation increases, thus we can expect the highest fluxes to be observed early in the *Fermi* mission.

Recent studies suggest that LAT will be able to see another diffuse emission component originating nearby in the solar system: a  $\gamma$ -ray glow around the ecliptic due to the albedo of small solar system bodies (produced by cosmic-ray interactions) in the Main Asteroid Belt between the orbits of Mars and Jupiter and Kuiper Belt beyond Neptune’s orbit (Moskalenko et al. 2008). Observations of the albedo of small bodies can be used to derive their size distribution. Additionally  $\gamma$ -ray albedo of Kuiper Belt objects could be used to probe the cosmic-ray spectrum in the far outer solar system close to the heliospheric boundary.

Since the ecliptic is projected across the Galactic center, and passes through high Galactic latitudes, both diffuse emission components (inverse Compton scattering of solar photons and the albedo of small solar system bodies) are important to take into account when studying the sources in the direction of the Galactic center and extragalactic diffuse emission (see also §§3.1.2, 3.4).

The Moon is also a source of  $\gamma$ -rays due to CR interactions with its surface and has been detected by EGRET (Thompson et al. 1997b). However, contrary to the CR interaction with the gaseous atmospheres of the Earth and the Sun, the Moon surface is solid, consisting of rock, making its albedo spectrum unique. The spectrum of  $\gamma$ -rays from the Moon is very steep with an effective cutoff around 3–4 GeV (600 MeV for the inner part of the Moon disk) and exhibits a narrow pion-decay line at 67.5 MeV, perhaps unique in astrophysics (Moskalenko & Porter 2007). Apart from other astrophysical sources, the albedo spectrum of the Moon is well understood, including its absolute normalization; this makes it a useful “standard candle” for  $\gamma$ -ray telescopes. The steep albedo spectrum also provides a unique opportunity for energy calibration of  $\gamma$ -ray telescopes such as LAT.

Finally, the brightest  $\gamma$ -ray source on the sky is the Earth’s atmosphere due to its proximity to the spacecraft. The Earth’s albedo due to the cosmic-ray interactions with the atmosphere has been observed by EGRET (Petry 2005). Its observations can provide important information about interactions of cosmic rays and solar wind particles with Earth’s magnetic field and the atmosphere.

### 3.3. Study the high energy behavior of GRBs and transients

Over the last decade the study of X-ray, optical, and radio afterglows of  $\gamma$ -ray bursts (GRBs) has revealed their distance scale, helping to transform the subject from phenomenological speculation to quantitative astrophysical interpretation. We now know that long-duration GRBs ( $\tau > 2$  s) and at least some short-duration GRBs lie at cosmological distances

and that both classes involve extremely powerful, relativistic explosions. Long GRBs are associated with low metallicity hosts with high star formation rates, and have nuclear offsets of  $\sim 10$  kpc (Bloom et al. 2002). Long-duration bursts are typically found in star-forming regions of galaxies and are sometimes associated with supernovae, indicating that the burst mechanism is associated with the collapse of very massive stars (Zhang et al. 2004). Short-duration bursts are often located in much lower star-formation rate regions of the host galaxy, suggesting that in some cases these bursts arise from the coalescence of compact objects (Bloom et al. 2006; Nakar 2007). For the  $\sim 30\%$  of long-duration bursts seen by *Swift* that have measured redshifts, the redshift distribution peaks near  $z \sim 2.8$  (Jakobsson et al. 2006), comparable to Type 2 AGN. The sparse distribution for short bursts with spectroscopic redshifts spans a much lower range,  $z \sim 0.1 - 1.1$ . However, a photometric study of the host galaxies of short bursts without spectroscopically determined redshifts indicates that the fainter hosts tend to lie at redshifts  $z > 1$  (Berger et al. 2007).

The standard picture that has emerged of GRB physics is that an initial fireball powers a collimated, super-relativistic blast wave with initial Lorentz factor  $\sim 10^2 - 10^3$ . Prompt  $\gamma$ -ray and X-ray emission from this “central engine” may continue for few  $\times 10^3$  s. Then external shocks arising from interaction of the ejecta with the circumstellar environment at lower Lorentz factors give rise to afterglows in the X-ray and lower-energy bands that are detected for hours to months. The physical details – primal energy source and energy transport, degree of blast wave collimation, and emission mechanisms – remain for debate (Zhang & Mészáros 2004). The LAT will help constrain many uncertainties in these areas.

EGRET detected two components of high-energy  $\gamma$ -ray emission from GRBs:  $>100$  MeV emission contemporaneous with the prompt pulsed emission detected in the 10–1000 keV band, and a delayed component extending to GeV energies that lasted more than an hour in the case of GRB 940217 (Hurley 1994). Analogous components were detected in the short burst GRB 930131 (Sommer et al. 1994). Most importantly, EGRET detected one burst (GRB 941017) in which a third power-law component was evident above the usual Band function spectrum (Band 1993), with an inferred peak in  $\nu F(\nu)$  above 300 MeV during most of the prompt emission phase (Gonzalez et al. 2003). This indicates that some bursts occur for which the bulk of the energy release falls in the LAT energy band. The prompt pulsed component in these bursts was poorly measured by EGRET since the severe spark chamber deadtime ( $\sim 100$  ms/event) was comparable to or longer than pulse timescales. The LAT is designed with low deadtime ( $\sim 26$   $\mu$ s/event) so that even very intense portions of bursts will be detected with very little ( $< \text{few } \%$ ) deadtime.

The delayed-emission component will also be much better measured because of LAT’s increased effective area, larger FoV, and low self-veto at supra-GeV energies. These observations will test models of delayed GeV emission, for example, those involving production of  $\gamma$ -rays from ultra-high-energy cosmic rays (Böttcher & Dermer 1998), impact of a relativistic wind from the GRB on external matter (Mészáros et al. 1994), and synchrotron self-Compton radiation (Dermer et al. 2000).

Internal and external shock models (Zhang & Mészáros 2004) are currently constrained primarily by spectral and temporal behavior at sub-MeV energies (Fenimore et al. 1999), where the most detailed observations have been made. But

these observations span only a relatively narrow energy range. The LAT's sensitivity will force comparison of models with observations over a dynamic range in energy of  $\sim 10^3 - 10^4$ , and a factor of  $\sim 10^6$  including joint GBM observations.

The LAT can provide time-dependent spectral diagnostics of bright bursts and will be able to measure high-energy exponential spectral cutoffs expected for moderately high redshift GRBs caused by  $\gamma\gamma$  absorption in the cosmic UV-optical background (complementing AGN probes). The LAT will distinguish such attenuation from  $\gamma\gamma$  absorption internal to the sources. Internal absorption is expected to produce time-variable breaks in power-law energy spectra. Signatures of internal absorption will constrain the bulk Lorentz factor and adiabatic/radiative behavior of the GRB blast wave as a function of time for sufficiently bright bursts (Baring & Harding 1997; Lithwick & Sari 2001; Baring 2006).

To estimate the LAT sensitivity to GRB, a phenomenological GRB model is adopted that assumes the spectrum of the GRB is described by the Band function, and the high-energy power law extends up to LAT energies. In order to compare the LAT sensitivity to GRB with the BATSE catalog of GRB, we compute the fluence of GRBs in the 50–300 keV energy band. Figure 28 shows the minimum detectable fluence as a function of the localization accuracy, for different viewing angles and for different high-energy spectral indexes keeping the peak energy and the low energy spectral index of the Band model fixed (to 500 keV and  $-1$ , respectively). The plot shows the expected relation between the fluence and the localization accuracy, which scales as the inverse of the square root of the burst fluence.

Detailed simulations, based on extrapolations from the BATSE-detected GRBs, and adopting the distribution of Band parameters of the catalog of bright BATSE bursts (Kaneko et al. 2006), suggest that the LAT may detect one burst per month, depending on the GRB model for high energy emission. These estimations are in good agreement with the observed number of GRBs. In the first few months of operations LAT has already detected high-energy emission from four GRBs: GRB 080825C (Bouvier et al. 2008, GCN: 8183), the bright GRB 080916C (Tajima et al. 2008, GCN: 8246), GRB 081024B (Omodei et al. 2008, GCN 8407) and GRB 081215A, (McEnery et al. 2008, GCN 8684).

For more than one-third of LAT-detected bursts, LAT localizations should be sufficiently accurate for direct X-ray and optical counterpart searches. For instance,  $\sim 50\%$  of the LAT bursts are projected to have localization errors commensurate with the field of view of *Swift's* XRT ( $23'$ ), which very efficiently detects afterglows with few arc-second error radii. Burst positions are also calculated rapidly onboard, albeit with less initial accuracy, by the LAT flight software, as well as on the ground by the science analysis software pipeline, and distributed via the GCN network. Searches are conducted during ground analysis for fainter bursts not detected by the on-board trigger of the LAT.

Simulations show that LAT observations may constrain quantum gravity scenarios that give rise to an energy-dependent speed of light and consequent energy-dependent shifts of GRB photon arrival times (Amelino-Camelia et al. 1998; Alfaro et al. 2002). Short-duration GRBs, which exhibit negligible pulse spectral evolution above  $\sim 10$  keV may represent the ideal tool for this purpose (Scargle et al. 2008). The LAT properties important for such measurements are its broad energy range, sensitivity at high energies, and  $< 10 \mu\text{s}$  event timing. The LAT's low deadtime and simple event reconstruc-

tion, even for multi-photon events, enable searches for evaporation of primordial black holes with masses of  $\sim 10^{17}$  gm (Fichtel et al. 1994).

### 3.4. Probe the nature of dark matter

Compelling evidence for large amounts of nonbaryonic matter in the Universe is provided by the rotation curves of galaxies, structure-formation arguments, the dynamics and weak lensing of clusters of galaxies, and, most recently, WMAP measurements of the CMB (Spergel et al. 2007, for review see e.g., Bergström 2000). One of the most attractive candidates for Dark Matter is the Weakly Interacting Massive Particle (WIMP). Several theoretical candidates for WIMPs are provided in extensions of the Standard Model of Particle Physics such as Super-Symmetry. Searches for predicted particle states of these theories are one of the prime goals of accelerator-based particle physics, in particular the experiments at the Large Hadron Collider (LHC), which is planned to be operational in 2008.

Annihilations of WIMPs can lead to signals in radio waves, neutrinos, antiprotons and positrons and  $\gamma$ -rays.  $\gamma$ -ray observations have the advantage over charged particles that the direction of the  $\gamma$ -rays points back to the source, and they are not subject to additional flux uncertainties such as unknown trapping times (Bergström et al. 2001; Ullio et al. 2002). However, predicted rates are subject to significant astrophysical uncertainties. Substructure in Dark Matter Halos is especially uncertain, with the predicted flux, for a given annihilation cross section, varying by several orders of magnitude.

Observations of the  $\gamma$ -ray signal of WIMPs may not only constrain the particle nature of these particles but also, in the case that the LHC experiments discover a WIMP candidate, establish the connection between those particles and the Dark Matter. If the Dark Matter is identified, the LAT may be able to image the distribution of Dark Matter in the Galaxy which would constrain scenarios for structure formation.

Two types of WIMP annihilation signals into  $\gamma$ -rays are possible: a spectrally *continuous* flux below  $m_\chi$  the mass of the annihilating particle, resulting mainly from the decay of  $\pi^0$  mesons produced in the fragmentation of annihilation final states, and *monoenergetic*  $\gamma$ -ray lines resulting from WIMP annihilations into two-body final states containing two photons or a Z boson and a photon. Generally, the continuous signal has a much larger rate, but with a signature that is difficult to separate from the other Galactic diffuse foreground contributions, while the monoenergetic line is a much smaller signal, but, if detected, is more easily distinguished. The basic quantities that LAT observations can constrain are the total velocity-averaged annihilation cross section, the branching fraction in different final states, and the mass of the WIMPs.

Different astrophysical sources can be used to search for a signal from WIMP annihilations, each with advantages and challenges. Table 7 summarizes the different search strategies that we have studied.

Detailed calculations of LAT sensitivities to Dark Matter are described in a separate paper (Baltz et al. 2008). Generally, sensitivities are in the cosmologically interesting region of  $\langle\sigma v\rangle \sim 10^{-26} - 10^{-25} \text{ cm}^3 \text{ s}^{-1}$ , in the mass range between 40 and 200 GeV. Figure 29 shows the expected number of halo clumps vs. detection significance for a generic WIMP of mass 100 GeV and  $\langle\sigma v\rangle = 2.3 \times 10^{-26} \text{ cm}^3 \text{ s}^{-1}$  assuming the distribution of halo clumps given by Taylor & Babul (2005a; 2005b) in which about 30% of the halo mass is concentrated

in halo clumps. The diffuse background was assumed to consist of an isotropic extragalactic component (Sreekumar et al. 1998) and a Galactic component (Strong et al. 2000).

The intensity needed to detect a  $\gamma$ -ray line with  $5\sigma$  significance is in the vicinity of  $10^{-9}$  ph cm $^{-2}$  s $^{-2}$  sr $^{-1}$  for an annulus around the Galactic Center (masking the galactic plane to  $\pm 15^\circ$ ).

In Baltz et al. (2006), information obtainable with *Fermi* is compared with what may be learned at upcoming accelerator-based experiments, for a range of particle Dark Matter models. Over sizable ranges of particle model parameter space, *Fermi* has significant sensitivity and will provide key pieces of the puzzle. The challenge will be to untangle the annihilation signals from the astrophysical backgrounds due to other processes.

### 3.5. Use high-energy $\gamma$ -rays to probe the early universe

Photons above 10 GeV can probe the era of galaxy formation through absorption by near UV, optical, and near IR extragalactic background light (EBL). The EBL at IR to UV wavelengths is accumulated radiation from structure and star formation and its subsequent evolution in the universe with the main contributors being the starlight in the optical to UV band, and IR radiation from dust reprocessed starlight (see e.g., Madau & Phinney 1996; MacMinn & Primack 1996; Primack et al. 2001; Hauser & Dwek 2001).

Since direct measurements of EBL suffer from large systematic uncertainties due to contamination by the bright foreground (e.g., interplanetary dust, stars and gas in the Milky Way, etc.), the indirect probe provided by absorption of high-energy  $\gamma$ -rays via pair production ( $\gamma + \gamma \rightarrow e^+ + e^-$ ), emitted from blazars, during their propagation in the EBL fields, can be a powerful tool for probing the EBL density. For example, observations of relatively nearby TeV blazars by the HESS atmospheric Cherenkov telescope (Aharonian et al. 2006c) have placed significant limits on the EBL at IR energies in the local universe. The photon-photon pair production cross section has a pronounced maximum at  $E_\gamma \approx 0.8$  TeV (1 eV/EBL) (interaction angle averaged), close to the pair production threshold. Hence the LAT energy range extending to greater than 300 GeV is ideal for probing the EBL in the largely unexplored optical-UV band. According to current EBL models (e.g., Primack et al. 1999; Stecker et al. 2006; Kneiske et al. 2004), absorption breaks in the LAT energy range are expected for sources located at  $z \geq 0.5$ . This offers for the first time the opportunity to constrain the *evolution* of the EBL. For this purpose, at least two methods have been developed: probing the horizon of extragalactic  $\gamma$ -rays through measurements of either the ratio of absorbed to unabsorbed flux versus redshift (Chen et al. 2004), or detection of the e-folding cutoff energy  $E(\tau_{\gamma\gamma} = 1)$  as a function of redshift (Fazio & Stecker 1970; Kneiske et al. 2004) in a large number of suitable sources. With the expected LAT flux sensitivity

the number of detected  $\gamma$ -ray loud blazars will increase to potentially several thousand sources (see §3.2.1) with redshifts up to  $z \sim 5 - 6$ . Such a large number of sources will be required for a statistically meaningful search for evolutionary behavior of spectral absorption features in bright and hard-spectrum AGNs. Any of the analysis methods employed requires disentangling source intrinsic opacity effects, particularly if they are evolutionary with redshift, from the absorption due to EBL. Absorption in the local environment of AGN but external to the jet radiation fields has been shown to mimic an absorption pattern similar to what is expected from EBL attenuation of  $\gamma$ -rays (Reimer 2007), i.e. higher  $\gamma$ -ray opacities from higher redshift sources. Careful source selection and a statistical assessment of the radiation field density at the  $\gamma$ -ray source site will be an integral part of the analysis. Monitoring of external photon fields in AGN (e.g., broad-line region lines) and correlating with the observed  $\gamma$ -ray cutoff energy may offer verification, and possibly quantification, of this effect.

## 4. SUMMARY

The Large Area Telescope, the primary instrument on the *Fermi* Gamma-ray Space Telescope, is a state-of-the-art, high-energy  $\gamma$ -ray telescope. The LAT's combination of wide field-of-view, large effective area, excellent single photon angular resolution (particularly at high energies), good energy resolution, excellent time resolution and low instrumental dead time, will push back several frontiers in high-energy astrophysics. Data from the LAT and software analysis tools will be available to the entire scientific community.

The *Fermi*/LAT Collaboration acknowledges the generous ongoing support of a number of agencies and institutes that have supported both the development and the operation of the LAT as well as scientific data analysis. These include the National Aeronautics and Space Administration and the Department of Energy in the United States, the Commissariat à l'Énergie Atomique and the Centre National de la Recherche Scientifique / Institut National de Physique Nucléaire et de Physique des Particules in France, the Agenzia Spaziale Italiana and the Istituto Nazionale di Fisica Nucleare in Italy, the Ministry of Education, Culture, Sports, Science and Technology (MEXT), High Energy Accelerator Research Organization (KEK) and Japan Aerospace Exploration Agency (JAXA) in Japan, and the K. A. Wallenberg Foundation, the Swedish Research Council, and the Swedish National Space Board in Sweden. Additional support from the following agencies is also gratefully acknowledged: the Istituto Nazionale di Astrofisica in Italy and the K. A. Wallenberg Foundation for providing a grant in support of a Royal Swedish Academy of Sciences Research fellowship for JC.

## REFERENCES

- Abdo, A., et al. 2008, *Science*, 322, 1218  
 Agostinelli, S., et al. 2003, *Nucl. Instr. Meth. A*, 506, 250  
 Aguilar, M., et al. 2002, *Phys. Rep.*, 366, 331  
 Aharonian, F. A., et al. 2005a, *A&A*, 432, L25  
 Aharonian, F. A., et al. 2005b, *A&A*, 437, L7  
 Aharonian, F. A., et al. 2006a, *A&A*, 456, 245  
 Aharonian, F. A., et al. 2006b, *A&A*, 449, 223  
 Aharonian, F. A., et al. 2006c, *Nature*, 440, 1018  
 Albert, J., et al. 2007, *ApJ*, 665, L51  
 Alfaro, J., Morales-Tecotl, H. A., & Urrutia, L. F. 2002, *Phys. Rev. D*, 65, 103509  
 Allen, G. E., et al. 1997, *ApJ*, 487, L97  
 Allison, J., et al. 2006, *IEEE Trans. Nuc. Sci.*, 53, 270  
 Amelino-Camelia, G., Ellis, J., Mavromatos, N.E., Nanopoulos, D.V., & Sarkar, S. 1998, *Nature*, 395, 525  
 Atwood, W. B., et al. 1994, *Nucl. Instr. Meth. A*, 342, 302  
 Atwood, W. B., et al. 2000, *Nucl. Instr. Meth. A*, 446, 444  
 Atwood, W. B., Ziegler, M., Johnson, R. P., & Baughman, B. M. 2006, *ApJ*, 652, L49

- Atwood, W. B., et al. 2007, *Aph*, 28, 422
- Baldini, L., et al. 2006, *IEEE Trans. Nuc. Sci.*, 53, 466
- Baldini, L., et al. 2007, in *Proc. of 1<sup>st</sup> GLAST Symposium*, eds. S. Ritz, P. Michelson, & C. Meegan, (NY: AIP), AIP Conf. Proc. 921, 190
- Baltz, E. A., Battaglia, M., Peskin, M. E., & Wizansky, T. 2006, *Phys. Rev. D*, 74, 103251
- Baltz, E. A., et al. 2008, *JCAP*, 07, 013
- Band, D., et al. 1993, *ApJ*, 413, 281
- Baring, M. G., & Harding, A. K. 1997, *ApJ*, 491, 663
- Baring, M. G. 2006, *ApJ*, 650, 1004
- Barrand, G., et al. 2001, *Computer Phys. Comm.*, 140, 45
- Baughman, B. M., Atwood, W. B., Johnson, R. P., Porter, T. A., & Ziegler M., 2007, in *Proc. 30th Int. Cosmic Ray Conf.*, in press (arXiv:0706.0503)
- Berezinsky, V. S., Blasi, P., & Ptuskin, V. S. 1997, *ApJ*, 487, 529
- Berezinsky, V., Hnatyk, B., & Vilenkin, V. 2001, *Phys. Rev. D*, 64, 043004
- Berger, E., et al. 2007, *ApJ*, 660, 496
- Bergström, L. 2000, *Rept. Prog. Phys.*, 63, 793
- Bergström, L., Edsjö, J., & Ullio, P. 2001, *Phys. Rev. Lett.*, 87, 251301
- Bidoli, V., et al. 2002, *Annales Geophysicae*, 20, 1693
- Biggami, G. F. et al. 1975, *Space Sci. Instr.*, 1, 245
- Biggami, G. F., Fichtel, C. E., Hartman, R. C., & Thompson D. J. 1979, *ApJ*, 323, 649
- Biggami, G. F., & Caraveo, P. A. 1996, *ARA&A*, 34,331
- Blandford, R. D., & Znajek, R. L. 1977, *MNRAS*, 179, 433
- Bloom, J. S., Kulkarni, S. R., & Djorgovski, S. G. 2002, *AJ*, 123, 1111
- Bloom, J. S., et al. 2006, *ApJ*, 638, 354
- Böttcher, M., & Dermer, C. D. 1998, *ApJ*, 499, L131
- Bouvier, A., et al. 2008, *GCN Circular* 8183
- Breiman, L., Friedman, J., Stone, C. J., & Olshen, R. A. 1984, *Classification and Regression Trees*, Wadsworth International Group, Belmont, CA
- Calcáneo-Roldán, C., & Moore, B. 2000, *Phys. Rev. D*, 62, 123005
- Caraveo, P. A., Biggami, G. F., & Trümper, J., 1996, *A&A Rev.*, 7, 209
- Caraveo, P. A., & Reimer, O. 2007, in *Proc. of 1st GLAST Symposium*, eds. S. Ritz, P. Michelson & C. Meegan, (NY:AIP), AIP Conf. Proc. 921, 289
- Carlson, P., et al. 1996, *Nucl. Instr. Meth. A*, 376, 271
- Casanova, S., Dingus, B. L., & Zhang, B. 2007, *ApJ*, 656, 306
- Chandler, A. M., et al. 2001 *ApJ*, 556, 59
- Chen, A., Reyes, L. C., & Ritz, S. 2004, *ApJ*608, 686
- Cheng, K. S., Ho, C., & Ruderman, M. 1986, *ApJ*, 300, 500
- Chiang, J., & Mukherjee, R. 1998, *ApJ*, 496, 752
- Colafrancesco, S., 2002, *A&A*, 396, 31
- Colafrancesco, S., & Blasi, P. 1998, *Aph*, 9, 227
- Couto é Silva, E. do, et al. 2001, *Nucl. Instr. Meth. A*, 474, 19
- Dar, A., & Shaviv, N. 1995, *Phys. Rev. Lett.*, 75, 3052
- Daugherty, J. K., & Harding, A. K. 1996, *ApJ*, 458, 278
- de Boer, W., et al. 2005, *Phys. Rev. Lett.*, 95, 209001
- de Jager, O. C., et al. 2006, *A&AS*, 120, 441
- Dermer, C. D., Chiang, J., & Mitman, K. E. 2000, *ApJ*, 537, 785
- Dermer, C. D. 2007, *ApJ*, 659, 958
- Dixon, D. D., Hartmann, D. H., Kolaczyk, E. D., Samimi, J., Diehl, R., Kanbach, G., Mayer-Hasselwander, H., & Strong, A. W. 1998, *New Astron.*, 3, 539
- Dolgov, A., & Silk, J. 1993, *Phys. Rev. D*, 47, 4244
- Dyks, J., & Rudak, B. 2003, *ApJ*, 598, 1201
- Elsässer, D., & Mannheim, K. 2005, *Phys. Rev. Lett.*, 94, 171302
- Engelmann, J. J., et al. 1990, *A&A*, 233, 96
- Ensslin, T. A., Biermann, P. L., Kronberg, P. P., & Wu, X.-P., 1997, *ApJ*, 477, 560
- Espósito, J. A., et al. 1996, *ApJ*, 461, 820
- Fazio, G. G., & Stecker, F. W. 1970, *Nature*, 226, 135
- Fenimore, E. E., Ramirez-Ruiz, E., & Wu, B. 1999, *ApJ*, 518, 73
- Feretti, L., Burigana, C., & Ensslin, T. 2004, *New Astron.*, 48, 1134
- Ferreira, O., et al. 2004, *Nucl. Instr. Meth. Phys. Res. A*, 530, 323
- Fichtel, C. E., et al. 1975, *ApJ*, 198, 163
- Fichtel, C. E., et al. 1994, *ApJ*, 434, 557
- Fossati G., et al. 1998, *MNRAS*, 299, 433
- Frühwirth, R., Regler, M., Bock, R. K., Grote, H. & Notz, D. 2000, *Data Analysis Techniques for High-Energy Physics*, 2nd edition, Cambridge University Press
- Fryer, C. L., & Heger, A. 2005, *ApJ*, 623, 302
- Funk, S., et al. 2008, *ApJ*, 679, 1299
- Gabici, S., & Blasi, P. 2003, *Aph*, 19, 679
- Gao, Y.-T., Stecker, F. W., Gleiser, M., & Cline, D. B. 1990, *ApJ*, 361, 37
- Gehrels, N., et al. 2000, *Nature*, 404, 363
- Giommi, P., et al. 2006, *A&A*, 456, 911
- Giovannini, G., Tordi, M., & Feretti, L. 1999, *New Astron.*, 4, 141
- Gonthier, P. L., et al. 2007, *Ap&SS*, 309, 245
- Gonzalez, M. M., et al. 2003, *Nature*, 424, 74
- Grechnev, V. V. 2008, *Sol. Phys.*, 252, 149
- Grenier, I. A. 2000, *A&A*, 364, L93
- Grenier, I. A., Casandjian, J.-M., & Terrier, R. 2005, *Science*, 307, 1292
- Grove, E., et al. 2008, in preparation
- Haino, S., et al. 2004, *Phys. Lett. B*, 594, 35
- Halpern, J. P., et al. 2001, *ApJ*, 552, L125
- Halpern, J. P., et al. 2002, *ApJ*, 573, L41
- Harding, A. K., Grenier, I. A., & Gonthier, P. L. 2007, *Ap&SS*, 309, 221
- Hartman, R. C., et al. 1999, *ApJS*, 123, 79
- Hauser, M. G., & Dwek, E. 2001, *ARA&A*, 39, 249
- Hawking, S. W., 1974, *Nature*, 248, 30
- Hunter, S. D., et al. 1997, *ApJ*, 481, 205
- Hurley, K. 1994, *Nature*, 372, 652
- Jackson, B., et al. 2005, *IEEE Signal Processing Letters*, 12, 105
- Jakobsson, P., et al. 2006, *A&A*, 447, 897
- Johnson, W. N., et al. 2001, *IEEE Trans. Nuc. Sci.*, 48, 1182
- Jungman, G., Kamionkowski, M., & Griest, K. 1996, *Phys. Rev. D*, 267, 195
- Kaaret, P., & Cottam, J. 1996, *ApJ*, 462, L35
- Kaneko, Y., et al. 2006, *ApJS*, 166, 298
- Kanbach, G., et al. 1993, *A&AS*, 97, 349
- Keshet, U., et al. 2003, *ApJ*, 585, 128
- Kneiske, T. et al. 2004, *A&A*, 413, 807
- Kniffen, D. A., et al. 1993, *ApJ*, 411, 133
- Kramer, M., et al. 2003, *MNRAS*, 342, 1299
- Lake, G. 1990, *Nature*, 346, 39
- Lithwick, Y., & Sari, R. 2001, *ApJ*, 555, 540
- Loeb, A., & Waxman, E. 2000, *Nature*, 405, 156
- MacMinn, D., & Primack, J. R. 1996, *Space Sci. Rev.*, 75, 413
- Madau, P., & Phinney, E. S. 1996, *ApJ*, 456, 124
- Maki, K., Mitsui, T., & Orito, S. 1996, *Phys. Rev. Lett.*, 76, 3474
- Mattox, J., et al. 1996, *A&AS*, 120, 95
- Mattox, J., Hartman, R. C., & Reimer, O. 2001, *ApJS*, 135, 155
- Mészáros, P., Rees, M. J., & Papanthanasian, H. 2004, *ApJ*, 432, 181
- McEnery, J., et al. 2008, *GCN Circular* 8407
- Mikhailov, V., et al. 2002, *J. Mod. Phys. A*, 17, 1695
- Miniati, F. 2002, *MNRAS*, 337, 199
- Mirabal, N., & Halpern, J. P. 2001, *ApJ*, 547, L137
- Mizuno, T., et al. 2004, *ApJ*, 614, 1113
- Moderski, R., et al. 2004, *ApJ*, 611, 77
- Moiseev, A. A., et al. 2004, *Aph*, 22, 275
- Moiseev, A. A., et al. 2007, *Aph*, 27, 339
- Montmerle, T. 1979, *ApJ*, 231, 95
- Moskalenko, I. V., & Strong, A. W. 2000, *ApJ*, 528, 357
- Moskalenko, I. V., & Strong, A. W. 2005, in *Proc. Int. Conf. on Astrophysical Sources of High Energy Particles and Radiation*, eds. T. Bulik, et al. (NY: AIP), AIP Conf. Proc. 801, 57
- Moskalenko, I. V., Porter, T. A., & Digel, S. W. 2006, *ApJ*, 652, L65
- Moskalenko, I. V., & Porter, T. A. 2007, *ApJ*, 670, 1467
- Moskalenko, I. V., Digel, S. W., Porter, T. A., Reimer, O., & Strong A. W. 2007, *Nucl. Phys. B (Proc. Suppl.)*, 173, 44
- Moskalenko, I. V., Porter, T. A., Digel, S. W., Michelson, P. F., & Ormes, J. F. 2007, *ApJ*, 681, 1708
- Mücke, A., & Pohl, M. 2000, *MNRAS*, 312, 177
- Mukherjee, R., & Chiang, J. 1999, *Aph*, 11, 213
- Muslimov, A., & Harding, A. K. 2003, *ApJ*, 588, 430
- Nakar, E. 2007, *Phys. Rep.*, 442, 166
- Narumoto T., & Totani, T. 2006, *ApJ*, 643, 81
- Ng, C.-Y., Roberts, M. S. E., & Romani, R. W. 2005, *ApJ*, 627, 904
- Nolan, P. L., et al. 2003, *ApJ*, 597, 615
- Norris, J. P., et al. 1996, *ApJ*, 459, 393
- Omodei, N., et al. 2008, *GCN Circular* 8407
- Orlando, E., & Strong, A. W. 2007, *Ap&SS*, 309, 359
- Orlando, E., & Strong, A. W. 2008, *A&A*, 480, 847
- Page, D. N., & Hawking, S. W. 1976, *ApJ*, 206, 1
- Paredes, J. M., Martí, J., Ribó, M., & Massi, M. 2000, *Science*, 288, 2340
- Pavlidou, V., & Fields, B. D. 2001, *ApJ*, 558, 63
- Pavlidou, V., & Fields, B. D. 2002, *ApJ*, 575, L5
- Picozza, P., et al. 2007, *Aph*, 27, 296
- Petry, D. 2005, in *High Energy Gamma Ray Astronomy: 2nd International Symposium*, Heidelberg, July, 2004, eds. F. A. Aharonian, H. J. Volk, & D. Horns, (NY:AIP), AIP Conf. Proc. 745, 709
- Porciani, C., & Madau, P. 1999, *ApJ*, 526, L522
- Porter, T. A., Moskalenko, I. V., & Strong A. W. 2006, *ApJ*, 648, L29
- Porter, T. A., Moskalenko, I. V., Strong A. W., Orlando, E., & Bouchet, L. 2008, *ApJ*, 682, 400
- Preece, R. D., et al. 2000, *ApJS*, 126, 19
- Primack, J. R., Bullock, J. S., Somerville, R. S. & MacMinn, D. 1999, *Aph*, 11, 93

- Primack, J. R., Somerville, R. S., Bullock, J. S. & Devriendt, J. E. G. 2001, AIP, 558, 463
- Primack, J. R., Bullock, J. S., & Somerville, R. S. 2005, in Proc. of the Gamma 2004 Symposium on High Energy Gamma Ray Astronomy (NY:AIP), AIP Conf. Proc. 745, 23
- Reimer, A. 2007, ApJ, 665, 1023
- Reimer, O., et al. 2001, MNRAS, 324, 772
- Reimer, O., Pohl, M., Sreekumar, P., & Mattox, J. R. 2003, ApJ, 558, 155
- Rephaeli, Y., Nevalainen, J., Ohashi, T., & Bykov, A. M. 2008, Space Sci. Rev., 134, 71
- Roberts, M. S. E., Romani, R. W., & Kawai, N. 2001, ApJS, 133, 451
- Romani, R. W. 1996, ApJ, 470, 469
- Romero, G. E., et al. 1999, A&A, 348, 868R
- Rudaz, S., & Stecker, F. W. 1991, ApJ368, 406
- Scargle, J. D. 1998, ApJ, 504, 405
- Scargle, J. D., Norris, J. P., & Bonnell, J. T. 2008, ApJ, 673, 972
- Seckel, D., Stanev, T., & Gaisser, T. K. 1991, ApJ, 382, 652
- Selesnik, R. S.,Looper, M. D., & Mewaldt, R. A. 2007, Space Weather, 5, S04003
- Share, G.H., et al. 2006, BAAS, 38, 255
- Sikora, M., & Madejski, G. 2000, ApJ, 534, 109
- Silk, J., & Srednicki, M., 1984, Phys. Rev. Lett., 53, 624
- Smith, D. A., et al. 2008, A&A, to be published
- Sommer, M., et al. 1994, ApJ, 422, L63
- Sowards-Emmerd, D., Romani, R. W., & Michelson, P. F. 2003, ApJ, 590, 109
- Sowards-Emmerd, D., et al. 2004, ApJ, 609, 564
- Sowards-Emmerd, D., et al. 2005, ApJ, 626, 95
- Spergel, D. N., et al. 2007, ApJS, 170, 377
- Sreekumar, P., et al. 1998, ApJ, 494, 523
- Stecker, F. W., Vette, J. I., & Trombka, J. I. 1971, Nature, 231, 122
- Stecker, F., & Salamon, M. 1996, ApJ, 464, 600
- Stecker, F. W., Malkan, A., & Scully, S. T. 2006, ApJ, 648, 774; and erratum: ApJ, 658, 1392 (2007)
- Stecker, F., Hunter, S. D., & Kniffen, D. A. 2008, APh, 29, 25
- Strong, A. W., Moskalenko, I. V., & Reimer, O. 2000, ApJ, 537, 763
- Strong, A. W., Moskalenko, I. V., & Reimer, O. 2004a, ApJ, 613, 962
- Strong, A. W., Moskalenko, I. V., & Reimer, O. 2004b, ApJ, 613, 956
- Strong, A. W., Moskalenko, I. V., Reimer O., Digel S., & Diehl R. 2004c, A&A, 422, L47
- Sturmer, S. J., & Dermer, C. D. 1995, A&A, 291, L17
- Tajima, H., et al. 2008, GCN Circular 8246
- Takata, J., et al. 2006, MNRAS, 366, 1310
- Tavani, M., et al. 1998, ApJ, 497, L89
- Tavani, M., et al. 2008, Nucl. Instr. Meth. Phys. Res. A, 588, 52
- Taylor, J. E., & Babul, A. 2005a, MNRAS, 364, 515
- Taylor, J. E., & Babul, A. 2005b, MNRAS, 364, 535
- Thompson, D. J., et al. 1993, ApJS, 86, 629
- Thompson, D. J., et al. 1997a, Proc. 4th Compton Symp., ed. C.D. Dermer, et al. (New York, AIP), pp.39-51
- Thompson, D. J., Bertsch, D. L., Morris, D. J., & Mukherjee, R. 1997b, J. Geophys. Res., 102, 14735
- Thompson, D. J., et al. 2002, IEEE Trans. Nuc. Sci., 49, 1898
- Thompson, D. J. 2001, Proc. of High-Energy Gamma-ray Astronomy Symposium, eds. F.A. Aharonian & H.J. Völk (New York, AIP), AIP Conf. Proc., 558, 103
- Thompson, D. J. 2004, in Cosmic Gamma-Ray Sources, eds. K. S. Cheng, & G. E. Romero (Dordrecht Boston London: Kluwer), 149
- Torres, D. F., et al. 2004, ApJ, 607, L99
- Torres, D. F., & Reimer, O. 2005, ApJ, 629, L141
- Totani, T., & Kitayama, T. 2000, ApJ, 545, 572
- Ullio, P., et al. 2002, Phys. Rev. D, 66, 123502
- Urry, M., & Padovani, P. 1995, PASP, 107, 803
- Vercellone, S., et al. 2008, ApJ, 676, L13
- Voronov, S. A., et al. 1991, Cosmic Research (English Translation) 29(4), 567
- Willis, T. D. 1996, PhD thesis, Stanford University
- Yadigaroglu, I. A., & Romani, R. W. 1997, ApJ, 476, 347
- Zhang, B., & Mészáros, P. 2004, Intl. J. Mod. Phys. A, 19, 238
- Zhang, W., Woosley, S. E., & Heger, A. 2004, ApJ, 608, 365
- Ziegler, M., Baughman, B. M., Johnson, R. P., & Atwood, W. B. 2008, ApJ, 680, 620
- Zuccon, P., et al. 2003, APh, 20, 221

TABLE 1. SUMMARY OF LARGE AREA TELESCOPE INSTRUMENT PARAMETERS AND ESTIMATED PERFORMANCE

Parameter	Value or Range
Energy range	20 MeV – 300 GeV
Effective area at normal incidence <sup>a</sup>	9,500 cm <sup>2</sup>
Energy resolution (equivalent Gaussian 1 $\sigma$ ):	
100 MeV – 1 GeV (on axis)	9%–15%
1 GeV – 10 GeV (on axis)	8%–9%
10 GeV – 300 GeV (on-axis)	8.5%–18%
>10 GeV (>60° incidence)	≤6%
Single photon angular resolution (space angle)	
on-axis, 68% containment radius:	
>10 GeV	≤0.15°
1 GeV	0.6°
100 MeV	3.5°
on-axis, 95% containment radius	< 3 × $\theta_{68\%}$
off-axis containment radius at 55°	< 1.7 × on-axis value
Field of View (FoV)	2.4 sr
Timing accuracy	< 10 $\mu$ sec
Event readout time (dead time)	26.5 $\mu$ sec
GRB location accuracy on-board <sup>b</sup>	< 10'
GRB notification time to spacecraft <sup>c</sup>	< 5 sec
Point source location determination <sup>d</sup>	< 0.5'
Point source sensitivity (>100 MeV) <sup>e</sup>	3 × 10 <sup>-9</sup> ph cm <sup>-2</sup> s <sup>-1</sup>

<sup>a</sup>Maximum (as function of energy) effective area at normal incidence. Includes inefficiencies necessary to achieve required background rejection. Effective area peak is typically in the 1 to 10 GeV range.

<sup>b</sup>For burst (<20 sec duration) with >100 photons above 1 GeV. This corresponds to a burst of  $\sim 5$  cm<sup>-2</sup> s<sup>-1</sup> peak rate in the 50 – 300 keV band assuming a spectrum of broken power law at 200 keV from photon index of -0.9 to -2.0. Such bursts are estimated to occur in the LAT FoV  $\sim 10$  times per year.

<sup>c</sup>Time relative to detection of GRB.

<sup>d</sup>High latitude source of 10<sup>-7</sup> cm<sup>-2</sup> s<sup>-1</sup> flux at >100 MeV with a photon spectral index of -2.0 above a flat background and assuming no spectral cut-off at high energy; 1 $\sigma$  radius; 1-year survey.

<sup>e</sup>For a steady source after 1 year sky survey, assuming a high-latitude diffuse flux of 1.5 × 10<sup>-5</sup> cm<sup>-2</sup> s<sup>-1</sup> sr<sup>-1</sup> (>100 MeV) and a photon spectral index of -2.1, with no spectral cut-off.

TABLE 2. KEY LAT TRACKER PARAMETERS

Parameter	Value	Performance Drivers and Constraints
Noise occupancy (fraction of channels with noise hits per trigger)	10 <sup>-6</sup>	Trigger rate, data volume, track reconstruction. The requirement, driven by the trigger rate, is < 10 <sup>-4</sup>
Single channel efficiency for minimum ionizing particle (MIP), within fiducial volume	>99%	PSF, especially at low energy. It is important to measure the tracks in the first 2 planes following the conversion point.
Ratio of strip pitch to vertical spacing between tracker planes	0.0071	High-energy (>1 GeV) PSF
Silicon-strip detector pitch (center-to-center distance between strips)	228 $\mu$ m	Small value needed to maintain a small pitch-to-plane-spacing ratio without destroying the FoV.
Aspect ratio (height/width)	0.4	Large FoV for photons with energy determination
Front converter foil thickness in radiation lengths (100% W)	12 × 0.03 (0.010 cm/foil)	Minimize thickness per plane for low-energy PSF, but not so much that support material dominates. Maximize total thickness to maximize effective area.
Back converter foil thickness in radiation lengths (93% W)	4 × 0.18 (0.072 cm/foil)	Effective area and FoV at high energies
Support material and detector material per $x - y$ plane (radiation lengths)	0.014	Stable mechanical support is needed, but much of this material is in a non-optimal location for the PSF. Minimize to limit PSF tails from conversions occurring in support material.

TABLE 3. KEY LAT CALORIMETER PARAMETERS

Parameter	Value	Performance Drivers and Constraints
Depth, including tracker (radiation lengths)	10.1	Calorimeter depth is a compromise in shower containment against maximum permitted mass. Use segmentation and shower profile analysis to improve energy measurement at high energies
Sampling (angle dependent)	>90% active	Energy loss in passive material causes low-energy tails on measured energy and affects energy resolution.
Longitudinal segmentation	8 segments	Showers profile analysis permits estimation of and correction for energy leakage
Lateral segmentation	~1 Molière radius	Correlation of energy deposition in calorimeter with extrapolated tracks in tracker is critical part of background rejection.

TABLE 4. KEY LAT ANTICOINCIDENCE DETECTOR PARAMETERS

Parameter	Value	Performance Drivers and Constraints
Segmentation into tiles	<1000 cm <sup>2</sup> each	Minimize self-veto, especially at high energy. This value is for the top. Side tiles are smaller, to achieve a similar solid angle, as seen from the calorimeter.
Efficiency of a tile for detecting a MIP	>0.9997	Cosmic ray rejection, to meet a requirement of 0.99999 when combined with the other subsystems.
Number of layers	1	Minimize material, mass, and power. Dual readout on each tile for redundancy.
Micrometeoroid / thermal blanket thickness	0.39 g cm <sup>-2</sup>	Small value needed to minimize $\gamma$ -ray production in this passive material from cosmic-ray interactions.
Total thickness (radiation lengths)	10.0 mm (0.06)	Minimize absorption of incoming gamma radiation

TABLE 5. DATA SOURCES FOR BACKGROUND MODEL

	Energy range		
	> local geomagnetic cutoff	150 MeV to geomagnetic cutoff	10 MeV – 150 MeV
Galactic Cosmic Rays			
protons + antiprotons	AMS		
electrons	AMS		
positrons	AMS		
He	AMS		
$Z > 2$ nuclei	HEAO-3		
Splash Albedo			
protons		AMS	Nina
electrons		AMS	Mariya
positrons		AMS	Mariya
Re-entrant Albedo			
protons			Nina
electrons			Mariya
positrons			Mariya
Earth albedo $\gamma$ -rays		10 MeV – 100 GeV, EGRET	
Neutrons		10 MeV – 1 TeV, various sources	

NOTE. — Data Sources: AMS: Aguilar et al. (2002); Nina: Bidoli et al. (2002); Mariya: Voronov et al. (1991), Mikhailov et al. (2002); EGRET: Petry (2005); HEAO-3: Engelmann et al. (1990); neutrons: Selesnik et al. (2007)

TABLE 6. LAT ANALYSIS CLASSES

Analysis class	Residual background rate (Hz)	Characteristics
Transient	2	Maximize effective area, particularly at low energy, at the expense of higher residual background rate; suitable for study of localized, transient sources
Source	0.4	Residual background rate comparable to extragalactic diffuse rate estimated from EGRET; suitable for study of localized sources
Diffuse	0.1	Residual background rate comparable to irreducible limit and tails of PSF at high-energy minimized; suitable for study of the weakest diffuse sources expected

TABLE 7. LAT SEARCHES FOR DARK MATTER

Astrophysical source or search technique	Advantages	Disadvantages
Galactic center	Large number of photons	Disturbance by many point sources, uncertainty in diffuse background prediction.
Satellites, sub-halos	Low celestial diffuse background, good identification of source	Low number of photons.
Milky way halo	Large number of photons	Uncertainty in Galactic diffuse background prediction
Extragalactic	Large number of photons	Astrophysical uncertainties, uncertainty in Galactic diffuse contribution.
Spectral lines	No astrophysical uncertainties, smoking gun signal	Very low number of photons.

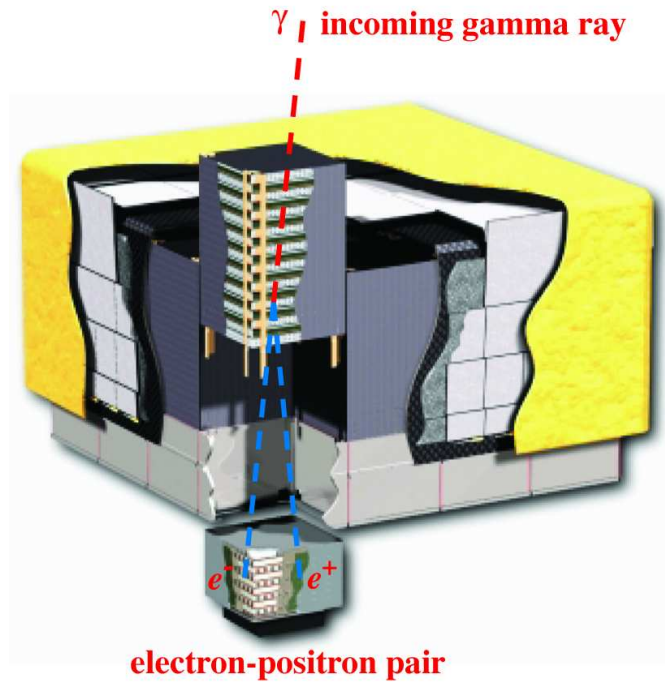


FIG. 1.— Schematic diagram of the Large Area Telescope. The telescope's dimensions are  $1.8 \text{ m} \times 1.8 \text{ m} \times 0.72 \text{ m}$ . The power required and the mass are 650 W and 2,789 kg, respectively.

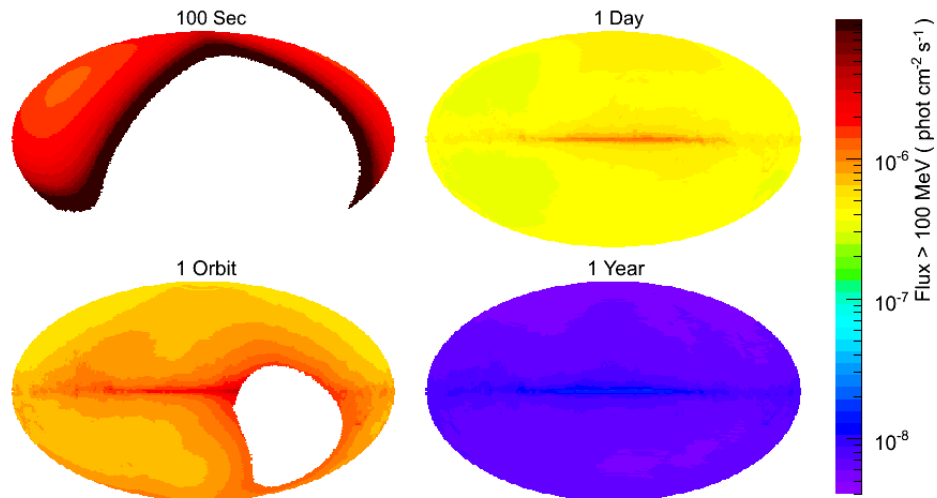


FIG. 2.— LAT source sensitivity for exposures on various timescales. Each map is an Aitoff projection in galactic coordinates. In standard sky-survey mode, nearly uniform exposure is achieved every 2 orbits, with every region viewed for  $\sim 30$  min every 3 hours.



FIG. 3.— Completed tracker array before integration with the ACD.

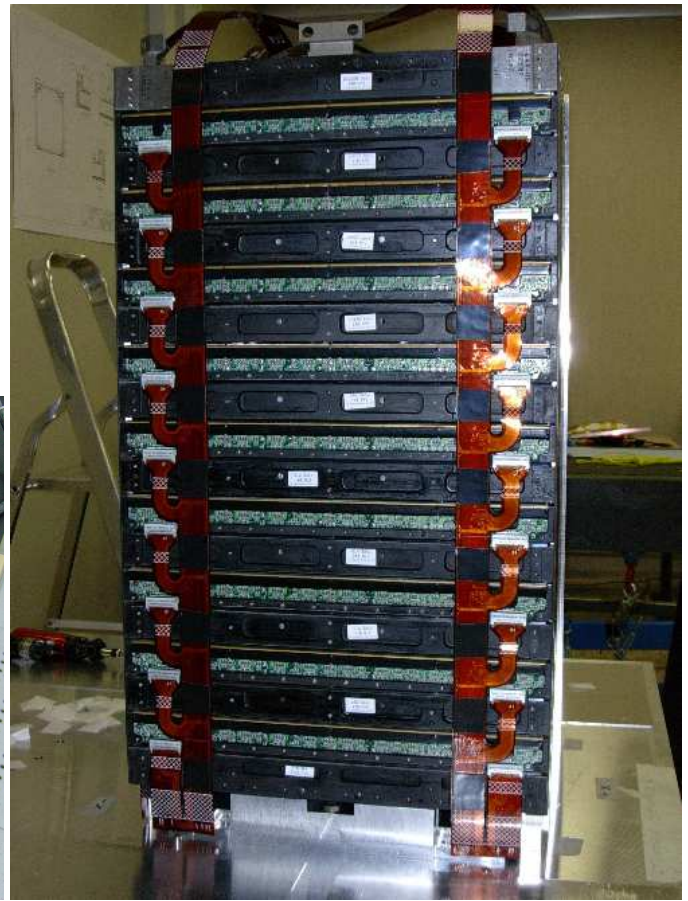
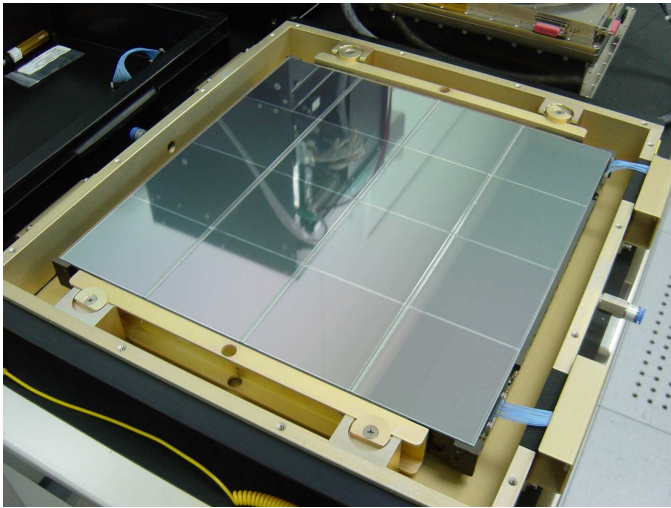


FIG. 4.— (a) A flight tracker tray and (b) a completed tracker module with one sidewall removed.

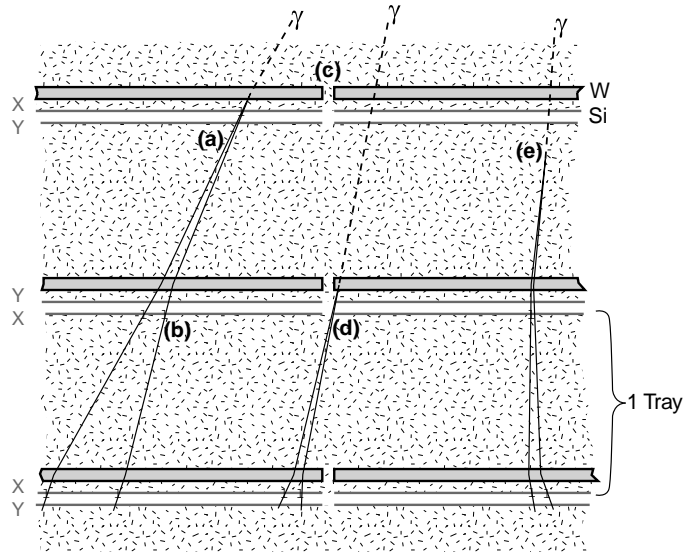


FIG. 5.— Illustration of tracker design principles. The first two points dominate the measurement of the photon direction, especially at low energy. (Note that in this projection only the  $x$  hits can be displayed.) (a) Ideal conversion in W: Si detectors are located as close as possible to the W foils, to minimize the lever arm for multiple scattering. Therefore, scattering in the 2nd W layer has very little impact on the measurement. (b) Fine detector segmentation can separately detect the two particles in many cases, enhancing both the PSF and the background rejection. (c) Converter foils cover only the active area of the Si, to minimize conversions for which a close-by measurement is not possible. (d) A missed hit in the 1st or 2nd layer can degrade the PSF by up to a factor of two, so it is important to have such inefficiencies well localized and identifiable, rather than spread across the active area. (e) A conversion in the structural material or Si can give long lever arms for multiple scattering, so such material is minimized. Good 2-hit resolution can help identify such conversions.

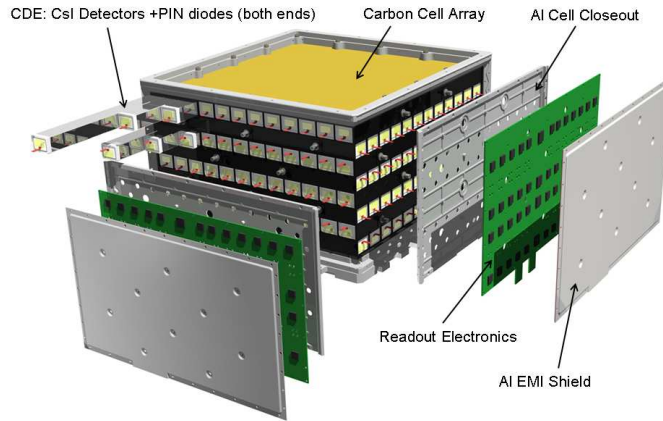


FIG. 6.— LAT calorimeter module. The 96 CsI(Tl) scintillator crystal detector elements are arranged in 8 layers, with the orientation of the crystals in adjacent layers rotated by  $90^\circ$ . The total calorimeter depth (at normal incidence) is 8.6 radiation lengths.

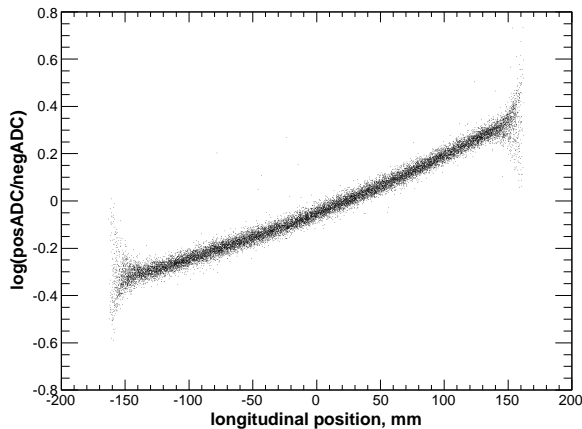


FIG. 7.— Light asymmetry measured in a typical calorimeter crystal using sea level muons. The light asymmetry is defined as the logarithm of the ratio of the outputs of the diodes at opposite ends of the crystal. The width of the distribution at each position is attributable to the light collection statistics at each end of the crystal for the  $\sim 11$  MeV energy depositions of vertically incident muons used in the analysis. This width scales with energy deposition as  $E^{-1/2}$ .

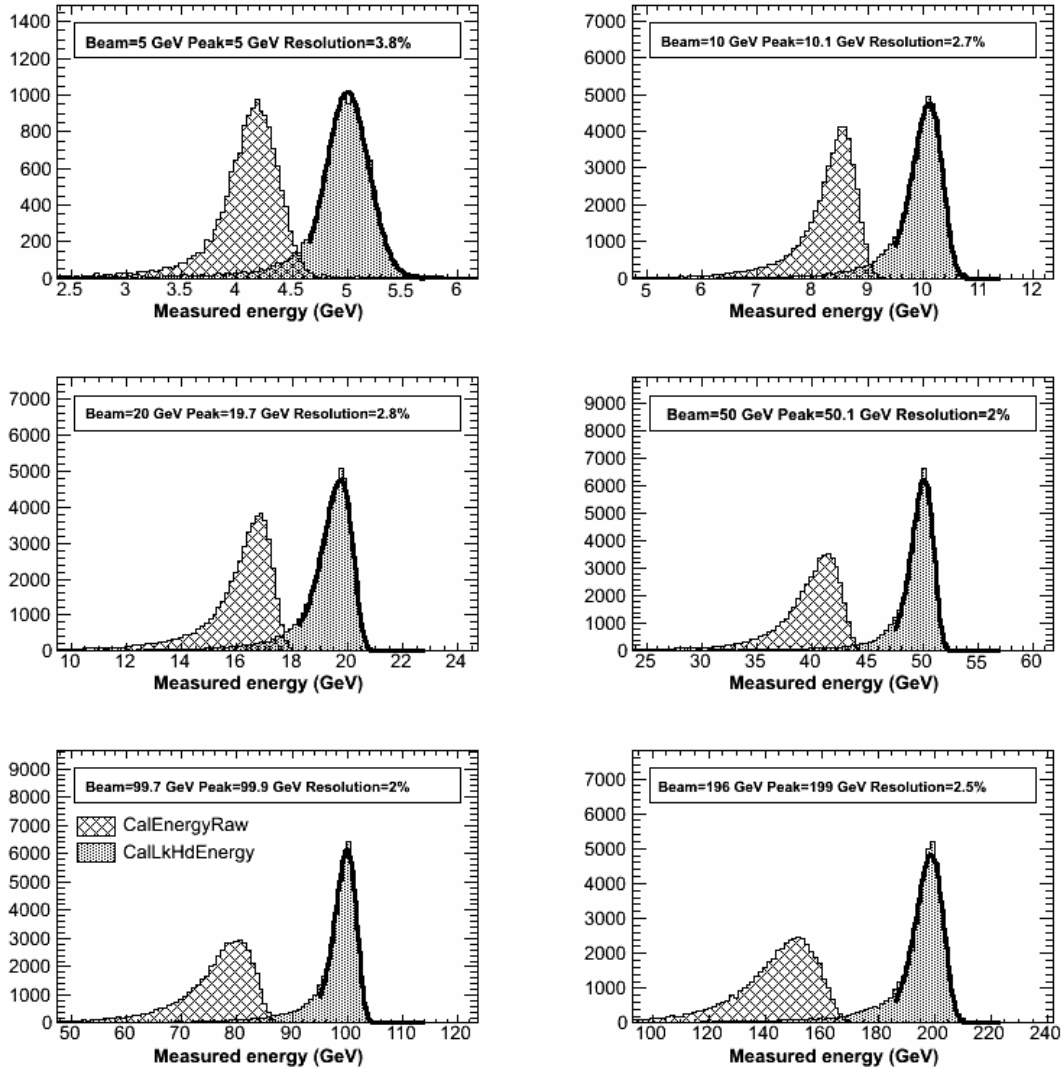


FIG. 8.— Energy resolution as a function of electron energy as measured with the LAT calibration unit in CERN beam tests. Each panel displays a histogram of the total measured energy (hatched peak) and the reconstructed energy (solid peak), using the LK method, at beam energies of 5, 10, 20, 50, 99.7 and 196 GeV, respectively. The beams entered the calibration unit at an angle of  $45^\circ$  to the detector vertical axis. As long as shower maximum is within the calorimeter, the energy measurement and resolution are considerably improved by the energy reconstruction algorithms. The measured energy resolutions ( $\Delta E/E$ ) are indicated in the figure.

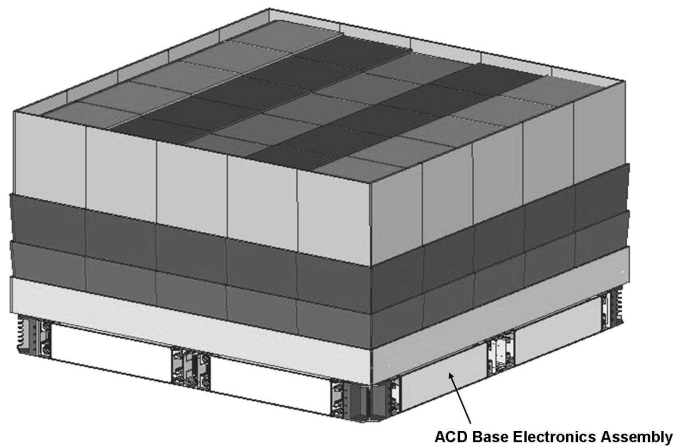


FIG. 9.— LAT Anticoincidence Detector (ACD) design. The ACD has a total of 89 plastic scintillator tiles with a  $5 \times 5$  array on the top and 16 tiles on each of the 4 sides. Each tile is readout by 2 photomultipliers coupled to wavelength shifting fibers embedded in the scintillator. The tiles overlap in one dimension to minimize gaps between tiles. In addition, 2 sets of 4, scintillating fiber ribbons are used to cover the remaining gaps. The ribbons, which are under the tiles, run up the side, across the top, and down the other side. Each ribbon is readout with photomultipliers at both ends.

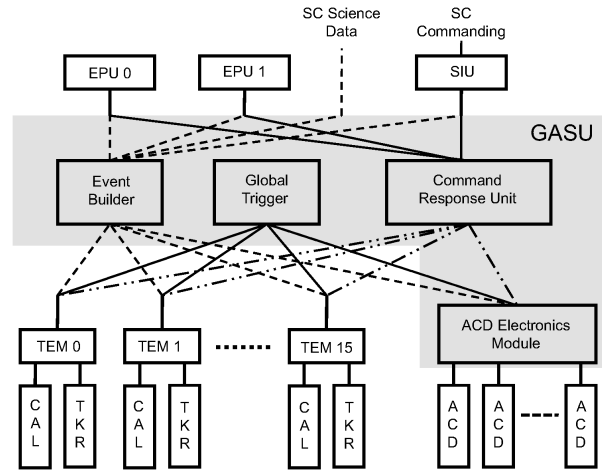


FIG. 10.— LAT Data Acquisition System (DAQ) architecture. The Global-trigger/ACD-module/Signal distribution Unit (GASU) consists of the ACD Electronics Module, the Global Trigger Module (GTM), the Event Builder Module (EBM), and the Command Response Unit (CRU). The trigger and data readout from each of the 16 pairs of tracker and calorimeter modules is supported by a Tower Electronics Module (TEM). There are two primary Event Processing Units (EPU) and one primary Spacecraft Interface Unit (SIU). Not shown on the diagram are the redundant units (e.g. 1 SIU, 1 EPU, 1 GASU).

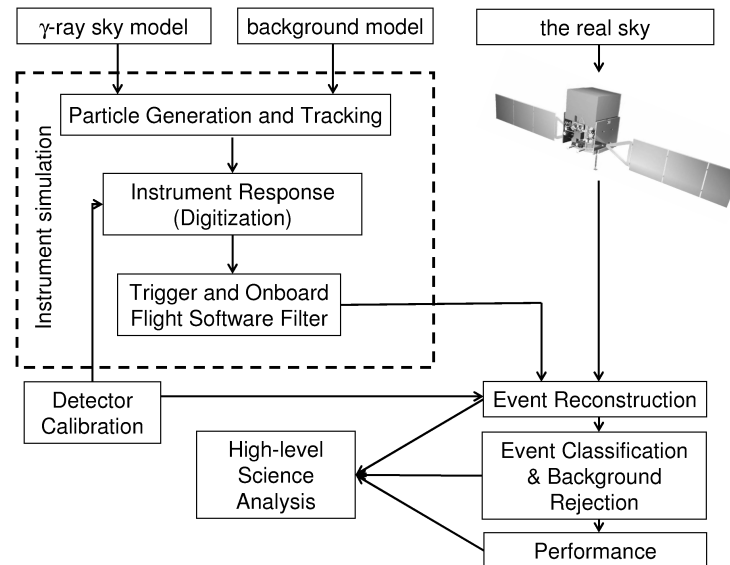


FIG. 11.— Components of the instrument simulation, calibration, and data analysis.

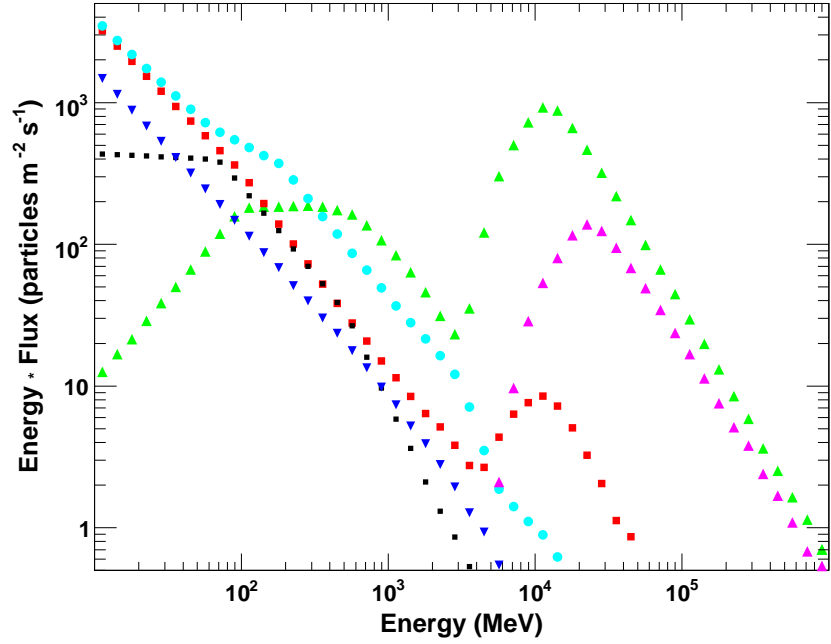


FIG. 12.— Orbit averaged background fluxes of the various components incident on the LAT used in the background model. The fluxes are shown as a function of total kinetic energy of the particles: protons (green filled triangles up), He (purple filled triangles up), electrons (filled red squares), positrons (light blue squares), Earth albedo neutrons (black squares), and Earth albedo  $\gamma$ -rays (dark blue filled triangles down). The effect of geomagnetic cutoff is seen at 3 GeV for protons and electrons, and at higher energy for helium nuclei. At low energies the curves show the sum of re-entrant and splash albedo for electrons and positrons.

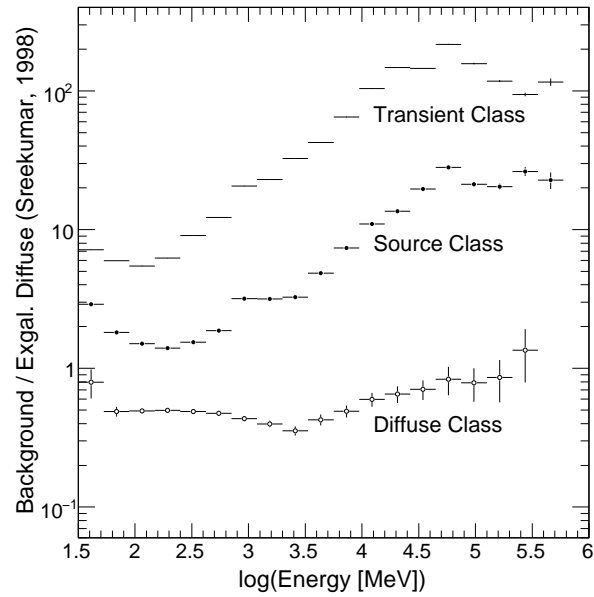


FIG. 13.— Ratio of the residual background to the extragalactic diffuse background inferred from EGRET observations (Sreekumar et al. 1998) for each of the three analysis classes. The integral EGRET diffuse flux is  $1.45 \times 10^{-7}$  ph cm $^{-2}$  s $^{-1}$  sr $^{-1}$  above 100 MeV.

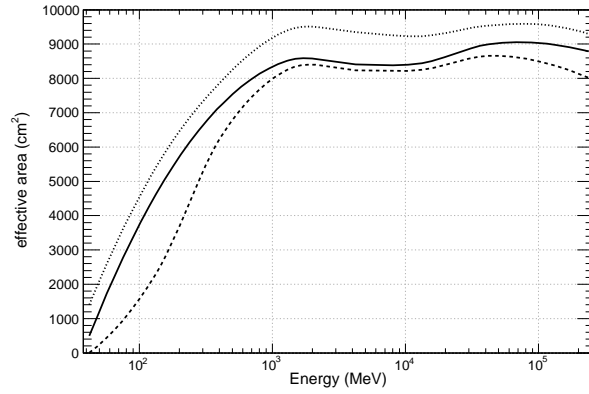


FIG. 14.— Effective area versus energy at normal incidence for Diffuse (dashed curve), Source (solid curve), and Transient (dotted curve) analysis classes.

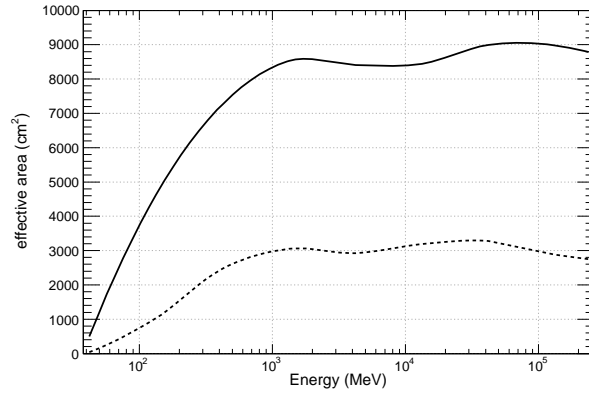


FIG. 15.— Effective area versus energy at normal incidence (solid curve) and at 60° off-axis (dashed curve) for Source analysis class.

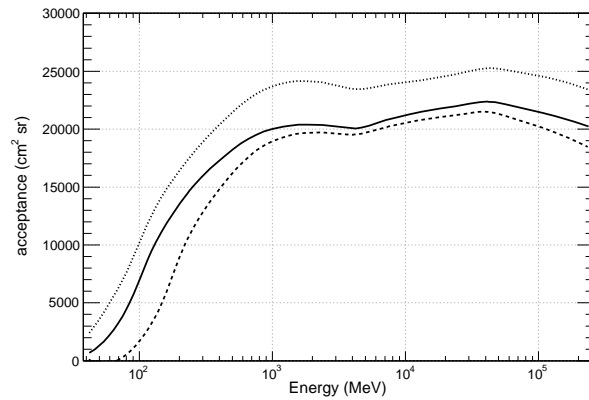


FIG. 16.— Acceptance versus energy for Diffuse (dashed curve), Source (solid curve), and Transient (dotted curve) analysis classes.

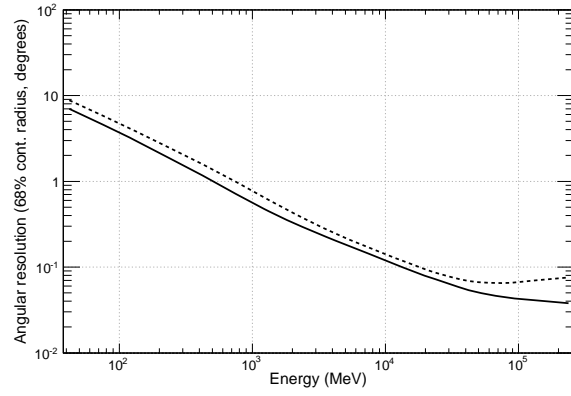


FIG. 17.— 68% containment radius versus energy at normal incidence (solid curve) and at 60° off-axis (dashed curve) for conversions in the thin section of the tracker.

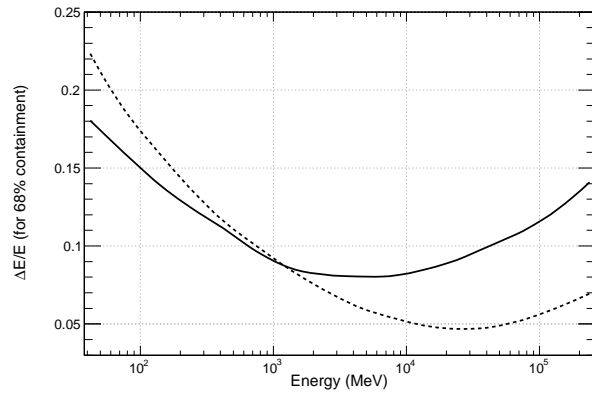


FIG. 18.— Energy resolution versus energy for normal incidence (solid curve) and at 60° off-axis (dashed curve).

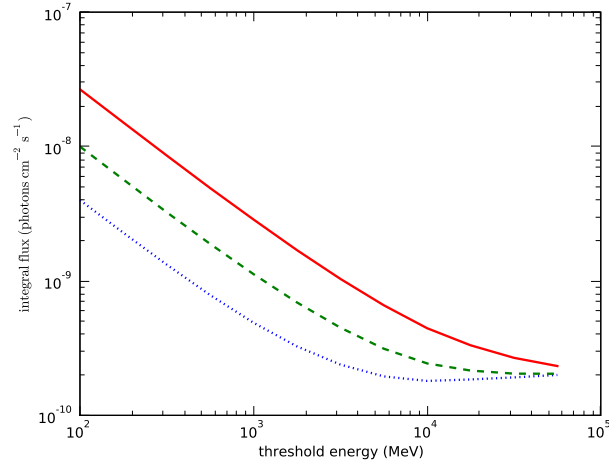


FIG. 19.— Integral source sensitivity for  $5\sigma$  detection for 1 year sky survey exposure. The source is assumed to have a power law differential photon number spectrum with index  $-2.0$  and the background is assumed to be uniform with integral flux (above 100 MeV) of  $1.5 \times 10^{-5}$  ph cm $^{-2}$  s $^{-1}$  sr $^{-1}$  (dotted curve) and spectral index  $-2.1$ , typical of the diffuse background at high galactic latitudes. The background is 10 times higher and 100 times higher for the dashed and solid curves, respectively, representative of the diffuse background near or on the galactic plane.

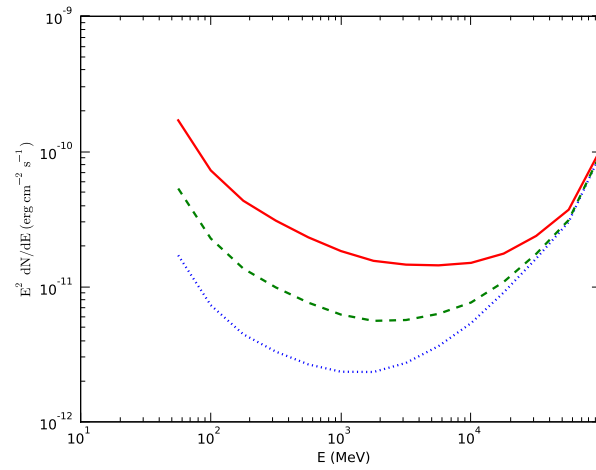


FIG. 20.— Differential source sensitivity in 1/4 decade bins for  $5\sigma$  detection for 1 year sky survey exposure. The source is assumed to have a power law differential photon number spectrum with index  $-2.0$  and the background is assumed to be uniform with integral flux (above 100 MeV) of  $1.5 \times 10^{-5}$  ph cm $^{-2}$  s $^{-1}$  sr $^{-1}$  (dotted curve) and spectral index  $-2.1$ , typical of the diffuse emission at high galactic latitudes. The background is 10 times higher and 100 times higher for the dashed and solid curves, respectively, representative of the diffuse background near or on the galactic plane.

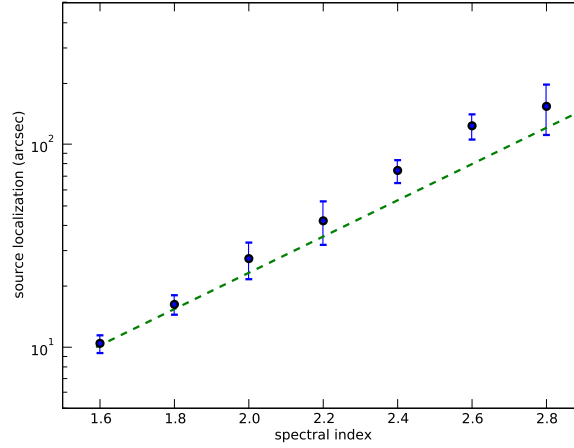


FIG. 21.— LAT 68% confidence radii localizations for a source with integral flux (above 100 MeV) of  $10^{-7}$   $\text{ph cm}^{-2} \text{s}^{-1}$  versus source spectral index for a source detected in the one-year sky survey. The variation of angular resolution with energy and viewing angle from the instrument axis is taken into account. In effect, the source viewing angle is averaged over in sky-survey mode. The source is assumed to be located in a region with uniform background with integral diffuse flux (above 100 MeV) of  $1.5 \times 10^{-5}$   $\text{ph cm}^{-2} \text{s}^{-1} \text{sr}^{-1}$  and spectral index  $-2.1$ . The source localization radius scales as  $(\text{flux})^{-1/2}$ .

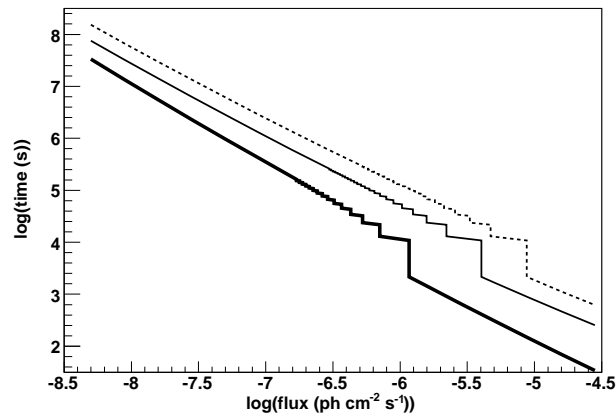


FIG. 22.— Minimum time necessary to detect a source at high latitude with  $5\sigma$  significance (thick solid curve), to measure its flux with an accuracy of 20% (thin solid curve) and its spectral index with an uncertainty of 0.1 (dashed curve), as a function of source flux. A photon spectral index of 2.0 is assumed. The steps at short times are due to the discontinuous source coverage due to the observatory survey mode.

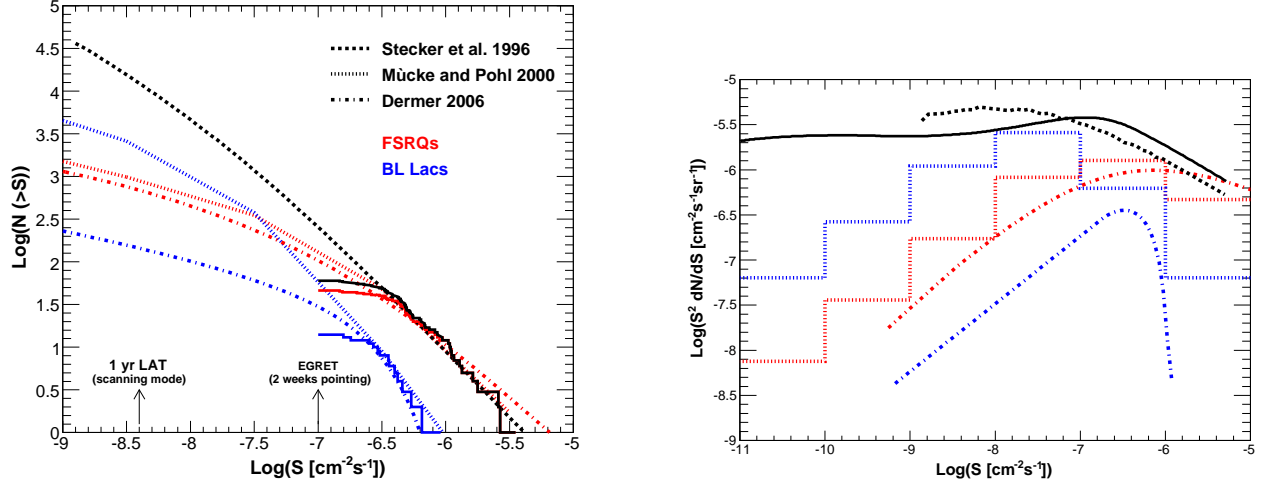


FIG. 23.— (a) Cumulative number distribution of EGRET detected blazars measured over two-week intervals (FSRQs: red curves) and BL Lac objects: blue curves) and various model predictions (Stecker & Salamon 1996: long-dashed line; Mücke & Pohl 2000: dashed-dotted lines; Dermer 2007: dashed lines). The predicted number of radio-loud AGN ranges from  $\sim 10^3$  up to  $\sim 10^4$  sources. (b) The predicted power distribution of radio-loud AGN for the respective models, with the solid black line representing the model of Narumoto & Totani (2006), the black dotted line corresponds to the predicted power distribution of Stecker & Salamon (1996). The colored histograms correspond to the predicted power distributions for BL Lacs (blue) and FSRQs (red) of Mücke & Pohl (2000), and the colored curves correspond to the power distributions of BL Lacs (blue) and FSRQs (red) of Dermer (2007). The main contribution to the extragalactic diffuse  $\gamma$ -ray background is predicted to come from sources at the peak of the respective model distribution.

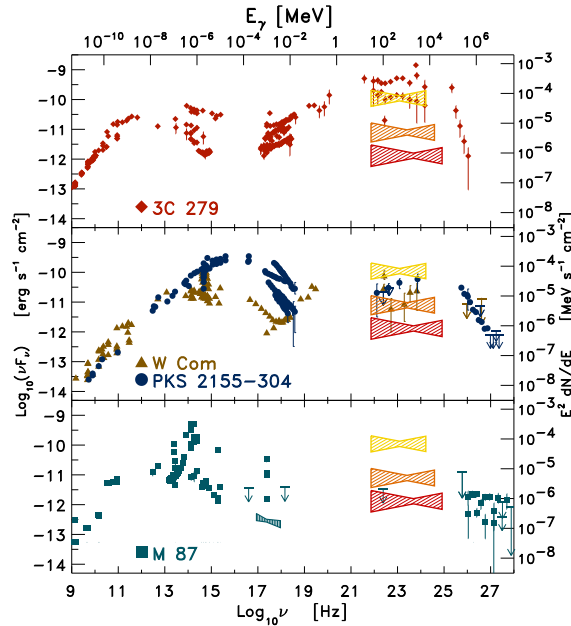


FIG. 24.— Spectral energy distributions (SEDs) of four  $\gamma$ -ray blazars: 3C 279 (a typical FSRQ,  $z = 0.5362$ , top); W Com (a low energy peaked BL Lac object, LBL,  $z = 0.102$ ) and PKS 2155-304 (a high energy peaked BL Lac object, HBL,  $z = 0.116$ ) middle; M 87 (a FR-I radio galaxy,  $z = 0.00436$ , bottom). Included in the SEDs are multiwavelength data points collected in different epochs (different brightness states) for each source (errors bars not represented for clarity). A qualitative representation of the average expected LAT pass band and sensitivity for 1 year of observations is shown. The LAT integral sensitivity shows the minimum needed for a 20% determination of the flux after a one-day (yellow/upper bowties), one-month (orange/middle bowties), and one-year (red/bottom bowties) exposure of in all-sky survey mode for a blazar with a  $E^{-2}$   $\gamma$ -ray spectrum. The resulting significance at each of these levels is about  $8\sigma$ , the spectral index is determined to about 6%, and the bowtie shape indicates the energy range that contributes the most to the sensitivity. To make a measurement at that level or better, a flat spectral energy density curve must lie above the axis of the bowtie.

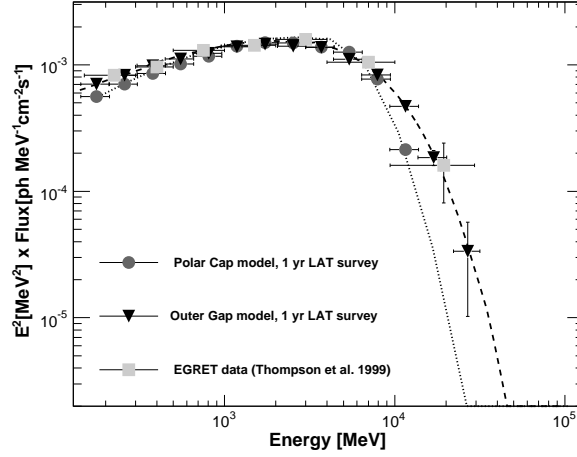


FIG. 25.— The observed EGRET Vela pulsar spectrum, along with realizations of the expected spectrum after one year of GLAST LAT sky survey observations for two pulsar models. The expected sensitivity allows discrimination between the two models and allows tests of the emission zone structure through phase resolved spectra.

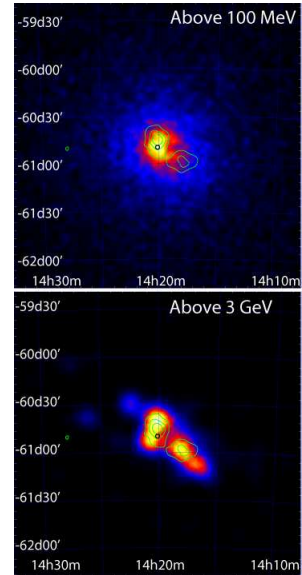
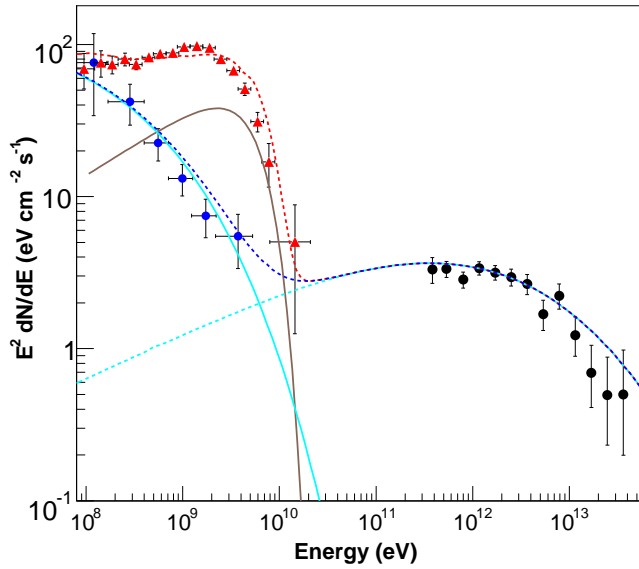


FIG. 26.— Simulation of the K3/Rabbit PWN complex. (a): simulated smoothed LAT count maps from 5 years of sky survey-mode observation - the K3 region is at upper left and the Rabbit nebula is at lower right. Shown are the full  $E > 100$  MeV emission and the  $E > 3$  GeV non-pulsed emission (obtainable by gating off of the PSR J1420-6048 pulse). The green contours show the HESS TeV emission. At high energies the two PWNe are clearly resolved. (b): the HESS spectrum of Compton emission from the PWNe along with simulated LAT spectra from five years of sky-survey type observations (red points). The blue points show the simulated off-pulse spectrum measured with the LAT, indicating a clear detection of the synchrotron component of the PWNe. Also shown are two pulsar-like spectra. The brighter pulsar model is for Vela-like emission from PSR J1420-60438; the fainter (dashed line) is for an unknown Geminga-like pulsar in the Rabbit.

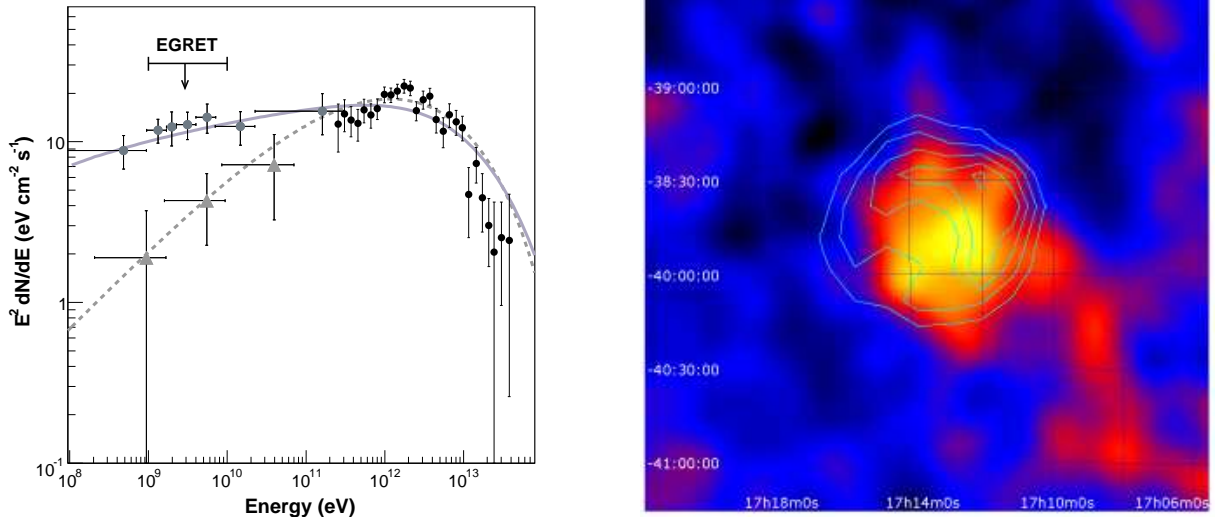


FIG. 27.— The HESS spectrum of the shell SNR RX J1713.7-3946, with plausible leptonic and hadronic models. Note that EGRET was not able to distinguish the SNR from the relatively bright nearby point source 3EG J1714-3857 and upper limits to the SNR flux from this source’s spectrum did not allow EGRET to distinguish these possibilities. However, 5y of LAT observations at typical sky survey duty cycle can. (a) Simulated LAT spectra for the two cases (Funk 2008). A differential spectral index of  $\gamma = 2$  has been assumed for both the parent proton and electron energy distributions. The observed  $\gamma$ -ray spectrum is sensitive to that assumption, which limits the ability to differentiate between parent species. (b) Result of a Lucy-Richardson deconvolution of the simulated LAT counts map, after cleaning of the point source. The SNR is clearly resolved, although the bright background of the Galactic plane limits the S/N of the detection.

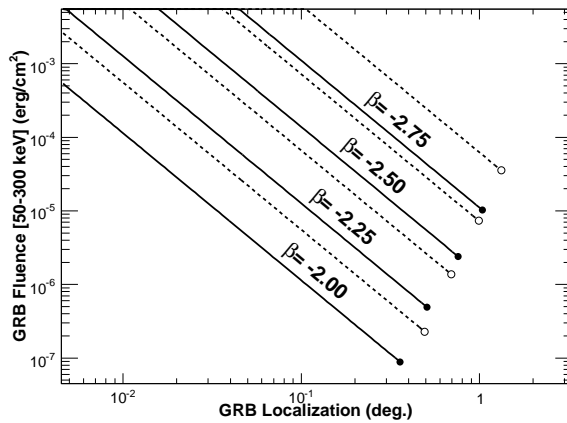


FIG. 28.—  $\gamma$ -ray burst localization with the LAT. The lines correspond to the scaling law between the location accuracy (at  $1\sigma$ ) and the intensity of the burst, expressed as fluence in the 50–300 keV band. Solid lines correspond to GRB at normal incidence, and dashed lines to  $60^\circ$  off-axis. Different sets of lines are for different high-energy spectral indexes (assuming the Band function describes the GRB spectral energy distribution). The starting points of the lines, (filled circles for on-axis, and empty for off-axis) correspond to the minimum fluence required to detect a burst (at least 10 counts in the LAT detector).

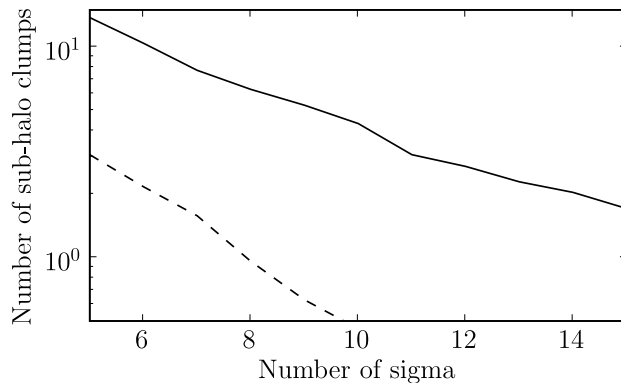


FIG. 29.— Number of clumps observed by *Fermi*/LAT vs. number of  $\sigma$  significance in 5 years of LAT observations in all-sky scanning mode (solid line); 1 year of observation (dashed line). A generic WIMP of mass 100 GeV and  $\langle\sigma v\rangle = 2.3 \times 10^{-26} \text{ cm}^3 \text{ s}^{-1}$ , a halo clump distribution from Taylor & Babul (2005a; 2005b) and diffuse  $\gamma$ -ray backgrounds according to Sreekumar et al. (1998) and Strong et al. (2000) have been assumed.